



HAL
open science

Synthesis of Metal and Conjugated Polymer Nanostructures in Hexagonal Mesophases for Application in Fuel Cells and photocatalysis

Dita Floresyona

► **To cite this version:**

Dita Floresyona. Synthesis of Metal and Conjugated Polymer Nanostructures in Hexagonal Mesophases for Application in Fuel Cells and photocatalysis. *Polymers*. Université Paris Saclay (COMUE), 2017. English. NNT: 2017SACLS206 . tel-01865813

HAL Id: tel-01865813

<https://theses.hal.science/tel-01865813>

Submitted on 2 Sep 2018

HAL is a multi-disciplinary open access archive for the deposit and dissemination of scientific research documents, whether they are published or not. The documents may come from teaching and research institutions in France or abroad, or from public or private research centers.

L'archive ouverte pluridisciplinaire **HAL**, est destinée au dépôt et à la diffusion de documents scientifiques de niveau recherche, publiés ou non, émanant des établissements d'enseignement et de recherche français ou étrangers, des laboratoires publics ou privés.

NNT : 2017SACLS206

THESE DE DOCTORAT
DE L'UNIVERSITE PARIS-SACLAY
PREPAREE AU
« L'UNIVERSITE PARIS-SUD »

ECOLE DOCTORALE N° 571

Science Chimiques : Molécules, Matériaux, Instrumentation et Biosystèmes
Spécialité de doctorat : chimie

Par

Dita Floresyona

Synthèse de nanostructures métalliques et de polymères conducteurs dans des mésophases hexagonales pour des applications dans les piles à combustible et le traitement de l'eau

Thèse présentée et soutenue à Orsay, le 15 Septembre 2017 :

Composition du Jury :

M. Ally Aukauloo	Professeur des Universités (Univ. Paris-Sud)	Présidente du jury
Mme. Sophie Cassaignon	Professeur des Universités (Université Pierre et Marie Curie)	Rapporteur
M. Boniface Kokoh	Professeur des Universités (Université de Poitiers)	Rapporteur
Mme. Anne-Lucie Teillout	Maitre de Conférence (Univ. Paris-Sud)	Examinatrice
Mme. Hynd Remita	Directrice de Recherche CNRS (Univ. Paris-Sud)	Directrice de thèse
Mme. Laurence Ramos	Directrice de Recherche CNRS (Université de Montpellier)	Co-directrice de thèse

Acknowledgements

I want to express my sincere gratitude to my supervisor, Dr. Hynd REMITA. I am grateful because she has been willing to accept me as her PhD student. I thank her for all the knowledge, guidance, and patience during my thesis. Her passion for research, her dynamic in working, her friendliness, and her awareness to people, inspired me. She taught me to be tough. She has given me opportunities to attend many conferences, to participate in scientific events, and to have many collaborations.

I want to thank my co-supervisor, Dr. Laurence RAMOS for the discussions, input, and detail corrections of my work and my thesis. She has been really patience in explaining all the detail calculations in SAXS and WAXS measurement. I thank her for her fast response.

I would like to thank Prof. Boniface Kokoh, Prof. Sophie Cassaignon, Prof. Ally Aukaaloo, and Dr. Anne-Lucie Teillout. I am glad that they accepted to be a member of juries of my thesis.

I would like to thank Dr. Anne-Lucie Teillout and Prof. Pedro de Oliveira (LCP, Université Paris-Sud) for their guidance and help during electrochemistry experiment, for the fruitful discussions, and for correcting the electrochemistry part of my thesis. I particularly thank Anne-Lucie for her patience and help..

I thank Philippe Dieudonne-George for SAXS and WAXS experiments in Laboratoire de Charles Coulomb in Université de Montpellier.

I would like to thank all my collaborators. I thank Prof. Fabrice Goubard and Prof. Pierre-Henri Aubert (Université de Cergy-Pontoise) for the electrochemistry and conductivity measurements, for the discussion, and input for my work. I thank Prof Teko Napporn (Université de Poitiers) for glucose oxidation experiments, discussions, and very useful input for my thesis. I thank Prof. Isabelle Lampre (LCP, Université Paris Sud) for Fluorescence Spectroscopy experiments. I thank Jérémie Mathurin and Prof. Alexandre Dazzi from (LCP, Université Paris Sud) for AFMIR experiments. I thank Dr. Jean-louis Marignier for the experiments in ELYSE. I thank Dr. Daniel Bahena (IPCYT, Mexico) for HAADF-STEM and EDS analysis. I thank Diana Dragoé (ICCMO, Université Paris

Sud) for XPS analysis, data treatment, and discussion. I thank Patricia Beaunier (UPMC) for TEM characterizations.

I warmly thank Stephanie Mendes Merinho and Ally Aukauloo (ICCMO, Université Paris Sud) for O₂ evolution experiments and for fruitful discussions.

I thank Mireille Benoît for being very helpful in finding chemical products, set-up some experiments, and dealing with many technical problems in the lab.

Special thanks to my friends and colleagues in LCP. I thank Srabanti Ghosh for the guidance and supervision during my master internship, it helped me a lot to understand my PhD projects. I thank Iyad SARHID, for helping me to prepare all the documents for Ecole Doctorale in 2 hours before the deadline, so I could finally be accepted. I thank Maria Guadalupe, Xiaojiao Yuan, Anais Lehoux, Marie Clement, Ana Laura, Teseer Bahri, and Zhengpeng Chui for helping me not only with the experiments and data treatment, but also to deal with French administration. I thank them for the good working ambience, friendship, and humor. They make my Monday mornings and comeback after vacations not so difficult.

I want to thank my Indonesian friends, for Mbak Arum, Mba Alvi, Ajeng, mbak Sundari, Tesa, Risa, Uun, and Vini. I thank them for the “ngopi-ngopi cantik” and “jalan-jalan bego” times in Paris during the weekend.

And at last but most importantly, I want to thank my family, especially my parents, for the endless love, support, and prayers. They are the two people who always believe in me, in my capability, who never stop me to continue education and pursue my dreams. This thesis is dedicated to them.

Table of Content

Adknowledgements	i
Table of content	iii
General introduction	vi
Résumé général	ix
CHAPTER I. Objectives and State of the Arts	1
I.1 Global environmental problem	3
I.2 Synthesis of nanomaterials	4
I.2.1 Radiolysis technique for the synthesis of nanomaterials	5
I.2.2 Principle of radiolysis	5
I.2.3 Dose rate effect	7
I.2.4 Synthesis of nanomaterials using templates	9
I.3 Soft templates: Swollen hexagonal mesophases	10
I.3.1 Surfactant	11
a. Anionic surfactants	11
b. Nonionic surfactants	12
c. Cationic surfactants	12
d. Zwitterionic (amphoteric) surfactants	12
I.3.2 Surfactant self-assembly	13
I.3.3 Critical packing parameter (CPP)	14
I.3.4 Self-assembly in hexagonal mesophases	17
I.3.5 Characterization of hexagonal mesophases by Small Angle X-Ray Scattering (SAXS)	18
I.3.6 Swollen hexagonal mesophases	20
I.4 Synthesis of nanomaterials in hexagonal mesophases	21
I.4.1 Synthesis of porous metal nanostructures in the water phase of hexagonal mesophases	21
a. The role of surfactants	22
b. The role of the dose rate	23
I.4.2 Synthesis of conjugated polymer nanostructures in the oil phase of hexagonal mesophases	24
CHAPTER II. Experimental Part	27
II.1 Preparation of hexagonal mesophases	30
II.1.1 Synthesis of metal nanostructures in the aqueous phase of hexagonal mesophases for application in fuel cells	30
a. Swollen hexagonal mesophases containing Pd and Pt	30
b. Preparation of hexagonal mesophases containing AuPd, AuPt, and AuPdPt	31
c. Preparation of hexagonal mesophases containing PtNi	32
II.1.2 Synthesis of conjugated polymer nanostructures in the oil phase of hexagonal mesophases	33
a. Synthesis of conjugated polymer P3HT (poly(3-hexylthiophene))	33
b. Synthesis of nano PDPB (Poly(diphenylbutadiene) (as supporting polymer) in hexagonal mesophases	34

II.1.3	Synthesis of Pt-PDPB nanocomposites in hexagonal mesophases	34
II.2	Material characterizations	35
II.2.1	Small and Wide Angle X-Ray Scattering	35
II.2.2	Transmission Electron Microscopy (TEM)	35
II.2.3	Scanning Electron Microscopy (SEM)	36
II.2.4	HAADF-STEM	36
II.2.5	XPS (X-Ray Photoelectron Spectroscopy)	36
II.2.6	UV–vis spectrophotometer	36
II.2.7	Fluorescence spectroscopy	37
II.2.8	Maldi-TOF (Matrix Assisted Laser Desorption/Ionization Time of Flight)	37
II.2.9	Attenuated Total reflectance (ATR-FTIR)	37
II.2.10	AFMIR	37
II.2.11	Electrochemical analysis for polymer nanostructures	38
II.3	Application of metal and polymer nanostructures	38
II.3.1	Metal nanostructures	38
a.	Ethanol oxidation using bimetallic PdPt	38
b.	Glucose oxidation using AuPd, AuPt, and AuPdPt	39
c.	H ₂ evolution using PtNi	39
II.3.2	Application of conjugated polymer nano P3HT for photodegradation of pollutants	40
CHAPTER III Synthesis of Porous Metal Nanostructures in the Confined Water Phase of Hexagonal Mesophases for Application in Fuel Cells		43
III.1	Fuel cells	45
III.1.1	Basic working principle	46
III.1.2	Direct alcohol fuel cells	47
III.1.3	Nanomaterials for electrocatalysis in DAFCs	49
a.	Anodic catalysis	51
b.	Cathodic catalysis	51
III.2	Bimetallic PdPt Nanoballs Synthesized in Hexagonal Mesophases for Electrooxidation of Ethanol	51
III.2.1	Materials characterizations	53
a.	Characterization of hexagonal mesophases by SAXS	53
b.	Transmission Electron Microscopy (TEM)	59
c.	Pore size measurement by SAXS-WAXS	61
d.	Pore size measurement by BET	63
e.	HAADF-STEM and EDS	64
III.2.2	Application of PdPt nanoballs for electrooxidation of ethanol	65
a.	Cyclic voltammetry of PdPt nanoballs in alkaline solution	65
b.	Mechanism of ethanol oxidation on PdPt nanoballs used as electrocatalysts	66
c.	Tuning the composition of porous PdPt bimetallic nanoballs for ethanol oxidation reaction	67
d.	Influence of the pore size of pure Pd nanoballs on their electrocatalytic activity towards ethanol oxidation	70

e. Influence of pore size of Pd ₇₅ Pt ₂₅ nanoballs on their electrocatalytic activity towards ethanol oxidation	76
III.3 Synthesis of bimetallic (Au@Pd and Au@Pt core shell) and trimetallic AuPdPt nanostructures for ethanol and glucose oxidation reactions	81
III.3.1 Material characterizations	82
III.3.2 Application of Au@Pd, Au@Pt, and AuPdPt for ethanol oxidation reaction	86
III.3.3 Application of AuPd, AuPt, and AuPdPt for glucose oxidation reaction (in collaboration with Teko Napporn from Université de Poitiers)	89
III.4 Synthesis of PtNi porous nanostructures for H₂ evolution reaction	91
III.4.1 Material characterization	91
III.4.2 Application of PtNi for H ₂ evolution	95
III.5 Conclusion	96
CHAPTER IV Conjugated Polymer Nanostructures Synthesized in the Oil Phase of Hexagonal Mesophases for Photocatalysis under Solar Light	99
IV.1 Theoretical background and bibliography	102
VI.1.1 Heterogeneous photocatalysis	102
VI.1.2 Photocatalytic process	103
VI.1.3 Conjugated polymers	104
VI.1.4 The importance of nanostructuring of conjugated polymers for photocatalytic application	107
IV.2 Synthesis and application of conjugated polymer poly (3-hexylthiophene) for pollutant degradation under visible light	109
VI.2.1 Material characterizations	110
VI.2.2 Photocatalytic tests	116
VI.2.3 Photocatalytic mechanism	120
VI.2.4 Deposition of nano P3HT on a support for photocatalytic application	125
IV.3 Conclusion	126
CHAPTER V Synthesis of Pt-PDPB (Platinum-Polydiphenylbutadiyne) Nanocomposites in Hexagonal Mesophases	127
V.1 Introduction	129
V.2 Material characterization	132
V.2.1 Material characterization	132
V.2.2 Characterization by Transmission Electron Microscopy (TEM)	134
a. PDPB nanostructures	134
b. Pt nanostructures	135
c. Pt-PDPB nanocomposites	136
V.2.3 Characterization by AFMIR	137
V.3 Conclusion and Perspectives	138
CHAPTER VI General conclusions and Perspectives	141
REFERENCES	151

General Introduction

The inevitable increase in population and economic development that must necessarily occur in many countries have brought two big problems: the crisis of energy and environmental pollution. Fossil fuels, which are polluting, non-renewable, and the main contributor of greenhouse effect are still considered as the major energy resources in many countries nowadays. The other serious problem caused by the on-going industrialization and human activities is the environmental pollution (water, air and soils). Water, which is really essential to our existence, is polluted by those activities.

Fuel cells are considered as clean energy devices. However, the problems of high cost and limited durability of the electrocatalysts, which is mainly caused by the use of Pt electrocatalysts in most of the reactions involved in fuel cells, limit their action for commercialization. Combining Pt with other less expensive metals, decreasing the particle size or increasing the surface area by engineering porous Pt-based catalysts are expected to improve their activity and reduce their cost.

On the other hand, photocatalysis is considered as a promising technology for water and air depollution. Titanium dioxide (TiO_2) is the most commonly used semiconductor for photocatalysis because of its good photocatalytic activity, low price, high stability and non-toxicity. However, TiO_2 is only active under UV light. Conjugated polymer (CP) materials for photocatalysis has recently emerged as a very hot field topic of research. CPs combine the properties of organic materials (low cost and easy processing) and the properties of semiconductor materials (such as high conductivity, mechanical and thermal stability). It has been recently shown that nanostructuring of conjugated polymers is essential for their application in photocatalysis.

Physico-chemical properties of nanomaterials depend on their size and shape. Therefore, synthesis of metal, polymer or composite nanomaterials of controlled shape, structure and composition is a main challenge in nanoscience and nanotechnology.

In this work, we synthesized porous metal nanostructures, conjugated polymers, and composite nanomaterials in soft templates provided by hexagonal mesophases. These hexagonal mesophases are versatile templates made of quaternary systems (water, surfactant, co-surfactant, oil). The nanomaterials synthesized *in situ* can be extracted by

simple alcohol (ethanol or 2-propanol) addition to the template and washing (with the alcohol).

Radiolysis is a powerful technique to synthesize metal nanostructures and nanomaterials in solutions or in complex media. This technique has been used to synthesize porous mono- and multi-metallic nanostructures, polymer and composite metal-polymer nanomaterials. The porous metal nanostructures were used as electrocatalysts for reactions involved in fuel cells (mainly ethanol oxidation), while conjugated polymer nanostructures were used as photocatalysts for water treatment under visible light.

The structure of this manuscript is the following:

Chapter 1 is devoted to provide generalities concerning the synthesis process of nanomaterials using hard and soft templates. Principles of radiolytic synthesis of nanomaterials are presented. The soft templating approach for nanomaterials synthesis is described. The formation of hexagonal mesophases and their use as soft templates for the synthesis of metal, polymer and composite nanostructures are presented.

Chapter 2 gives details of the experimental procedures, which include synthesis of nanomaterials in soft template hexagonal mesophases, radiolytic synthesis, characterization techniques (x-ray scattering, microscopy, spectroscopy, and electrochemistry), and electrocatalytic tests (for metal nanostructures) and photocatalytic experiments (for conjugated polymer nanostructures).

In **Chapter 3**, synthesis of porous metal nanostructures in the confined water phase of hexagonal mesophases, and their application as electrocatalysts in several reactions involved in fuel cells are presented. Different porous metal nanostructures were synthesized and characterized with different techniques: porous PdPt nanoball (of controlled porosity and composition), Au@Pd, Au@Pt core-shells, AuPdPt nanoballs, and porous PtNi nanostructures.

- Porous PdPt nanoballs were used as electrocatalysts for ethanol oxidation reaction in alkaline media. The pore size of PdPt nanoballs were tuned by controlling the volume ratio of oil over water of the hexagonal mesophase templates. PdPt

nanoballs with different pore sizes were characterized by transmission microscopy, x-ray scattering, and BET. The relative composition of Pd and Pt was optimized. The study of the influence of the pore size of PdPt nanoballs on their electroactive surface area as well as their electro-activity towards ethanol oxidation reaction are presented. Results show that the electro active surface (EAS) and ethanol oxidation activity increase with bigger pore size.

- Other porous nanostructures were also synthesized by radiolysis in these soft templates: Au@Pd, Au@Pt (with core-shell structures), trimetallic AuPdPt nanostructures and PtNi nanoballs. Preliminary results about their application in fuel cells (ethanol oxidation, glucose oxidation, and H₂ reduction) are presented.

In **Chapter 4**, synthesis of poly (3-hexylthiophene) nanostructures in the oil phase of hexagonal mesophases and their application in photocatalysis for water treatment was studied. Photodegradation of organic model pollutants (phenol and rhodamine B) under visible light irradiation was studied. The photocatalytic mechanism was also studied and O₂^{•-} was found to be the main responsible radical in oxidation processes. Deposition of this conjugated polymer nanostructures gave promising results in photocatalysis.

Chapter 5 presents one pot radiolytic synthesis and characterization of Pt-PDPB (Poly(diphenylbutadiene)) nanocomposites. Co-doped mesophases (with Pt precursors confined in the water phase and diphenyl-butadiene DPB in the oil phase) were used as versatile soft templates. Nanowires of PDPB surrounded by 2-nm Pt nanoparticles were obtained.

Finally, in **Chapter 6**, we present the conclusions of this work and some perspectives. Overall, this works emphasize that radiolysis is a powerful method to synthesize nanomaterials and that mesophases are very versatile templates to synthesize different nanomaterials with large panel of applications.

Résumé general

Les mésophases hexagonales sont des systèmes quaternaires formés de tensioactifs et co-tensioactifs, eau salée et huile. Ces mésophases sont utilisées comme moules « mous » pour la synthèse de différents nanomatériaux tels que des nanostructures métalliques poreuses, des nanostructures de polymères conjugués et des nanocomposites métalliques-polymères. Contrairement aux matrices (ou moules) durs, qui nécessitent des réactifs chimiques corrosifs pour extraire les nanomatériaux synthétisés *in situ*, le processus d'extraction des nanomatériaux synthétisés dans les mésophases hexagonales est simple : les nanomatériaux peuvent être extraits simplement par lavage avec de l'éthanol ou du 2-propanol. Un autre intérêt à utiliser ces mésophases comme matrice de synthèse est qu'elles peuvent être gonflées en contrôlant le rapport huile / eau.

Cette thèse est divisée en trois parties: 1) La synthèse de nanostructures métalliques poreuses dans la phase aqueuse des mésophases hexagonales et leur application dans les piles à combustible (oxydation de l'éthanol), 2) La synthèse de nanostructures de polymères conjugués dans la phase huile des mésophases hexagonales pour des applications en photocatalyse et en particulier pour la dégradation de polluants, 3) La synthèse combinée dans les phases huile et eau des mésophases hexagonales de nanocomposites métal-polymère.

Des nanoballs poreux de PdPt ont été utilisés comme électrocatalyseurs pour la réaction d'oxydation de l'éthanol dans les milieux alcalins. La taille des pores des nanoballs de PdPt a été ajustée en contrôlant le rapport volumique de l'huile sur l'eau des modèles de mésophase hexagonale. Des nanoballs de PdPt avec différentes tailles de pores ont été caractérisés par une microscopie de transmission, une diffusion des rayons X et un BET. La composition relative de Pd et Pt a été optimisée. L'étude de l'influence de la taille des pores des nanoballs de PdPt sur leur surface électroactive ainsi que leur électro-activité vis-à-vis de la réaction d'oxydation de l'éthanol sont présentées. Les résultats montrent que la surface électroactive (EAS) et l'activité d'oxydation de l'éthanol augmentent avec une plus grande taille des pores. D'autres nanostructures poreuses ont également été synthétisées par radiolyse dans ces gabarits mous: Au @ Pd, Au @ Pt (avec des structures core-shell), des nanostructures trimétalliques AuPdPt et des

nanoballs PtNi. Les résultats préliminaires concernant leur application dans les piles à combustible (oxydation de l'éthanol, oxydation du glucose et réduction de H₂) sont présentés.

Des nanostructures de polymères conjugués (poly(3-hexylthiophène), P3HT) ont été synthétisées dans la phase huile des mésophases hexagonales. Ces nanostructures de polymères ont une activité photocatalytique élevée sous UV et lumière visible. Le phénol et la rhodamine B ont été utilisés comme polluants modèles. Ces photocatalyseurs sont très stables même après plusieurs cycles photocatalytiques. L'ajout de molécules capteurs et l'étude du mécanisme montrent que les radicaux O₂⁻ sont les principaux radicaux responsables de la dégradation du phénol. De manière très intéressante, l'activité photocatalytique de ces nanostructures de P3HT est fortement augmentée lorsqu'elles sont supportées sur une surface solide. Ce résultat ouvre de nouvelles perspectives pour des applications dans des réacteurs photocatalytiques et des surfaces autonettoyantes.

Des résultats préliminaires sur la synthèse des nanocomposites Pt-PDPB (polydiphénylbutadiyne) sont également présentés dans cette thèse. Des mésophases co-dopées (avec des précurseurs de Pt confinés dans la phase aqueuse et des DPB diphénylbutadiyne dans la phase huileuse) ont été utilisées comme matrices souples polyvalentes. Des nanofils de PDPB entourés de nanoparticules de 2 nm de Pt ont été obtenus.

Nous présentons les conclusions de ce travail et quelques perspectives. Dans l'ensemble, ces travaux soulignent que la radiolyse est une méthode puissante pour synthétiser les nanomatériaux et que les mésophases sont des modèles très polyvalents pour synthétiser différents nanomatériaux avec un large panel d'applications.

Chapter I
Objectives
and
State of the Art

Chapter I

Objectives and State of the Art

I.1 Global environmental problem

Global environmental pollution is not just problem which affects many people. It also affects the entire planet earth.¹ The inevitable increase in population and economic development that must necessarily occur in many countries have brought two big problems: the crisis of energy and environmental pollution.

Fossil fuels such as coal, petroleum, and gas have been considered since the past century as major energy resources for electricity, transportation, industry, etc. In 2013, in Europe, 76% of the energy needs were still derived from fossil fuels, specifically 35 % from oil, 24 % from natural gas, and 17 % from coal (**Figure 1.1**).² In France, the fossil fuel consumption is lower compared to EU because a large part of its energy need is supplied by nuclear energy (41%). As much as 49% of energy consumption in France is provided by fossil fuel (30% from oil, 14.5 % from natural gas, and 4.5 % from coal).

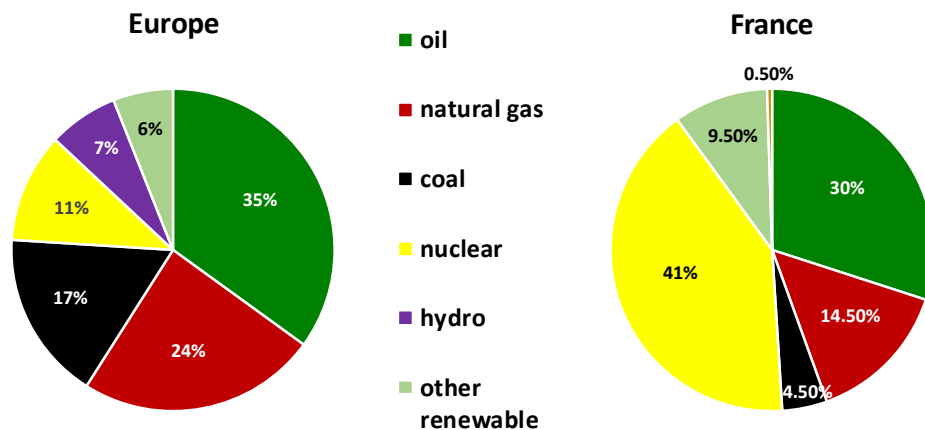


Figure 1.1 Energy consumption by source in Europe and France (2013)²

The utilization of fossil fuels is known to provoke various serious environmental problems, namely atmospheric pollution, greenhouse effect, global warming and depletion of natural resources. The combustion of fossil fuels releases greenhouse gases such as CH₄, N₂O, CO₂, etc.³ The accumulation of those gases in the atmosphere leads to an increase of the earth temperature, or so-called global warming, which generates many

serious environmental problems. Furthermore, the reaction of those gases with water can produce sulfuric, carbonic, and nitric acid, which fall to earth as acid rains. The process of harvesting, processing, and distributing of fossil fuels can also have a harmful impact on the environment. For example, transport of coal requires the use of diesel-powered locomotives, and burning of coal generates large amount of fly ashes. In addition, fossil fuels are non-renewable resources and their amount is progressively reduced. Scientists and engineers will need to invest themselves in solving the issues generated by the utilization of fossil fuels. Greater investment in energy efficient technologies, low carbon technologies, renewable technologies, nuclear energy, and carbon capture and storage technologies is now needed. In transportation, increasing vehicle efficiency along with a **gradual shift from conventional petroleum-fueled technology to fuel cells technology** or rechargeable batteries for electrical cars is currently being a hot topic of research.

The other serious problem caused by the on-going industrialization and human activities is environmental pollution (water, air and soils). Water, which is really essential to our existence, is polluted by those activities. In the last few decades, it has become evident that water resources are limited. Approximately, from the total water in the hydrosphere (1,386 million cubic kilometers) only 2.5 % is fresh water, and only 0.26 % of this fresh water is accessible to humans (concentrated in lakes and river systems).⁴ Water is also fundamental for sustaining a high quality of life. Polluted water or water deficit may cause diseases and damages to the environment. The scarcity of clean water has progressively increased in the last 60 years. By 2025, the majority of population on earth will live under low water supply conditions.

To address these two big energy and environment issues, as material scientists, we can contribute in design of materials for application in energy generation (or storage) and water depollution.

I.2 Synthesis of nanomaterials

Nanosized materials, such as metal or bimetallic nanostructures, metal porous nanostructures, nanotubes, conjugated polymer nanofibers, are attracting growing interest because they often exhibit remarkable properties when compared to bulk materials.⁵ Exceptional magnetic, optical, electronic, and catalytic properties can be exploited for numerous technological applications in particular in energy generation and water

depollution.⁶⁻⁹ Properties such as catalytic, electrocatalytic, and photocatalytic activities could strongly depend on the size and shape of the nanomaterials.¹⁰ Therefore synthesis of nanomaterials that could exhibit well-controlled shapes and sizes has been explored to enhance their performances.¹¹ Many approaches are currently developed to obtain metal and polymer nanostructures in a liquid phase.

The method of preparation of nanoparticles in aqueous medium involves reduction of metal precursor salt by a suitable reducing agent (such as sodium borohydride, ascorbic acid, formaldehyde and hydrazine). The reduction of metal precursor salt may also be carried out using UV-irradiation, microwave radiation and ionizing radiations like γ , X-rays or electron beams. Radiolytic reduction is a powerful method to synthesize metallic nanoparticles and nanostructures.¹²⁻¹⁶ The specificity of the radiation-induced reduction of metal ions into atom lies in generating radiolytic species of strongly reducing potential.

I.2.1 Radiolysis technique for the synthesis of nanomaterials

Radiolysis techniques have been successfully applied for the synthesis of several nanomaterials, including monometallic and bimetallic nanoparticles, polymers and composites.^{12,17} Concerning synthesis of metal nanoparticles, this method offers several advantages over the conventional chemical reducing technique such as: (1) mild conditions (atmospheric pressure and room temperature); (2) homogeneous reduction or polymerization (leading to nanomaterials with controlled and homogeneous size); (3) no additional reducing agents are used (as strong reducing species are formed by solvent radiolysis); and (4) most importantly in the case of bimetallic nanoparticles control of composition and structure (core-shell or alloy) by fixing the dose rate (which fixes the reduction kinetics).¹⁸

I.2.2 Principle of radiolysis

Radiolysis is the interaction of high-energy photons (γ -rays or X-rays) and atomic particles (electrons or ions beams) (so-called ionizing radiation) with matter. Radiolysis generates free radicals. The dose absorbed by the materials is expressed in grays ($1\text{Gy} = 1\text{Jkg}^{-1}$).¹⁹

The interaction of high-energy photon/atomic particles with a solvent such as water results in its excitation and formation of solvated electrons (e_s^-) and radicals.¹⁹ The processes of radical formation in the case of radiolysis of water are given in the reactions 1.1 to 1.4.

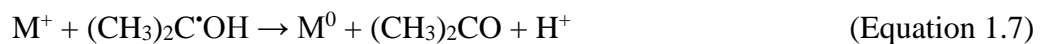


The hydrated/solvated electrons (e_s^-) and hydrogen radical (H^\bullet) are strong reducing agents with the respective redox potentials: $E^\circ(\text{H}_2\text{O}/e_{\text{aq}}^-) = -2.87 \text{ V}_{\text{NHE}}$ (Normal Hydrogen Electrode) and $E^\circ(\text{H}^+/\text{H}^\bullet) = -2.3 \text{ V}_{\text{NHE}}$. These free radicals can reduce dissolved metal ions down to the zero-valent state (complete reduction).

During radiolysis of water, hydroxyl radicals (HO^\bullet), which are very strong oxidative species [$E^0(\text{HO}^\bullet/\text{H}_2\text{O}) = +2.8 \text{ V}_{\text{NHE}}$], are also formed. To avoid competitive oxidation reactions which may limit or even prevent the reduction process of metals (in general), hydroxyl scavengers must be added in the solution prior to irradiation. Among these scavengers, primary or secondary alcohols (such as 2-propanol) molecules or formate ions, which also react with hydrogen atoms, are generally used.



Due to their redox potentials [$E^0(\text{CH}_3)_2\text{CO}/(\text{CH}_3)_2\text{C}^\bullet\text{OH}) = -1.8 \text{ V}_{\text{NHE}}$ at pH 7, and $E^0(\text{CO}_2/\text{COO}^{\bullet-}) = -1.9 \text{ V}_{\text{NHE}}$], the radicals formed by reactions (5) and (6) are almost as powerful reducing agents as H^\bullet radicals to reduce the metal ions (M^+) following the reactions below



When a chemical agent generally chosen as an electron donor (D) is added to the medium, its redox potential $E^0(\text{D}^+/\text{D})$ in general is not negative enough to reduce directly isolated metal ions into atoms. Thus, it essentially reduces ions adsorbed on the nuclei,

which have more positive redox potential [reactions (1.9)–(1.11)]. Then a development process occurs, which results in larger clusters:



Therefore, the radiolysis technique can produce very small metal nanoparticles since solvent radiolysis leads to very strong reducing agents, which can effectively reduce metal ions into a zero-valent state metal.

I.2.3 Dose rate effect

In the case of metal nanoparticle synthesized by radiolysis (**Figure 1.2**), the nucleation and growth of the clusters depends on the dose rate, which fixes the reduction kinetics. At high dose rate, the reduction is very fast and followed by steps of coalescence of atoms separately created (**Figure 1.2a**). At low dose rate, the reduction is slower and association of M^+ ions with atoms can be faster than the production rate of reducing radicals (**Figure 1.2b**). Therefore, the reduction of M^+ ions occurs mostly *in situ* on clusters already formed M_{n+1}^+ .

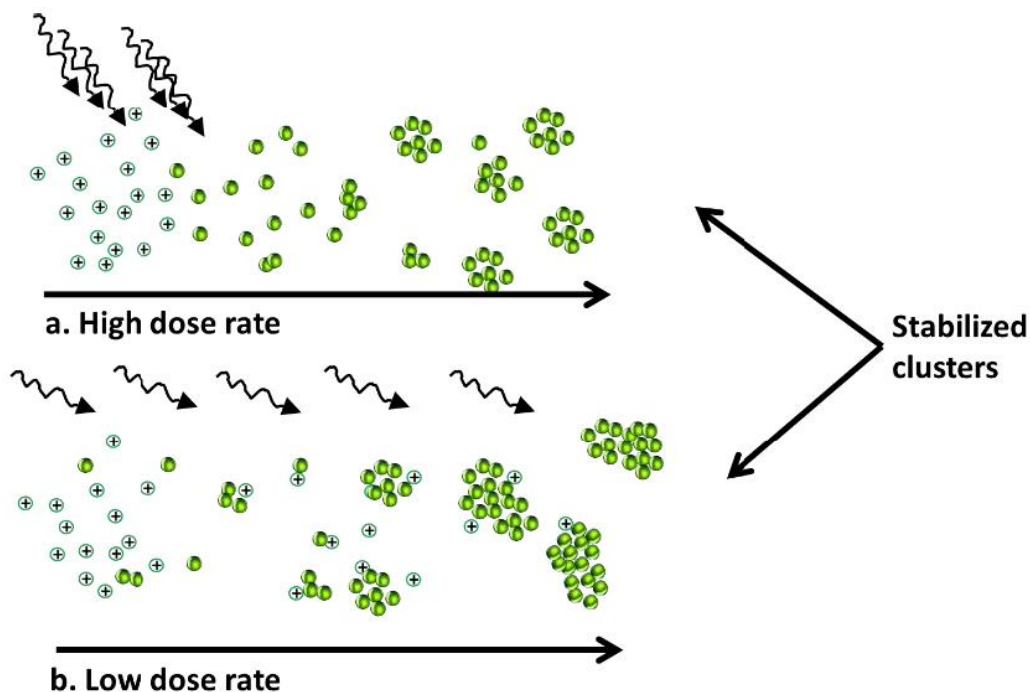


Figure 1.2. Nucleation and growth of clusters generated by radiolytic radicals at **a)** high and **b)** low dose rates.¹⁹

In the case of an irradiation-induced reduction process, when ions of two different metals are present in solution (**figure 1.3**), the competition reactions between those two metals will depend on the metal precursors and on the dose rate. At a low dose rate, the electron transfer occurs from the atoms of the less noble metal to the ions of the more noble metal, thus favoring the formation of bimetallic nanoparticles with a core-shell structure (the more noble metal being in the core). By contrast, at a high dose rate, the process of electron transfer from the less noble metal to the more noble metal can be prevented (due to fast reduction process) yielding alloyed clusters.^{20,21}

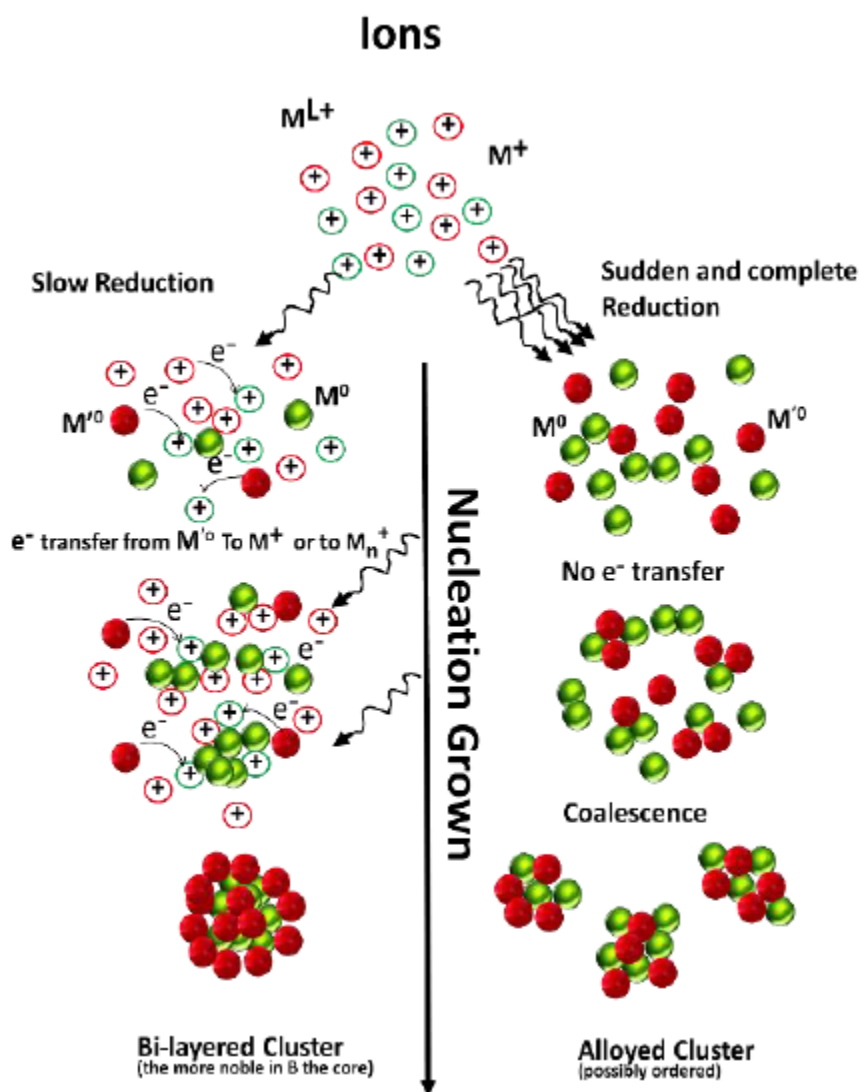


Figure 1.3. Scheme of the influence of the dose rate on the competition between the inter-metal electron transfer and the coalescence processes during the radiolytic reduction of mixed metal ion solutions. High dose rates favor alloying, whereas low dose rates favor core-shell segregation of the metals in the nanoparticles.²²

I.2.4 Synthesis of nanomaterials using templates

Synthesis of porous materials attracts a lot of interest for different applications: catalysis, electrocatalysis, sensing, drug delivery... To obtain a material with an organized and controlled porosity, a template synthesis is generally required. Different templates are available, and depending on their type and structure, a wide range of nanomaterials can be synthesized. There are three general steps for synthesis of nanomaterials using templates: (1) the template preparation, (2) the directed synthesis of the target material using the template, and (3) the template removal.²³ The templates are classified into two types: hard templates, which are constituted of solid materials, and soft templates, which are formed by self-assembly of molecules.

Hard templates

The most classical types of hard templates include porous aluminum oxide, carbon, titania, and even colloidal crystals made of polymers or silicates. For example, colloidal crystals, built out of self-assembled monodisperse polystyrene particles, have been used to produce 3D porous monometallic or Pt nanostructures that can be used as electrocatalysts in fuel cells (**Figure 1.4**).²⁴

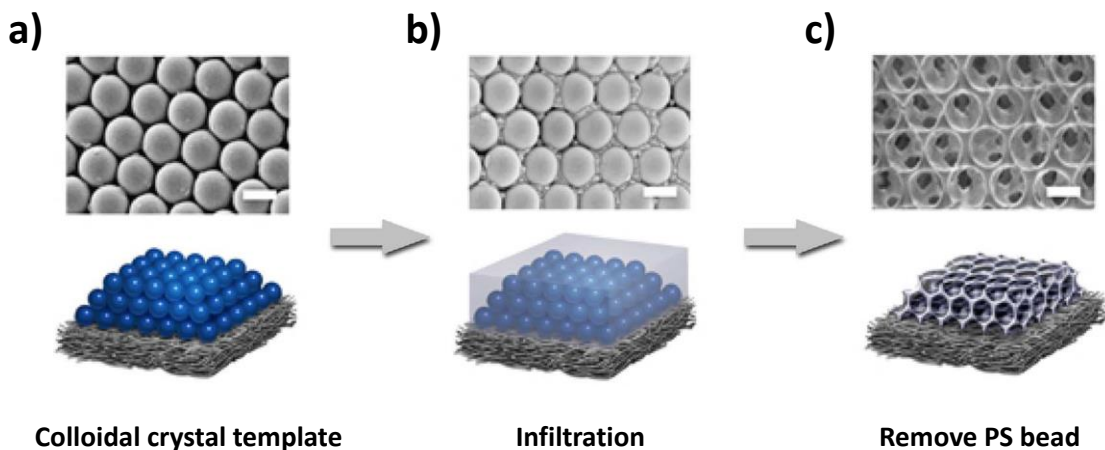


Figure 1.4 Schematic diagram of the fabrication process. (a) Self-assembly of a colloidal crystal template on GDL (gas diffusion layer). (b) Infiltration and pulse electrodeposition. (c) Removal of colloidal crystal template by soaking in toluene. Scale bar, 500 nm.²⁴

Bimetallic nanostructures have been previously obtained using hard templates. For instance, porous AuPd structures have been successfully synthesized by successive deposition of Au and Pt inside porous silica SBA-15 (two dimensional hexagonal

mesoporous silica) used as a hard template. The porous nanomaterial is then extracted by dissolution of silica (**Figure 1.5**).²⁵

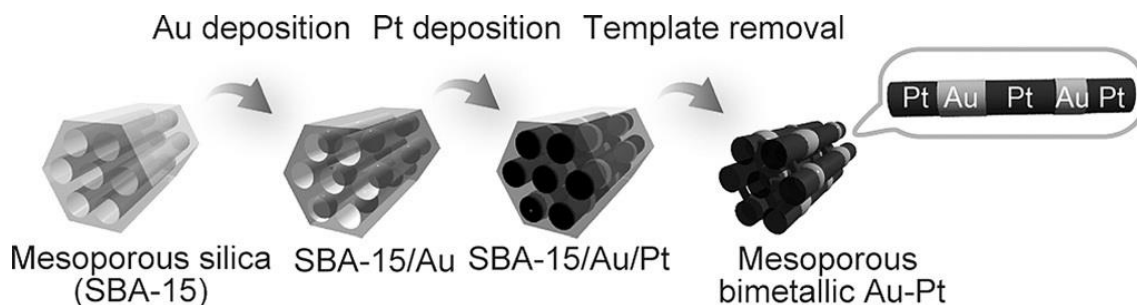


Figure 1.5 Preparation of mesoporous bimetallic Au–Pt with a phase-segregated heterostructure.²⁵

Hard templates such as track-etch polycarbonate or polyester membranes and anodic aluminium oxide membranes have been employed for the synthesis of controllable nanorods, nanofibers, nanotubes of conjugated polymers such as PANI (polyaniline), PEDOT (poly(3,4-ethylenedioxythiophene), PPy (Polypyrrole), P3HT (poly(3-hexylthiophene)) etc.^{26,27} Other materials such as zeolites, silica-based mesoporous molecular sieves, metal oxides, polyoxometallates, solid porous materials can also be used as hard templates for the synthesis of nanostructures.^{26,28,29} Here, nanostructures grow inside the pores or channels of a membrane, in order to control their size and shape.

However, one of the major drawbacks of using hard templates lies on the extraction process, which requires the use of harsh chemical agents that can alter the synthesized nanostructures. An alternative way to obtain metal or polymer nanostructures is by using soft templates, based on the self-assembly of surfactants or amphiphilic block copolymers.³⁰ Unlike with hard templates, the extraction process of these soft templates is very easy, as the synthesized materials can be extracted by simple addition alcohol (ethanol or 2-propanol) to the template and washing with the alcohol.

I.3 Soft templates: Swollen hexagonal mesophases

Thermotropic liquid crystals are molecular liquid crystals whose phase transitions are governed by temperature. By contrast, in lyotropic liquid crystals, made by a surfactant (or a mixture of surfactants in a solvent) the main control parameter is the concentration. Consequently, depending on their composition, different types of liquid

crystals with different symmetries, such as hexagonal, cubic, lamellar, etc.. can be formed. Swollen hexagonal mesophases are made of quaternary systems namely surfactant, brine, oil, and co-surfactant.

1.3.1 Surfactant

Surfactant is an abbreviation for surface active agent, which literally means active at the surface.³¹ Surfactant molecules are used to lower the free energy at the phase boundary. Surfactants are amphiphilic, which means that the molecules consist of at least 2 parts: a hydrophilic head group and a hydrophobic tail. The hydrophobic tail is usually a carboxylic chain.

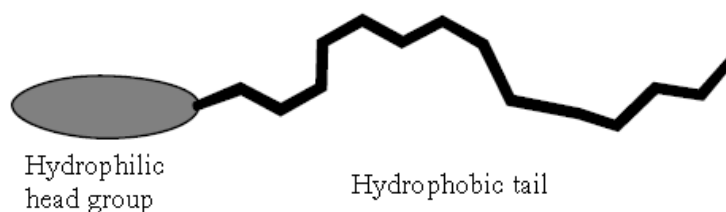


Figure 1.6 Schematic illustration of a surfactant³¹

Surfactants can be classified depending on the nature of the polar head groups, which can be anionic, nonionic, cationic, or zwitterionic.

a. Anionic surfactants

Carboxylates, sulfates, sulfonates, and phosphates are polar groups found in anionic surfactants. The most commonly used counterions are sodium, potassium, ammonium, calcium, and various protonated alkyl amines. **Figure 1.7** shows the chemical structure of sodium dodecyl sulfate (SDS), one the more common surfactant types belonging to this class.

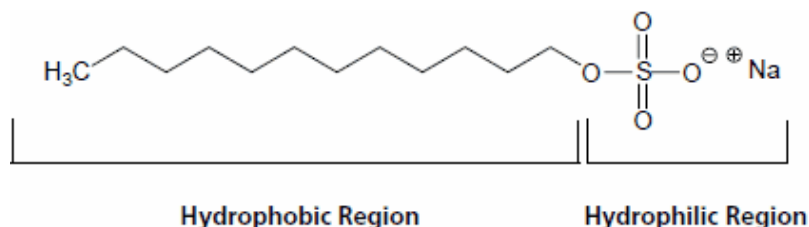


Figure 1.7 An example of anionic surfactant: sodium dodecyl sulfate (SDS)³²

b. Nonionic surfactants

Most non-ionic surfactants have a polyhydroxyl or polyether (consisting of oxyethylene units, made by polymerization of ethylene oxide) polar head.

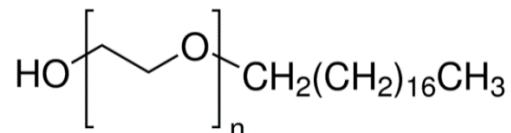
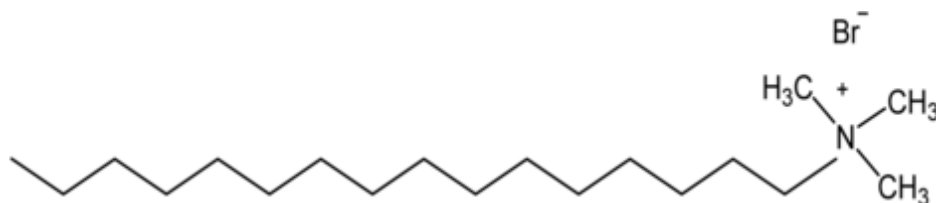


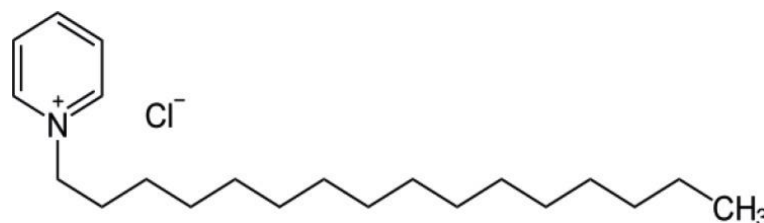
Figure 1.8 An example of nonionic surfactant: Polyoxyethelene glycol (hydroxyl group).³³

c. Cationic surfactants

The vast majority of cationic surfactants are based on the nitrogen atom carrying the cationic charge. Both amine and quaternary ammonium-based products are common.



Cetyl ammonium bromide (CTAB)



Cetyl pyridinium chloride (CpCl)

Figure 1.9 Two examples of cationic surfactants: cetyl ammonium bromide (CTAB)³⁴ and cetyl pyridinium chloride (CpCl).³⁵

d. Zwitterionic (amphoteric) surfactants

Zwitterionic (amphoteric) surfactants have both cationic and anionic centers attached to the same molecule. The cationic part is based on primary, secondary, or tertiary amines or quaternary ammonium cations. The anionic part can be more variable and include sulfonates, as in the sultaines CHAPS (3-[(3-Cholamidopropyl) dimethylammonio]-1-propanesulfonate) and cocamidopropyl hydroxysultaine. Betaines

such as cocamidopropyl betaine have a carboxylate with the ammonium. The most common biological zwitterionic surfactants have a phosphate anion with an amine or ammonium, such as phospholipids, phosphatidylserine, phosphatidylethanolamine, phosphatidylcholine, and sphingomyelins.

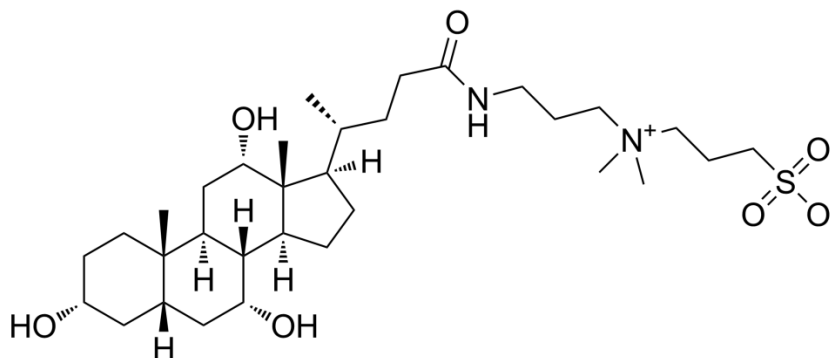
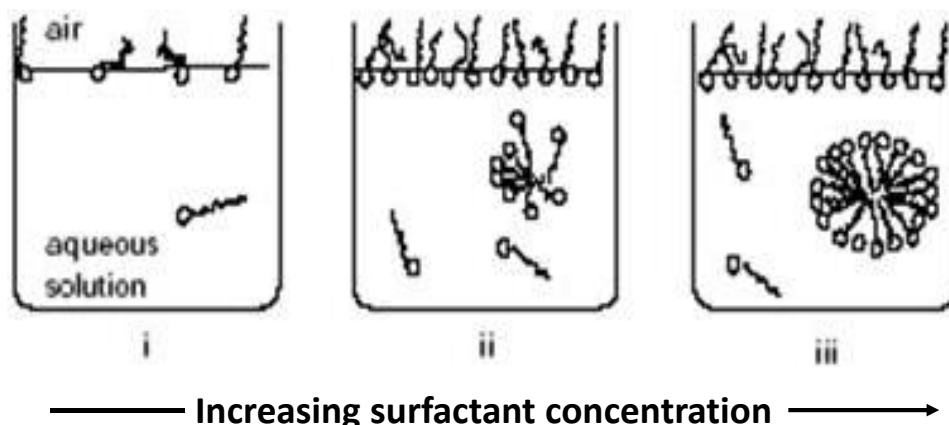


Figure 1.10 An example of zwitterionic (amphoteric) surfactant: CHAPS (3-[(3-Cholamidopropyl) dimethylammonio]-1-propanesulfonate) (anionic part).³⁶

1.3.2 Surfactant self-assembly

Surfactant molecules cover the air/water interface where the hydrophobic tails point to air and the polar head remains in contact with water. When the surfactant concentration increases, surfactant molecules disperse in water. As the surfactant concentration increases, an aggregate called micelle is formed, where the hydrophilic head groups are in contact with water, and the hydrophobic tails are in the center of the aggregate and protected from the water. The driving force of micelle formation is the elimination of the contact between the hydrophobic tails and water. The radius of a micelle is equal to the elongated length of hydrophobic tail.³⁷ The concentration where micelle starts to form is called critical micelle concentration (CMC). Different surfactants have different CMC values. **Figure 1.11** presents the formation of a micelle in water.



*Figure 1.11 Micelle formation*³⁷

Spherical micelles, as shown in **figure 1.12**, are one possibility of surfactant self-assembly. At higher surfactant concentrations or for different types of surfactant, different shapes of micelle may form. To understand the different structure of micelles that may form, it is convenient to introduce the critical packing parameter (CPP).

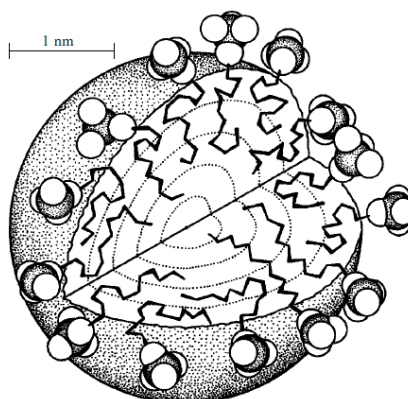


*Figure 1.12 An illustration of spherical micelle (for dodecyl sulfate) emphasizing the liquid-like character with a disordered hydrocarbon core and rough surface.*³⁸

1.3.3 Critical packing parameter (CPP)

CPP is the most important parameter to determine the self-assembly behavior of surfactant molecules in a solvent and was proposed by Israelachvili and co-workers.^{39,40} CPP can be interpreted as the ratio between the cross-sectional area of the hydrocarbon part and that of the head group (the hydrophilic part). Estimating the CPP enables us to determine the surfactant molecular packing and preferred geometrical structure such as spherical micelles, cylindrical micelles, bilayers, reversed micelles, etc. The illustration

of CPP is given in **Figure 1.13**. Analysis of different geometrical shapes of aggregates, leads to simple rule presented to predict the shape of the micelles, as illustrated in Table 1.1.

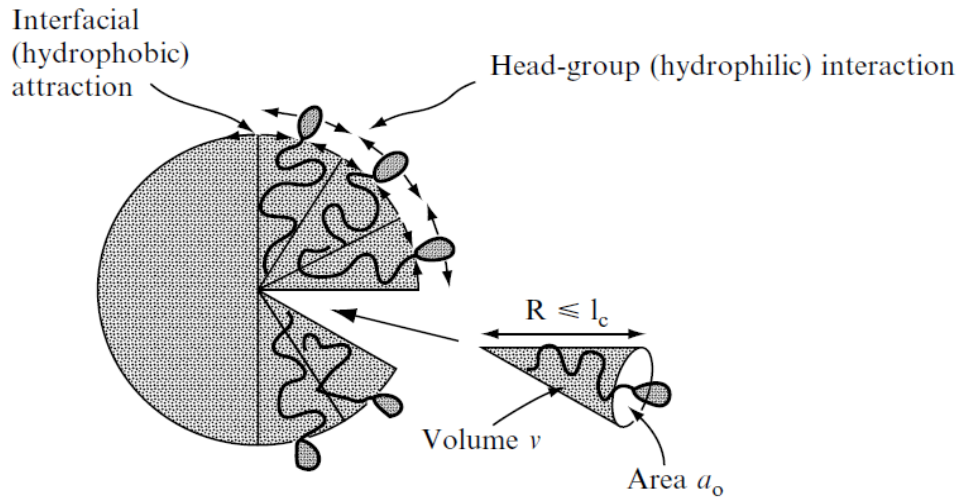
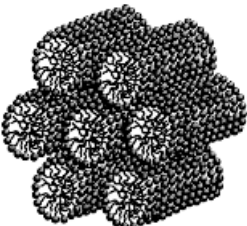
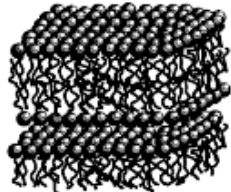
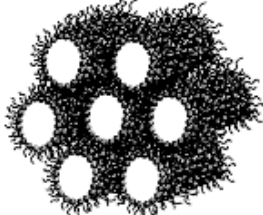
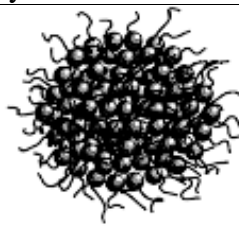


Figure 1.13 The critical packing parameter (CPP) or surfactant number relates the head group area, a_0 , the extended length, l_c , and the volume v of the hydrophobic part of a surfactant molecules into dimensionless number $CPP = v / (l_c a_0)$.³⁸

The interactions between the head groups in the aggregate are another factor that can affect the preferred geometrical structures. A strongly repulsive interaction between the head groups will drive an aggregate to the left in Fontell scheme, while the opposite applies for attractive interactions.

Table 1.1 Critical packing parameter (CPP) of surfactant molecules and preferred aggregate structures for geometrical packing reasons⁴¹

Critical packing parameter (v/a_0c)	Critical packing shape	Structures formed
$< 1/3$		 Spherical micelles
$1/3 - 1/2$		 Hexagonal phase (cylindrical micelles)
$1/2 - 1$		 Lamellar phase (sheet-like micelles)
≥ 1		 Cubic
> 1		 Reverse hexagonal phase (reverse cylindrical micelles)
		 Reverse spherical micelles

Fontell scheme for surfactant self-assembly (**Figure 1.14**) clearly represents the normal and reverse mesophase formation.

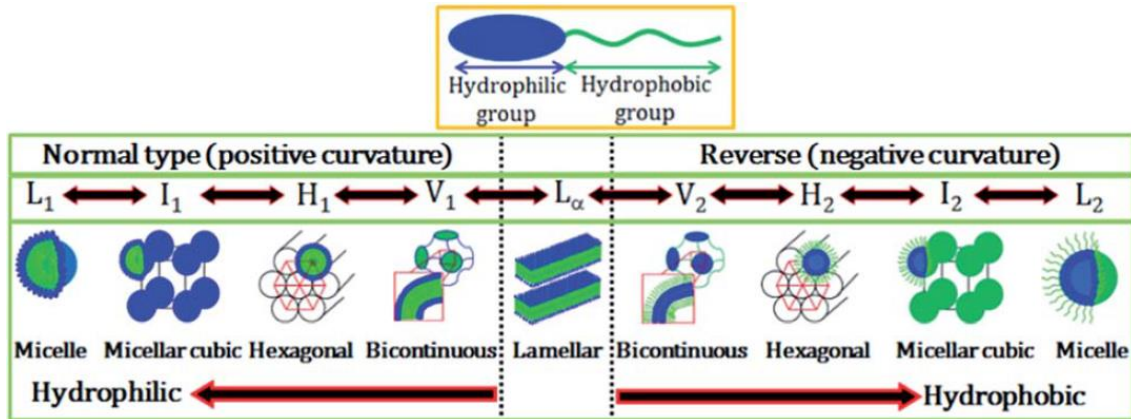


Figure 1.14 Schematic representation of an amphiphilic molecule and normal and reverse type of surfactant self-assembled structures. L_1 , I_1 , H_1 , V_1 , and L_α represents normal micelle, micellar cubic phase, hexagonal phase, bicontinuous cubic phase, and lamellar phase, respectively. V_2 , I_2 , H_2 , and L_2 respectively represent reverse (inverted) phases.⁴²

1.3.4 Self-assembly in hexagonal mesophases

In a mixture of surfactant, water and oil, the micelles formation strongly depends on the ratio between the three components, as illustrated in the phase diagram shown in **Figure 1.15**.

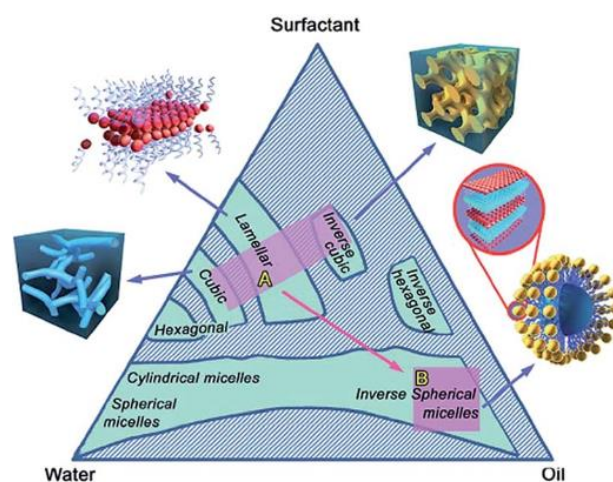


Figure 1.15 A three component (water, oil, surfactant) phase diagram showing the formation of micelles and mesophases by the self-assembly of surfactants.⁴³

Direct hexagonal phases consist of surfactant tubes regularly arranged on a triangular lattice in water. The structure is intermediate between a liquid phase and a crystalline phase. This is the reason why it is referred to as a liquid crystalline phase, or mesophase.

There are several factors affecting the formation of hexagonal mesophases:

- Polar head group interaction
- Salt concentration
- Nature of the counterion
- Co-surfactant

The self-assembly of hexagonal mesophases is illustrated in **Figure 1.16**. A high concentration of surfactants in water (containing salt or not) will lead to the formation of micelles. When oil is added to the micelles, an unstable emulsion (oil drops in water) is formed. The addition of a small amount of co-surfactant (small molecule of alcohol that goes at the air/oil interface, as a surfactant molecule) will lead to the self-assembly in hexagonal mesophases. The co-surfactant helps to balance the interaction between the head groups of the surfactant molecules.

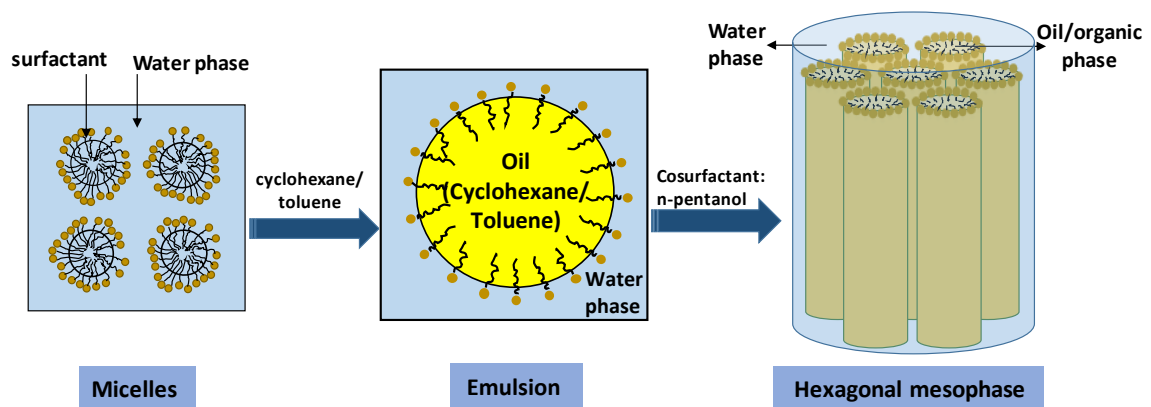


Figure 1.16 Formation of hexagonal mesophases

1.3.5 Characterization of hexagonal mesophases by Small Angle X-Ray Scattering (SAXS)

Characteristics of swollen hexagonal mesophases

There are several characteristic parameters of a hexagonal mesophase:

- Diameter of oil tube (D);
- The distance between the center of the adjacent tubes (d_c);
- The water channel between the two adjacent tubes (e) ($d_c = D + e$).

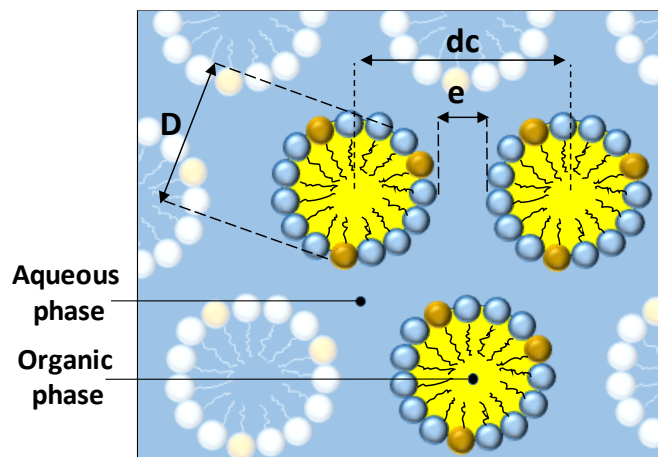


Figure 1.17 Scheme of the cross-section of a hexagonal mesophase.

The formation of hexagonal mesophases can be confirmed by observation of their texture using a polarized optical microscopy. The pattern and orientation formed can clarify the formation of hexagonal mesophases. However, this technique cannot be used to quantify the geometric parameters of the mesophase. Small angle X-ray scattering (SAXS) are used to characterize the mesophases. The positions of the Bragg peaks define the symmetry of the mesophase. For hexagonal mesophases, the positions of the successive Bragg peaks are in the ratio of 1, $\sqrt{3}$, and 2.

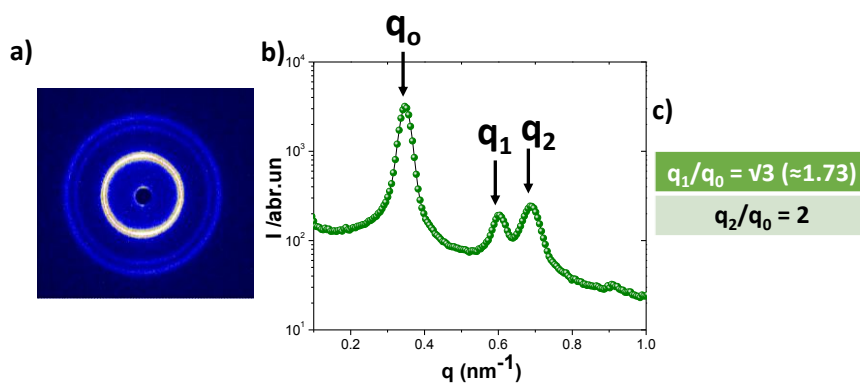


Figure 1.18 Example of SAXS spectra of a hexagonal mesophase; **a)** 2D scattering pattern; **b)** scattering profile, scattered intensity as a function of the wavevector, obtained by integration of the scattering pattern shown in a; **c)** calculation of the ratio between the peak positions.

The distance between the center of two adjacent tubes (d_c) is given by equation 1.1.

$$d_c = \frac{4\pi}{(\sqrt{3}) * q_0} \quad (\text{Equation 1.12})$$

where q_0 is the position of the first Bragg peak as determined from the SAXS spectrum.

The diameter of the oil tube (D) can thus be calculated using equation 1.2.

$$D = 2 * d_c * \sqrt{\left(\frac{\sqrt{3}}{2\pi}\right) * (1 - \phi_p)} \quad (\text{Equation 1.13})$$

Here ϕ_p is the volume fraction of the polar phases comprising the aqueous phase, the polar head group of the surfactant and cosurfactant molecules, relative to the total volume (equation 1.3).

$$\phi_p = \frac{V_{\text{aqueous phase}} + V_{\text{polar head of surfactant}} + V_{\text{polar head of co-surfactant}}}{V_{\text{total}}} \quad (\text{Equation 1.14})$$

Where for CTAB, the volume of one polar head group is 102 \AA^3 and the volume of one polar head group of 1-pentanol is 20.3 \AA^3 .

The thickness of water channel (e) can be calculated subtracting the distance between two adjacent tubes with the diameter of oil tube.

$$e = d_c - D \quad (\text{Equation 1.15})$$

1.3.6 Swollen hexagonal mesophases

One interesting property of hexagonal mesophases lies on their ability to be swollen. The tube diameter can be controlled by varying the ratio between the volume of oil to that of water (O/W). In our experiment, the volume of water is kept constant, while varying the volume of oil. To keep the mesophases stable, while increasing the volume of oil, the spontaneous curvature of the surfactant monolayer has to be varied concomitantly. This can be done by changing the ionic strength of the aqueous phase when using an ionic surfactant. Therefore, the salt concentration must be increased when increasing the O/W ratio.⁴⁴ **Figure 1.19** shows the scheme of the cross-section of a

hexagonal mesophase (a) and the tubes of mesophases arranged in a hexagonal lattice structures when the volume of oil is increased (b).

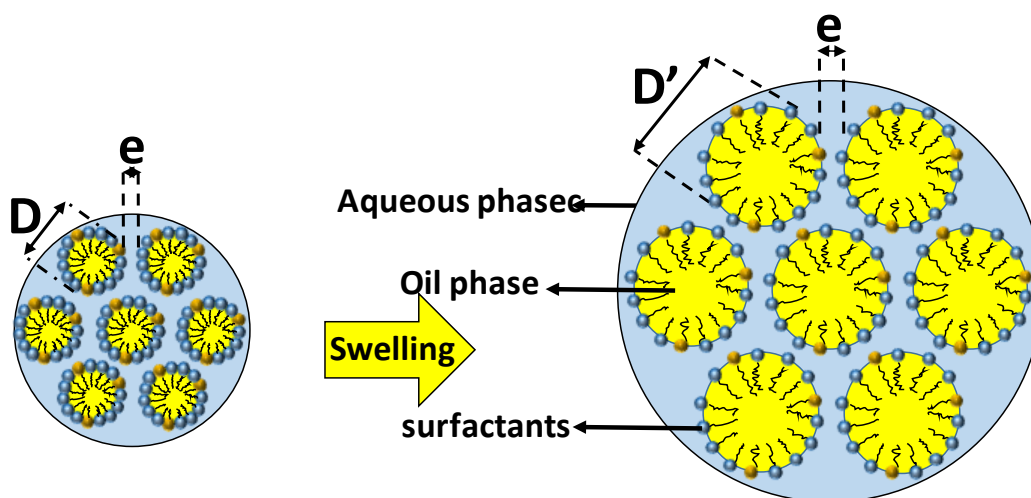


Figure 1.19 The scheme of the cross-section of hexagonal mesophases in a hexagonal lattice structures when the volume of oil is increased.

I.4 Synthesis of nanomaterials in hexagonal mesophases

Several nanomaterials including metal and conjugated polymer nanostructures have been successfully synthesized in the soft template hexagonal mesophases.^{16,17,45–49} Metals, which precursors are in general soluble in water, are synthesized in the confined aqueous phases of hexagonal mesophases. By contrast, the conjugated polymers, which monomers are soluble in oil, are polymerized in the oil phase of hexagonal mesophases.

I.4.1 Synthesis of porous metal nanostructures in the water phase of hexagonal mesophases

Swollen hexagonal mesophases can be doped with high concentrations of metal ions or complexes.^{44,50} The reduction of metal ions confined in the water phase has led to synthesis of 1D- 2D- or 3D-metal nanostructures such as Pd nanowires, Pd nanosheets Pd nanoparticles, Pd nanoballs, Pt nanoballs, PdPt nanoballs, AuPd core-shell.^{15,16,45,48,49,51} Those metals were synthesized by radiolysis (except Pd nanosheets which were synthesized through the reaction with CO) without any addition of reducing agents (the reducing species are induced by solvent radiolysis). Several factors can affect the shape of metal nanostructures formed in hexagonal mesophases such as the nature of

surfactants, the nature of metal precursors and the dose rate of radiation, which will be discussed in the following section.

I.4.1.1 The role of surfactants

Previous studies in our group have shown that a specific cationic surfactant (cetyl trimethyl ammonium bromide, CTAB) is essential to obtain porous Pd and Pt nanoballs (formed by 3D-connected nanowires and synthesized in hexagonal mesophases).^{16,48} Other shapes of Pd and PdPt nanostructures were obtained using mesophases based on other cationic surfactants such as cetylpyridinium chloride (CpCl), cetylmethylammonium chloride (CTAC) and cetylpyridinium bromide (CpBr). Experiments conducted with CpCl gave small Pd particles with diameters around 3 nm.¹⁶ Nanostructures made of less ordered Pd or Pt parallel nanowires were obtained with CTAC and formation of nanoballs were not observed in this case. In the case of CPBr, the obtained nanostructures were spherical aggregates made by nanoparticles of diameter 3 to 4 nm.⁴⁸

Figures 1.20 and 1.21 show TEM images of Pd nanostructures and PdPt nanostructures (with the atomic ratio Pd/Pt = 1/1) synthesized in hexagonal mesophases using different surfactants. Porous PdPt nanoballs can only be obtained using CTAB as surfactant. CTAB plays the role of structure-directing agent: It is known to favor formation of anisotropic nanostructures by preferential adsorption on (100) facets.^{52,53}

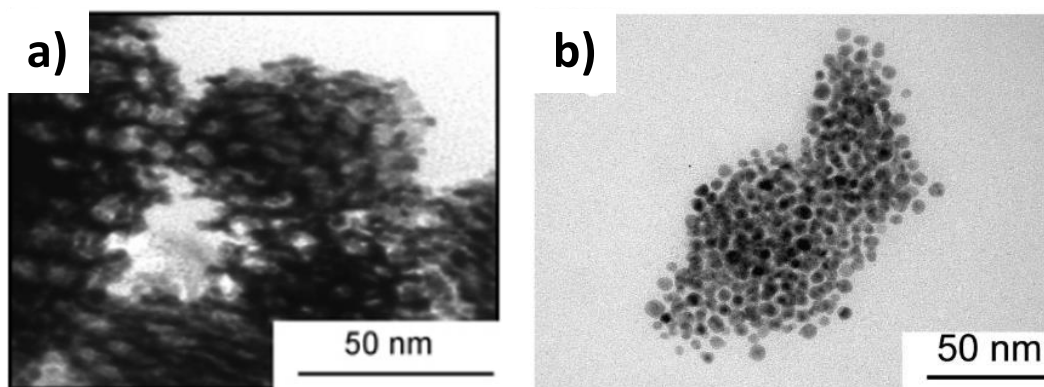


Figure 1.20 Different shapes of Pd nanostructures synthesized with different surfactants: a) Pd nanoballs synthesized using CTAB; b) Pd nanoparticles synthesized using CpCl.¹⁶

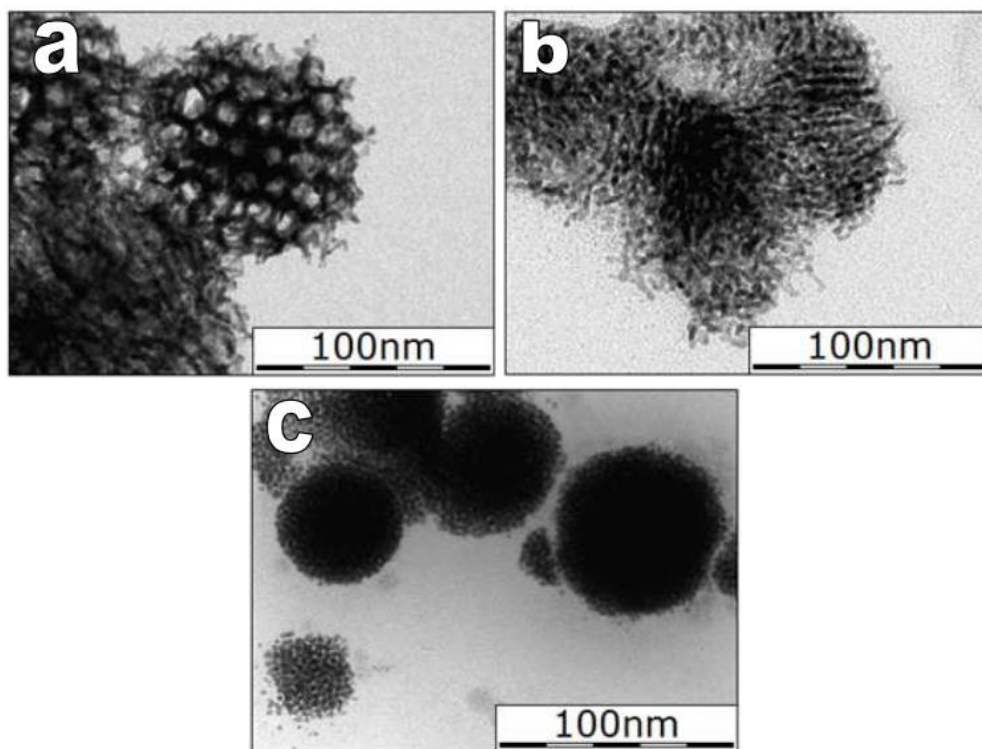


Figure 1.21 TEM images of Pd-Pt nanostructures ($Pd/Pt = 1:1$) synthesized in hexagonal mesophases based on different cationic surfactants and containing 0.1 M of metal salts, ($O/W=1.5$): (a) CTAB, (b) CTAC and (c) CpBr after 48 h irradiation with dose rate of 1.85 kGy/h (total dose: 88.8 kGy) under N_2 atmosphere.⁴⁸

1.4.1.2 The role of the dose rate

The dose rate fixes the reduction kinetics. A slow reduction kinetics provided by low dose rate is necessary for the formation of nanoballs.^{16,45} Palladium nanowires (**Figure 1.22a**) were synthesized using electron beams (which deliver a very high dose rate (48 kGy/h)) in hexagonal mesophases with CTAB as the surfactant (the same surfactant used to synthesize palladium nanoballs), whereas Pd nanoballs (**figure 1.22b**) were synthesized in mesophases using a low dose rate (1.85 kGy/h).^{16,45}

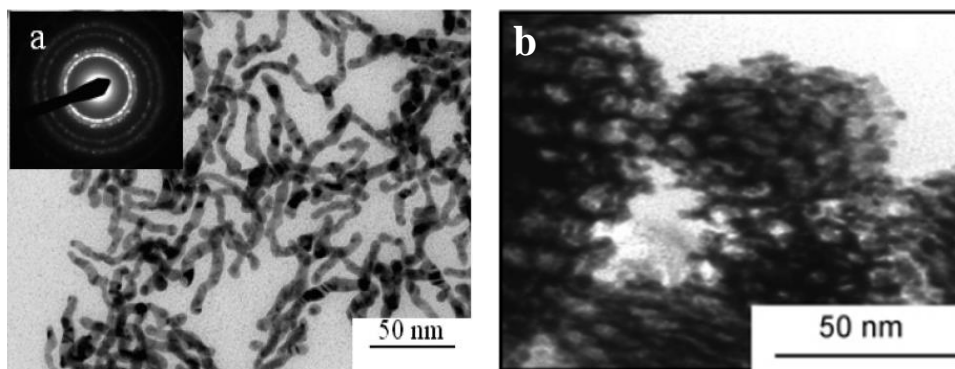


Figure 1.22 TEM images of palladium nanostructures synthesized in hexagonal mesophases using different dose rates; a) Pd nanowires synthesized using electron beam with 48 kGy/h dose rate, b) Pd nanoballs synthesized using gamma radiation with 2.2 kGy/h dose rate.^{16,45}

I.4.2 Synthesis of conjugated polymer nanostructures in the oil phase of hexagonal mesophases

Conjugated polymer nanostructures such as PDPB (Poly(diphenylbutadiene)) and PEDOT (poly(3,4-ethylenedioxythiophene)) for application in photocatalysis have been successfully synthesized in the oil phase of hexagonal mesophases.^{17,46,47,54} Depending on the ratio of oil to water (O/W) different diameter size/shapes of conjugated polymer nanostructures can be formed.

PDPB nanostructures were synthesized through a radical induced polymerization process. The formation of radicals is induced by either gamma irradiation or UV light. The diameter of the PDPB nanostructures can be tuned by controlling the O/W ratio in the soft template hexagonal mesophases. The higher the O/W ratio, the bigger the diameter of PDPB nanostructures is (**Figure 1.23**), as expected from a direct templating approach, since the synthesis takes place in the oil phase.¹⁷

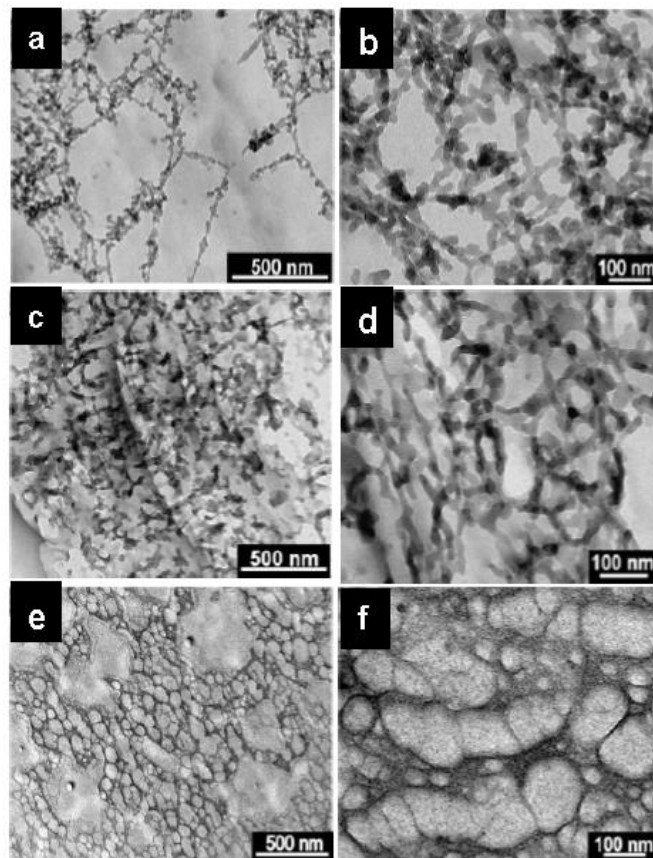


Figure 1.23 Transmission electron micrographs of PDPB nanostructures prepared by UV-irradiation in mesophases with (a, b) $O/W = 2.21$, (c, d) $O/W = 0.98$, and (e, f) $O/W = 0.72$.¹⁷

PEDOT nanostructures were synthesized by a chemical polymerization process (by oxidation polymerization process using oxidant FeCl_3). Depending on the O/W ratio, different shapes of PEDOT nanostructures can be formed. Vesicle-like structures were synthesized in mesophases with $O/W = 1.5$, while PEDOT nanospindles were synthesized with $O/W = 2.5$ (Figure 1.24).⁴⁷

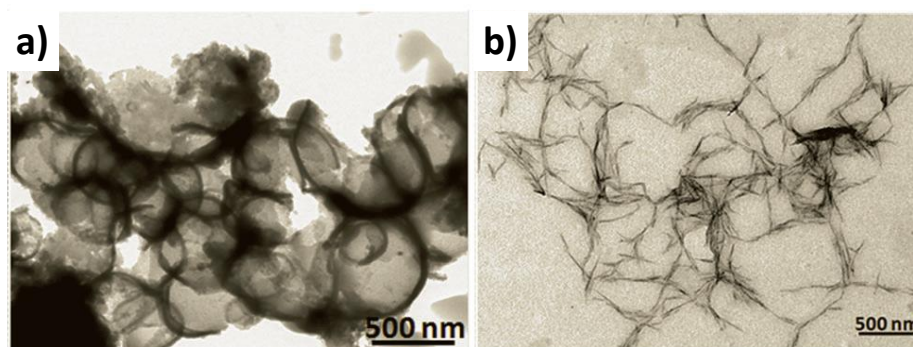


Figure 1.24 TEM images of PEDOT vesicles (a) and PEDOT nanospindles (b).⁴⁷

Synthesis of metal, polymer, and metal-polymer nanostructures in these soft templates and their applications will be discussed in chapters III, IV, and V. Several mono-, bi- and trimetallic nanostructures will be used as electrocatalysts for several reactions involved in fuel cells, while conjugated polymers are used as photocatalytic materials for water depollution

CHAPTER II

Experimental Part

CHAPTER II

Experimental Part

All the chemical products and solvents used for the experiments are shown in Table 2.1

Table 2.1 List of chemical products and solvents and their specification

Chemical product	Chemical formula	Molar mass (g/mol)	Purity	Company
Cetyltrimethylammonium bromide (CTAB)	C ₁₉ H ₄₂ BrN	364.45	≥98%	Sigma-Aldrich
Sodium dodecyl sulphate (SDS)	NaC ₁₂ H ₂₅ SO ₄	288.372	98.5%	Sigma-Aldrich
Cetylpyridinium chloride (CpCl)	C ₂₁ H ₃₈ ClN	339.99		Sigma-Aldrich
Cyclohexane	C ₆ H ₁₂	84.16	≥99%	Sigma-Aldrich
Toluene	C ₆ H ₅ -CH ₃	92.14	≥99%	Sigma-Aldrich
Sodium chloride	NaCl	58.44	99.5%	Sigma-Aldrich
Tetraaminepalladium (II) dichloride	Pd(NH ₃) ₄ Cl ₂ .H ₂ O	263.46	99.99%	Sigma-Aldrich
Tetraamineplatinum (II) dichloride	Pt(NH ₃) ₄ Cl ₂ .H ₂ O	352.11	99.99%	Alfa chemical
	HAuCl ₄ .3H ₂ O	393.83	99.9%	Sigma-Aldrich
Ethylene diamine	C ₂ H ₈ N ₂	60.10	>99.55%	Sigma-Aldrich
Anhydrous ethylic ether	(C ₂ H ₅) ₂ O	74.12	>99.7%	Sigma-Aldrich
Nickel formate	Ni(HCO ₂) ₂ .2H ₂ O	184.77		
1-pentanol	C ₅ H ₁₂ O	88.15	>99%	Sigma-Aldrich
Ethanol	C ₂ H ₆ O	46.06	≥99%	Sigma-Aldrich
2-propanol	C ₃ H ₈ O	60.1	≥99%	Sigma-Aldrich
3-hexylthiophene (3HT)	C ₁₀ H ₁₆ S	168.30	≥99%	Sigma-Aldrich
1,4-Diphenyl buadiyne (DPB)			99%	Sigma-Aldrich
Iron chloride	FeCl ₃	162.20	97%	Sigma-Aldrich
Titania (P25) (80% Anatase, 20% Rutile and a small amount of amorphous TiO ₂)	TiO ₂	79.87		Evonic

Rhodamine B	C ₂₈ H ₃₁ ClN ₂ O ₃	479.02		Fluka
Phenol	C ₆ H ₅ OH	94.11		Sigma-Aldrich
Potassium hydroxide	KOH	56.10	99.5%	Sigma-Aldrich
Nitrogen	N ₂	28.0		Air liquid
Oxygen	O ₂	32.0		Air liquid
Ultra-pure water	H ₂ O	18.0		Millipore System, 18.2 MΩ cm

II.1 Preparation of hexagonal mesophases

Hexagonal mesophases were prepared following the previous published method.^{50,55} Initially, surfactant was dissolved in water (with or without salt). The mixture was vortexed for a few minutes, then put in the oven to reach the equilibrium (the temperature of the oven will depend on the type of surfactant; 50°C for CTAB, 30°C for SDS, and 40°C for CpCl). A certain amount of oil (here we used either cyclohexane or toluene) was added to the mixture under vortex. The addition of n-pentanol as cosurfactant led to a perfectly birefringent and transparent gel, a hexagonal mesophase.

II.1.1 Synthesis of metal nanostructures in the aqueous phase of hexagonal mesophases for application in fuel cells

Porous metal nanostructures such as PdPt, AuPd, AuPt, AuPdPt, and PtNi are synthesized in hexagonal mesophases through radiolysis technique. The precursors of metallic salts are dissolved in the aqueous phase. The ratio of oil to water in hexagonal mesophases can be adjusted, thus allowing us to control the pore size of metal nanostructures. In the synthesis of bimetallic PdPt, the ratio of oil to water in hexagonal mesophases is varied from 1.5 to 4.5. Hence, we expect to have different pore size for the PdPt bimetallic nanostructures.

a. Swollen hexagonal mesophases containing Pd and Pt

The mesophases are prepared following the procedure described above. Here we used CTAB as surfactant, n-pentanol as co-surfactant, cyclohexane as the oil phase, and water containing metallic salts and eventually NaCl. The total metallic salt concentration (Pd(NH₃)₄Cl₂ and Pt(NH₃)₄Cl₂) is kept at 0.1 M. The ratio of Pd to Pt is varied as shown in **Table 2.2**.

Table 2.2 Pd/Pt composition to prepare Pd, Pt, and Pd/Pt nanoballs

CTAB	Aqueous phase					Cyclohexane (mL)	n-pentanol (μ L)
	water	Pd/Pt composition	Pd(NH ₃) ₄ Cl ₂ (M)	Pt(NH ₃) ₄ Cl ₂ (M)	[NaCl] (M)		
1.03 g	2 mL	100% Pd	0.1	0	0	2.98	240
		100% Pt	0	0.1	0	2.98	240
		(Pd ₅₀ Pt ₅₀)	0.05	0.05	0	2.98	240
		(Pd ₂₅ Pt ₇₅)	0.025	0.075	0	2.98	240
		(Pd ₇₅ Pt ₂₅)	0.075	0.025	0	2.98	240

In order to obtain porous PdPt nanoballs with different pore sizes, the tube of hexagonal mesophases is swollen by varying the ratio of oil to water as shown in **Table 2.3**.

Table 2.3 Composition to prepare hexagonal mesophases with different oil to water ratios

CTAB	Aqueous phase				Cyclohexane (mL)	O/W	n-pentanol (μ L)
	Water	Total Pd-Pt (M)	[NaCl] (M)	[Total salt] (M)			
1.03 g	2 mL	0.1 M	0	0.1	2.98	1.5	240
			0.1	0.2	4	2	240
			0.2	0.3	5	2.5	250
			0.3	0.4	6.5	3.25	260
			0.4	0.5	7.5	3.75	260
			0.5	0.6	9	4.5	260

b. Preparation of hexagonal mesophases containing AuPd, AuPt, and AuPdPt

Here we also used CTAB as surfactant, n-pentanol as co-surfactant, cyclohexane as the oil phase, and water containing metallic salts. The compositions of metallic salt, cyclohexane, and co-surfactant, (1-pentanol) are shown in **Table 2.4**.

Table 2.4 Composition to prepare hexagonal mesophases doped with Au, Pd, and Pt precursors.

CTAB	Aqueous phase					cyclohexane (mL)	n-pentanol (μ L)
	V of water	Au/Pd/Pt composition	[Au(en) ₂] Cl ₃	Pd(NH ₃) ₄ Cl ₂	Pt(NH ₃) ₄ Cl ₂		
1.03 g	2 mL	Au ₅ Pd ₉₅	0.005	0.095	0	2.98	240
		Au ₁₀ Pd ₉₀	0.01	0.090	0	2.98	240
		Au ₅ Pt ₉₅	0.005	0	0.095	2.98	240
		Au ₁₀ Pt ₉₀	0.01	0	0.090	2.98	240
		Au ₅ Pd ₇₀ Pt ₂₅	0.005	0.070	0.025	2.98	240

The precursor of gold (ethylenediamine (gold(III) ([Au(en)₂]Cl₃)) is synthesized following the previous published method.⁵⁶ 0.5 mL of ethylene diamine (purity >99.5%) diluted by 2.5 mL anhydrous ethylic ether (>99.7%) is added to a solution containing 0.5g of HAuCl₄·3H₂O and 5 mL of ether. A yellow gum precipitates. The upper solution is discarded and the precipitate is dissolved in 0.5 mL of distilled water. The complex [Au(en)₂]Cl₃ precipitates with the addition of 5 mL of glacial ethanol. The process of solubilization-precipitation is repeated 3 times. The yellow precipitate sample is dried on a filter Tamb, and kept in the dark.

c. Preparation of hexagonal mesophases containing PtNi

1.03 g of CTAB is mixed with 2 mL of water containing 0.085 M of Pt precursor (Pt(NH₃)₄Cl₂) and 0.015 M of Ni precursor (Nickel nitrate (Ni(NO₃)₂) or Nickel formate (C₂H₂NiO₄)) under continuous vortex. The mixture is then placed in an oven at T= 50°C for 1 h to reach a complete dissolution of the metallic salts. 2.98 mL of cyclohexane is added to the mixture under vortex leading to an unstable emulsion. The addition of \approx 240 μ L of n-pentanol as cosurfactant leads to a perfectly birefringent and transparent gel: a hexagonal mesophase.

Radiolytic synthesis of metal nanostructures in hexagonal mesophases

Hexagonal mesophases containing metallic complexes or salts are transferred into small vials, covered with rubber plastic septums, centrifuged for 15 minutes at 3000 rpm speed, and deoxygenized with N₂ flow for 10 minutes. The samples are then exposed to gamma irradiation for 24 hours at room temperature (the irradiation dose, 84 kGy, enables a complete reduction of the metal ions). Gamma irradiation is used as a technique to synthesize mono, bimetallic, and trimetallic nanostructures. The γ source located at Orsay is a ⁶⁰Co gamma-facility of 7000 Curies with a maximum dose rate of 3.5 kGy h⁻¹. Few samples are also prepared with electron beams at Elyse (Fast kinetics center in LCP) with a dose rate of 1062 kGy/h or 59 Gy/pulse (5 pulses/second). The color of the samples changes after irradiation from transparent to black. The nanomaterials are extracted from hexagonal mesophases using warm 2- propanol, centrifuged and washed (with warm 2- propanol) several times to remove the excess of surfactant and salt.

II.1.2 Synthesis of conjugated polymer nanostructures in the oil phase of hexagonal mesophases

a Synthesis of conjugated polymer P3HT (poly(3-hexylthiophene))

Poly(3-hexylthiophene) (P3HT) nanostructures (here after called nano P3HT) were synthesized inside the oil phase of hexagonal mesophases. The hexagonal mesophases were prepared following the previously published method with some modifications. To prepare the hexagonal mesophases, 1.03 g of CTAB was first dissolved in 2 mL of sodium chloride 0.1 M and then, vortexed for a few minutes. The mixture was then let in an oven at 50°C for 1 h to form a transparent and viscous micellar solution. Then, 1 mL of toluene containing 54 μ L of the 3HT monomer was added to the micellar solution under vortex. Subsequently, 2 mL of toluene containing 96 mg of FeCl₃ was added, and the mixture was vortexed for a few minutes. This led to an opaque unstable emulsion. The cosurfactant (20 μ L of n-pentanol) was added dropwise and strongly vortexed until an orange, translucent and birefringent gel (a hexagonal mesophase) was formed. The polymerization of 3-hexylthiophene was induced by oxidation with FeCl₃. To avoid bulk polymerization, the monomer and oxidizing agent were never put together, but instead were dissolved in toluene separately and then added to the mixture during the mesophase formation.

Synthesis of bulk P3HT

Bulk P3HT was synthesized in toluene without any surfactant. The ratio between monomer and oxidizing agent (FeCl_3) was the same as that used for the synthesis of nano P3HT in mesophases.

After polymerization, the materials were extracted by adding ethanol and water, followed by centrifugation and several washing (with ethanol and water) steps to remove the excess of surfactant and oxidant. The polymer was then extracted with ethanol and dried for one night at 40°C . The photocatalytic activity of nano and bulk P3HT was compared to that of plasmonic titania and PDPB nanowires. Plasmonic titania (TiO_2 modified with Ag nanoparticles) consist in small silver nanoparticles synthesized on TiO_2 (P25 (commercial TiO_2)) by radiolysis. The synthesis is described in details in a previous article.⁵⁷ PDPB nanowires were synthesized using swollen hexagonal mesophases as soft templates following the previously published method.⁵⁸

b Synthesis of nano PDPB (Poly(diphenylbutadiene) (as supporting polymer) in hexagonal mesophases

The PDPB conducting polymer nanostructures are synthesized inside the oil cylinder of hexagonal mesophases. 2 mL of brine (0.3 M NaCl) are mixed with SDS under vortex. 4.42 mL of cyclohexane containing 10% of DPB monomer (g/g) was added to the mixture leading to a white unstable emulsion. Co-surfactant ($\approx 417 \mu\text{L}$) was added dropwise. The mixture is vortexed. A transparent gel is formed: a hexagonal mesophase. The samples were then transferred into small vials, covered with rubber plastic septums, centrifuged, and deoxygenized with N_2 flow for few minutes. Gamma irradiation was used to induce the polymerization of PDPB. The dose necessary to complete polymerization of PDPB was 80 kGy (the dose rate follow the previously published article).¹⁷

II.1.3 Synthesis of Pt-PDPB nanocomposites in hexagonal mesophases

Pt-PDPB nanocomposites are synthesized in hexagonal mesophases following the procedure described above. 2 mL of water containing the Pt precursor (0.1 M of $\text{Pt}(\text{NH}_3)_4\text{Cl}_2 \cdot \text{H}_2\text{O}$) is mixed with 1 g of surfactant (CpCl) under vortex. The mixture is maintained at 40°C for 1 h. 3 mL of cyclohexane containing 10% of DPB monomer (g/d)

is added to the mixture leading to a white unstable emulsion. The co-surfactant ($\approx 340 \mu\text{L}$) is added dropwise. The mixture is vortexed. A transparent gel is formed: a hexagonal mesophase. The samples were then transferred into small vials, covered with rubber plastic septums, centrifuged, and deoxygenized with N_2 flow for 7 minutes. Gamma irradiation was used to reduce the metallic complexes of Pt and to induce the polymerization of PDPB. The dose necessary for complete reduction of Pt salt and polymerization of PDPB was 80 kGy.

II.2 Material characterizations

II.2.1 Small and Wide Angle X-Ray Scattering

The mesophases were analyzed using small angle X-Ray scattering (SAXS). The mesophases were inserted in glass capillaries of 1.5 mm diameter. A high brightness low power X-Ray tube, coupled with an aspheric multilayer optic (GeniX 3D from Xenocs) was employed, which delivered an ultralow divergent beam (0.5 mrad). Scatterless slits were used to give a clean 0.87 mm diameter X-Ray spot with an estimated flux around 35 mph s^{-1} at the sample position. A transmission configuration was used. The scattered intensity was collected on a two dimensional Schneider 2D image plate detector prototype, located at a distance of 1.9 m from the sample. The experimental data were corrected for the background scattering and the sample transmission.

The bimetallic PdPt powders were also characterized by SAXS and Wide Angle X-Ray Scattering (WAXS). Different to the characterization of the mesophases, the powders were sandwiched between kapton tapes. The sample to detector distance is shorter.

II.2.2 Transmission Electron Microscopy (TEM)

The samples were also characterized using TEM using a JEOL JEM 100CX at an accelerating voltage of 100 kV. Few drops of sample (dispersed in ethanol) were deposited on carbon coated copper grids and dried under N_2 flow. The images were collected using a CCD camera.

II.2.3 Scanning Electron Microscopy (SEM)

Scanning Electron Microscope (SEM) images were acquired using a ZEISS Supra 55VPFEG-SEM at 1 kV with no conductive coating on top of the sample. The sample was prepared by depositing few drops of a suspension of nano P3HT in chloroform on a quartz support and subsequently drying the solution under a N₂ flow.

II.2.4 HAADF-STEM

The samples were characterized by High Angle Annular Dark Field Scanning Transmission Electron Microscopy (HAADF-STEM). The HAADF-STEM images were recorded using a Cs corrected JEOL-ARM-200F electron transmission microscope at 200 kV. The HAADF-STEM images were acquired with a camera length of 8 cm and the collection angles of 70-280 mrad. Energy-Dispersive X-ray Spectroscopy (EDS) measurements for line scan profiles and mapping were obtained with a solid state detector from Oxford with an 80 mm² window. These experiments were performed in collaboration with Daniel Bahena (Cinvestav, Mexico).

II.2.5 XPS (X-Ray Photoelectron Spectroscopy)

XPS measurements were performed on a K-Alpha X-Ray Photoelectron Spectrometer (Thermo Fisher Scientific) under ultrahigh vacuum (base pressure in the low 10⁻⁹ mbar), equipped with a monochromatic Al source using a spot size of 400 μm. The hemispherical analyzer was operated at 0° take off angle in the Constant Analyzer Energy (CAE) mode, with a pass energy of 200 eV and a step of 1 eV for the acquisition of survey scans and a pass energy of 50 eV and a step of 0.1 eV for the acquisition of narrow windows. Charge compensation was done by means of a “dual beam” flood gun. The C 1s signal at 284.8 eV was used as reference for the bonding energy scale.

II.2.6 UV–vis spectrophotometer

UV–vis absorption spectra of the monomer, bulk P3HT and nano P3HT were recorded in chloroform using a Carry 5000 (Agilent) spectrophotometer.

II.2.7 Fluorescence spectroscopy

Luminescence measurements were performed with a SpexFluorolog 1681 spectrofluorimeter equipped with a Hamamatsu R928 photomultiplier cooled down to -20°C . The emission and excitation spectra were recorded at room temperature in the right angle configuration and not corrected by the detection system response. The maximum absorbance of the sample contained in a 1 cm quartz cuvette was below 0.1.

II.2.8 Maldi-TOF (Matrix Assisted Laser Desorption/Ionization Time of Flight)

Maldi-TOF mass spectrometry was used to measure the degree of polymerization. The solution of P3HT in tetrahydrofuran (THF) was mixed with a matrix solution. The matrix-sample solution was then placed on a stainless steel plate. The spectra were obtained in the reflection mode and in the positive ion mode.

II.2.9 Attenuated Total reflectance (ATR-FTIR)

Attenuated Total reflectance (ATR-FTIR) spectroscopy was used for chemical identification of P3HT. ATR-FTIR spectra of 3HT monomer, bulk P3HT, or nano P3HT were recorded using a Bruker Vertex 70 FTIR spectrometer with diamond ATR attachment (PIKEMIRACLE crystal plated diamond/ZnSe) and a mercury-cadmium-telluride (MCT) detector with a liquid nitrogen cooling system. Scanning wavelength were varied from 4000 to 600 cm^{-1} with a 4 cm^{-1} spectral resolution using 100 repetition scans on average for each spectrum.

II.2.10 AFMIR

The morphology of nano P3HT and bulk P3HT, eventually combined with the chemical structure information, was determined by combining the classical atomic force microscope (AFM) with tunable pulsed laser as an Infrared (IR) source (AFMIR). We used a commercial setup, nanoIR (Anasys Instrument corp.) allowing us to cover the range from 3600 cm^{-1} to 1000 cm^{-1} . Drops of ethanolic suspension of P3HT were directly deposited on the upper surface of a ZnSe prism and dried at room temperature. The ZnSe prism is transparent in the mid-infrared and the tip of the AFM remains in contact with the sample. When the sample absorbs the IR laser pulse, it warms via the photothermal effect, resulting in a rapid thermal expansion of the absorbing region of the sample. The

thermal expansion pulse impacts the tip of AFM cantilever and causes it to oscillate. As the amplitude of oscillations is proportional to the absorption, we are able to record infrared absorption spectra at a given point and to make chemical maps by scanning the surface at a given wavelength.⁵⁹

II.2.11 Electrochemical analysis for polymer nanostructures

The electrochemical setup was a three-electrode cell, with a glassy carbon (GC) disk (2 mm diameter) drop-coated by a P3HT film as the working electrode, a Pt wire as counter electrode, and a silver wire pseudo-reference electrode. This latter is calibrated as recommended by IUPAC⁶⁰ probing ferrocenium/ferrocene (Fc^+/Fc) redox potential measured at the end of each experiment. Polymer samples (at a concentration of 1 mg mL⁻¹ in chloroform) were drop-casted onto the GC-electrode and then dried. The GC-electrode was immersed into the electrochemical cell containing acetonitrile with 0.1 M tetrabutylammonium hexafluorophosphate (TBAPF₆). The compounds were electrochemically reduced prior to being oxidized between -2.1 V and +1.4 V at a scan rate of 20 mV/s.

II.3 Application of metal and polymer nanostructures

II.3.1 Metal nanostructures

a. Ethanol oxidation using bimetallic PdPt

➤ Sample preparation

Typically, 0.5 mg of Pd, Pt or PdPt based nanostructures and 0.25 mg PDPB nanofibers were dispersed into 500 μL of ethanol, and sonicated for 15 minutes approximately.

➤ Preparation of working electrode

For the electrochemical experiments, we used glassy carbon as working electrode. Typically, the electrode was polished on 6, 3, and 1 μM carpet sequentially using diamond paste before use. The time for polishing is 5 minutes for 6 and 3 μM carpet, and 10 minutes for 1 μM carpet. The electrode was then sonicated for a short time in ethanol to remove the excess of diamond paste and dried for a few

minutes. 6 μL of sample was then deposited on the surface of the glassy carbon electrode, and let dry for 30 minutes at room temperature.

➤ **Electrochemical tests**

The electrochemical setup was an EG & G 273 A driven by a PC with the M270 software. Potentials were measured against an Hg/HgO reference electrode ($E_{\text{Hg}/\text{HgO}} = 0.098$ vs NHE). The counter electrode was a platinum gauze of large surface area. Pure water from a RiOs 8 unit followed by a Millipore-Q Academic purification set was used throughout. The solutions were deaerated thoroughly for at least 30 min with pure argon and kept under a positive pressure of this gas during the experiments. The supporting electrolyte is 1 M KOH.

b. Glucose oxidation using AuPd, AuPt, and AuPdPt

➤ **Sample preparation**

1.6 mg of sample (weighed with an analytical balance) was added to 800 μL of isopropanol. The solution was then sonicated for 1 hour.

➤ **Preparation of working electrode**

A disk of glassy carbon (3 mm diameter, 0.071 cm^2 geometric surface area) was used as a support for the nanoparticles.

- First the ink was prepared with 1.6 mg of $\text{Pt}_{90}\text{Au}_{10}$ and added 800 μL of Isopropanol. The mixture was homogenized with an ultrasonic bath for 1 h.
- 3 μL of this ink was dropped on the clean glassy carbon disk surface. The ink was dried with a nitrogen flow for few minutes. The electrode obtained can be used for electrochemical investigation

➤ **Electrochemical test for glucose oxidation**

The supporting electrolyte was 0.1 M NaOH. The glucose oxidation was performed in 0.1M NaOH and 10mM of glucose.

c. H_2 evolution using PtNi

The sample and working electrode were prepared in the same way as for PdPt.

➤ **Electrochemical test for H₂ evolution**

The electrochemical setup was an EG & G 273 A driven by a PC with the M270 software. Potentials were measured against saturated calomel reference electrode ($E_{\text{Hg}_2\text{Cl}_2/\text{Hg}, \text{Cl}^-} = +0.2444 \text{ V vs NHE}$). The counter electrode was a platinum gauze of large surface area. Pure water from a RiOs 8 unit followed by a Millipore-Q Academic purification set was used throughout. The solutions were deaerated thoroughly for at least 30 min with pure argon and kept under a positive pressure of this gas during the experiments. The supporting electrolyte is 0.05 M H₂SO₄.

II.3.2 Application of conjugated polymer nano P3HT for photodegradation of pollutants

Phenol (C₆H₅OH) was chosen as model pollutant: it is a real pollutant, stable under irradiation (no photolysis), and its intermediate degradation products are well known. The photocatalytic activity of P3HT was evaluated for decomposition of phenol in a quartz cell reactor with a 10 mm optical path containing 3.5 mL of $3.7 \times 10^{-3} \text{ mol L}^{-1}$ of phenol in the presence of 1 g L^{-1} of P3HT. Other photocatalytic tests were also conducted with Rhodamine B (as another model pollutant) at a concentration of $4 \times 10^{-5} \text{ M}$ in the same conditions.

Before any photocatalytic tests, dark adsorption tests of bulk and nano P3HT were carried out, by putting the polymer samples into contact with the model pollutants in the absence of irradiation: The suspension containing P3HT in phenol or RB solution were stirred for 3 h to ensure the homogeneity of the suspension. After 3 h contact, no adsorption of phenol and RB on the polymer nanostructures or on bulk P3HT could be detected.

The samples were irradiated under stirring with an Oriel 300 W Xenon lamp through an infrared water filter for the experiment under UV-Visible light. For the experiments under visible light an ultraviolet cut off filter (longpass filter GG400, $\lambda \geq 400 \text{ nm}$) was put in front of infrared water filter.

For photocatalytic test of P3HT on a solid support, 3 mg of P3HT was dissolved in chloroform and gently deposited on a quartz glass, then dried at room temperature. A

P3HT-coated quartz glass was inserted into a 1 cm cell containing 3 mL of an aqueous solution with $3.7 \times 10^{-3} \text{ mol L}^{-1}$ of phenol or $4 \times 10^{-5} \text{ M}$ of RB.

400 μL of the solution was taken at different time intervals from the reactor and centrifuged before further analysis (centrifugation process is not necessary in the case of experiment using P3HT-coated quartz glass). HPLC (high performance liquid chromatography) was used to determine phenol concentration and to study its degradation while the RB concentration was determined by spectrophotometric method (at 550 nm). The Total Organic Carbon (TOC) was measured with a Shimadzu TOC-LCSH by IR after complete oxidation by catalytic combustion at 680°C on exclusive platinum catalyst, the inorganic carbon being removed by a previous acidification and air purging.

CHAPTER III

**Synthesis of Porous Metal
Nanostructures in the
Confined Water Phase of
Hexagonal Mesophases for
Application in Fuel Cells**

CHAPTER III

Synthesis of Porous Metal Nanostructures in the Confined Water Phase of Hexagonal Mesophases for Application in Fuel Cells

In this chapter, the synthesis in the confined aqueous phase of hexagonal mesophases of porous metallic nanostructures such as PdPt nanoballs, AuPd and AuPt core-shell nanoparticles, trimetallic AuPdPt and bimetallic PtNi nanostructures are presented. These metal nanostructures were used as electrocatalysts towards electrochemical reactions which are usually used in fuel cells..

Porous PdPt nanoballs were used for ethanol oxidation reaction. The optimization of Pd/Pt ratio and the influence of the pore size of nanoballs on their electrocatalytic performance was investigated. Preliminary results of the electrocatalytic activity of AuPd, AuPt, and AuPdPt nanostructures for ethanol oxidation and glucose oxidation reaction will be presented. Preliminary results on bimetallic PtNi porous nanostructures for H₂ evolution reaction are also presented.

This chapter is divided into 4 parts: 1) The introduction to fuel cells, basic working principles, and the importance of porous materials in electrocatalytic reactions; 2) Synthesis of porous PdPt nanoballs and their application in ethanol oxidation reaction, 3) Synthesis of core-shell AuPd/ AuPt porous nanostructures and trimetallic AuPdPt nanoballs and their application in ethanol oxidation reaction, and 4) Synthesis of PtNi nanostructures by radiolysis or electron beams and their application in H₂ evolution reaction.

III.1 Fuel cells

Fuel cells are static energy conversion devices that convert chemical reactions into electrical energy and produce water as the byproduct (in the case of hydrogen fuel cells).^{61,62} By contrast, conventional heat engines produce electricity from chemical energy with the use of intermediate mechanical energy conversion, which results in reduced efficiency compared to fuel cells. Compared to the other energy generation technologies, fuel cells offer several advantages like high energy conversion efficiency, zero emission, modularity, and scalability.⁶³⁻⁷⁶

III.1.1 Basic working principle

Figure 3.1 presents a simple fuel cell diagram with H_2 as the fuel. Principally, fuel cell consists of two main parts: the anodic part, where the oxidation of the fuel takes place, and the cathodic part where the reduction of oxygen takes place. The fuel cell consists of an electrolyte layer in contact with two electrodes on either side. The hydrogen fuel is fed continuously to anode electrode and the oxidant (oxygen) from air is fed continuously to the cathode electrode. At the anode, the hydrogen fuel is decomposed into positive ions and electrons. The intermediate electrolyte membrane permits only the positive ions to flow from the anode to the cathode side and acts as an insulator for electrons. These electrons have tendency to recombine on the other side of the membrane for the system to become stable, for which the free electrons move to the cathode side through an external electrical circuit. The recombination of the positive ions, electrons, and oxidant takes place at the cathode to form pure water. In the case of hydrogen fuel cells, the chemical reactions involved at the anode, at the cathode and the overall reactions are given as below:

Anode reaction using H_2 as fuel:



Cathode reaction:



Overall reaction:

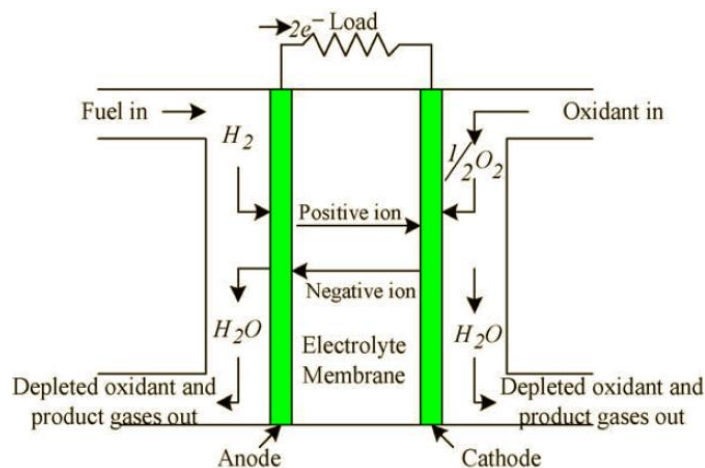


Figure 3.1 Fuel cell operation scheme.⁷⁷

Hydrogen is considered as a clean energy vector of the future able to solve the global energy and environmental crises. Development of efficient and cheap materials for green H₂ production is a main challenge towards a sustainable hydrogen economy. However, nowadays hydrogen is produced at 95% from fossil resources, which are limited and CO₂-emitting technologies.⁷⁸ Scientists are trying to develop economical and convenient ways to produce H₂ from the most abundant natural resources on earth namely water and sun. The main drawback using H₂ is its flammability, which makes its storage and transport difficult. Development of porous materials very efficient to store hydrogen is a challenge.

III.1.2 Direct alcohol fuel cells

In the last few decades, there have been an increasing interest in the development of Direct Alcohol Fuel Cells (DAFCs), particularly for application to the electric vehicle.⁷⁹ DAFCs offer several advantages compared to hydrogen fuel cells: high solubility in aqueous electrolytes, liquid fuel available at low cost, easily handled, transport, and stored, high theoretical density of energy compared to that of gasoline.⁸⁰ Among several alcohols used in DAFCs, ethanol appears as the most suitable fuel for commercialization. Compared to methanol, which is volatile, highly toxic, and flammable, ethanol is less toxic and easier to be handled, and has a higher energy density. In addition, ethanol can be produced in large quantity from biomass and is considered as a renewable energy.

There are two types of direct ethanol fuel cells: proton exchange membrane fuel cells (PEM-DEFCs) and anion exchange membrane fuel cells (AEM-DEFCs). The primary challenge in PEM-DEFCs is the sluggish kinetic of the ethanol oxidation reaction (EOR). Using acidic media and Pt catalysts has not been able to overcome this problem. Different observations have been made in alkaline media. It has been shown that when the acid electrolyte is changed to alkaline media, the fuel cell efficiency increases.⁸¹⁻⁸³ The performance of fuel cells mainly relies on electrocatalytic reactions in the anodic part (fuel oxidation) and in the cathodic part (oxygen reduction).

Catalysts for anodic reactions

Alkaline media DEFCs also offer the other advantage over acid media that they can use non-Pt catalysts. Pt is known as the most active catalysts for most of the reactions involved in fuel cells, especially in acidic media. However, Pt is rare, expensive and can be easily poisoned by the adsorbed of CO on its surface, which blocks electro-active sides of the catalysts.⁸⁴⁻⁸⁶ A convenient way to modify the electrocatalytic properties of Pt and to decrease the poisoning of its surface by adsorbed CO, is to alloy Pt with a second metal or even a third metal.⁸⁰ The use of non-Pt catalysts can reduce the cost of the catalysts as well as their efficiency and durability.^{87,88} Pd is known as the best electrocatalyst for ethanol oxidation in alkaline media. However, Pd is not really good in C-C bond breaking and most of the final products is acetate. Pt is a good electrocatalyst for C-C bond breaking, though it is expensive and can be easily poisoned by CO. Alloying Pd and Pt is expected to improve the activity and stability of the electrocatalysts towards ethanol oxidation.^{89,90}

A lot of research has been conducted to understand the mechanism of ethanol oxidation reactions on Pd and Pt catalysts since 1950s.⁹¹ Today, the commonly accepted mechanism of ethanol oxidation is a dual-pathway mechanism on Pt or Pd based catalysts in either acidic or alkaline media as shown in **Figure 3.2**.⁹²⁻⁹⁷

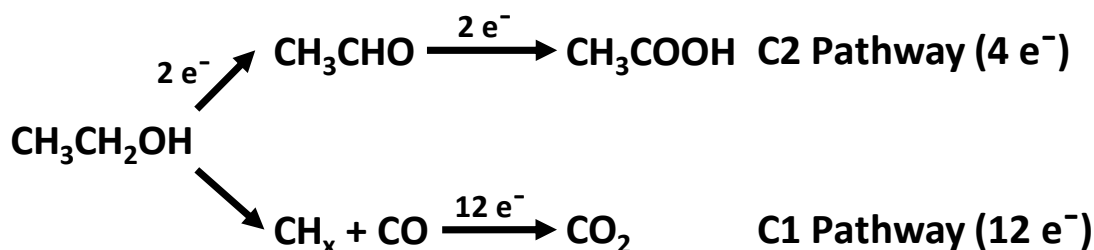
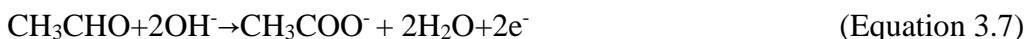
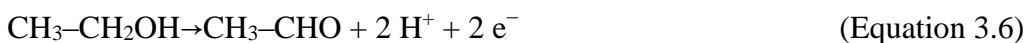


Figure 3.2 Schematic representation of the parallel pathways for ethanol oxidation on Pd and Pt electrodes.⁹⁸

The C1 pathway is the complete oxidation of ethanol to CO₂ or carbonates via CO_{ads} (adsorbed CO) intermediate by delivering 12 electrons and the C2 pathway is the partial oxidation of ethanol to acetate by delivering four electrons or to acetaldehyde by delivering two electrons without the breaking of the C–C bond as shown in the following equations (Equations 3.4 – 3.7):⁹⁸

C1 pathway:**C2 pathway:****Catalysts for cathodic reactions**

The kinetic of oxidation reaction of a fuel in the anodic part is much faster compared to the oxygen reduction reaction (ORR) in the cathodic part. The sluggish reaction kinetics of ORR even on the best Pt-based catalyst requires much higher Pt loading ($\sim 0.4 \text{ mg cm}^{-2}$) to achieve a desirable fuel cell performance.⁹⁹ Alloying Pt with non-noble metals such as Ni, Co, and Fe, is expected to improve its activity for oxygen reduction reaction.

During my PhD I focused only on the oxidation reactions, *i.e.* on the reactions involved in anodic part.

III.1.3 Nanomaterials for electrocatalysis in DAFCs

In DAFCs, the high cost and problem of durability (caused mainly by the use of electrocatalysts based on Pt) are the main limiting factors for large scale applications. Two approaches can be used to solve this problem: replacing/alloying Pt with other inexpensive (or less expensive) metals and increasing the active surface of electrocatalysts. Increasing the surface area to volume ratio can be achieved by engineering advanced electrodes based on nanoporous or mesoporous metallic particles.

Porous metallic electrocatalysts

Porous metallic nanomaterials have particular interest for applications in electrocatalysis because they exhibit exceptional properties including ultrahigh surface areas, large pore volumes, and nanoscale effects in their channels and their pore walls.¹⁰⁰ A high surface area provided by porous metallic electrocatalysts increases the proportion

of atoms exposed on the surface and subsequently should provide a large number of reaction or interaction sites for surface or interface related processes.¹⁰⁰ **Figure 3.3** illustrates an example of porous electrode and the scheme of coupled physicochemical steps that constitute an electrocatalytic process.

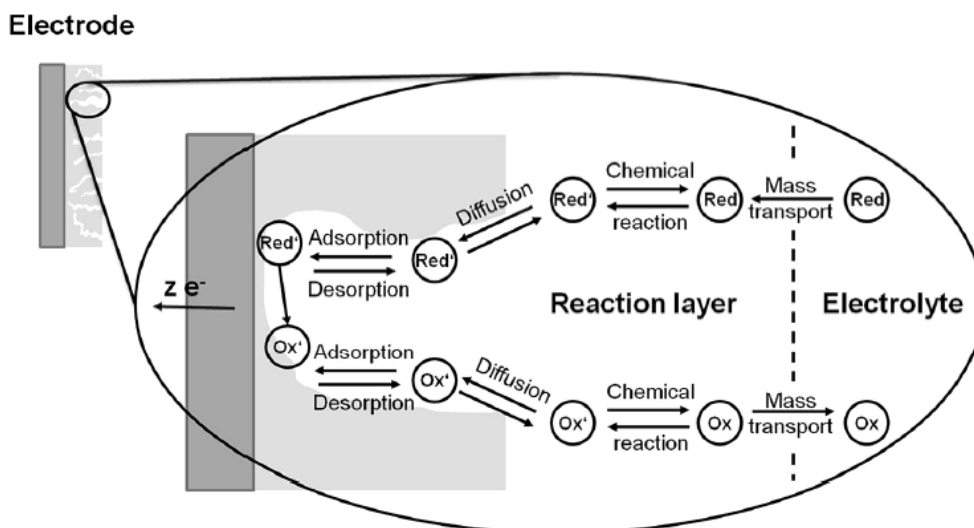


Figure 3.3 Schematic representation of the individual physicochemical steps that constitute an electrocatalytic process. The process is illustrated for the example of a porous electrode applied to an oxidation reaction.¹⁰¹

The chemical transformation of reactants occurs in the reaction layer near the surface of the electrode. The catalytic reaction itself proceeds at the interface between (accessible) the electrode surface and electrolyte. It consists of adsorption, reaction, and desorption. However, these catalytic steps are often preceded by diffusive transport of reactants to the electrode interface, chemical reactions occurring in the electrolyte, and mass transport from the bulk of the electrolyte to the reaction layer. Moreover, the products of the electrocatalytic surface reaction are also the subject of similar reaction and transport steps. The chemical and geometrical configuration of the catalytic electrode provides control over all of these individual steps.¹⁰¹ The porosity of electrocatalytic materials controls not only the active surface area, but also the transport of reactants and products. Small pores provide a high surface area, however, they can also decrease the rate of mass transport. Nevertheless, in the case of ethanol oxidation process, no chemical reaction upon free diffusing species has been experimentally observed in reaction layer.

In the following paragraph, we discuss the interest of using porous metal nanostructures for oxidation of alcohol (anodic reaction) and for reduction of oxygen (cathodic reaction).

a. Anodic catalysis

Yamauchi's group reported that nanoporous Pd@Pt (Pd is the core and Pt is the shell) having an average particle size of 80 nm and pore-to-pore distance of 16 nm shows enhanced activity for methanol oxidation in term of onset potential (about 0.1 V more negative), peak current (> twofold), and stability, compared to Pt black.¹⁰²

Several monometallic (Pd¹⁶ and Pt⁸⁸) and bimetallic (Pd-Pt¹⁰³ and Au@Pd¹⁰⁴) porous nanoballs (synthesized in the soft templates formed by hexagonal mesophases) exhibit a high activity for ethanol oxidation. Porous Au@Pt core-shell nanostructures (synthesized in hexagonal mesophases by radiolysis) also show excellent performances for glucose oxidation.⁸⁸

b. Cathodic catalysis

Pt₃Ni(111) is one of the most active surface for oxygen reduction reaction (ORR). Alloying of Pt and Ni can shift the d-band center of the surface Pt atoms that results in weakened interactions between Pt and intermediate oxide species, freeing more active sites for O₂ adsorption.¹⁰⁵ Erlebacher and coworkers proposed that the chemical composition and structure of materials can further improve their activity towards ORR. It has been also shown that ORR can be highly improved using porous Pt.¹⁰⁶

III.2 Bimetallic PdPt Nanoballs Synthesized in Hexagonal Mesophases for Electrooxidation of Ethanol

The search for renewable energy resources to replace the utilization of fossil fuels has become the major focus in research and industrial sector in the past decades. Direct alcohol fuel cells (DAFCs), because of their high efficiency, cleanness, easy transport (compared to hydrogen fuel cell), are predicted to be a good solution for green vehicles.

Platinum is well known to be the best catalyst for most of the reactions involved in fuel cells such as HOR (Hydrogen oxidation reaction), ORR (Oxygen reduction reaction), MOR (Methanol oxidation reaction), and FOR (Formic acid oxidation

reaction).¹⁰⁷ However, the scarcity of Pt, its high cost, and the problem of stability and durability (because the poisoning effect from the strongly adsorbed CO on its surface produced during the reactions) limit its application in fuel cells. Several techniques have been focused to decrease the cost and to improve the activity as well as the stability of the catalysts.

Alloying Pt with other inexpensive metals can decrease the catalyst cost and improve its activity and durability due to the synergetic effects from the two (or more) metals.^{89,108–113} Palladium is known to be the best material for ethanol oxidation in alkaline media. Moreover, Pd is about 50 times more abundant on earth compared to Pt. Alloying Pt and Pd is not only expected to reduce the cost, but also to improve the activity and stability of the electrocatalyst. Previous findings have indeed shown that bimetallic PdPt nanostructures exhibit higher activity and stability toward ethanol and methanol oxidation compared to their monometallic counterparts.^{112,114}

The catalytic electrocatalytic activities of a material have been reported to highly depend on its morphology, surface area, porosity, and size distribution. Porous metal nanostructures with large surface areas are attracting a lot of interest because of their potential applications in different fields such as catalysis, electrocatalysis and fuel cells, hydrogen storage, and chemical sensors. According to IUPAC, porous materials are divided into 3 classes: macroporous (pore size > 50 nm), mesoporous (2 nm < pore size < 50 nm), and microporous (pore size < 2 nm) materials.¹¹⁵

Metal porous nanostructures can exhibit better activity compared to spherical nanoparticles in electrocatalytic reactions. Porous Pd nanoflowers synthesized by a modified polyol method showed higher activity (about 60% more active than Pd nanoparticles (based on per mass unit of Pd)) and stability for methanol oxidation in alkaline media. In particular,¹¹⁶ Margareta and co-workers showed that nanoporous solid of Pd and Pt afford higher electro-oxidation efficiency and increase the catalytic stability relative to the corresponding planar metallic surface for methanol and ethanol oxidation.¹¹⁷ Porous bimetallic PdPt alloy nanosponges on the other hand have been shown to exhibit a much enhanced activity and stability towards the ethanol oxidation reaction in alkaline solution by providing large surface areas.¹¹² Due to the significant enhancement in terms of activity and stability that porous metal nanostructures can

exhibit for several electrocatalytic reactions involved in fuel cells, a lot of studies have been devoted to improve the synthesis of these porous materials.¹⁰⁰

The synthesis of porous metal nanostructures with controllable pore size generally requires the use of templates. Very often hard templates are used. However, a major drawback of using hard templates is the complicated process to extract the porous materials (synthesized within): To get rid from the template, a calcination process and a use of harsh chemical reagent (such as hydrofluoric acid) are often required.

Hexagonal mesophases (formed by elongated micelles arranged in hexagonal lattice structure) are made of a quaternary system (surfactant, co-surfactant, oil, and brine)(as explained in Chapter I). Those elongated micelles are tubes containing cyclohexane or toluene and which diameter can be controlled by tuning the volume ratio between the oil phase and the water phase.⁴⁸ Synthesis of nanomaterials can take place in the water phase, the oil phase, and even in both phases simultaneously. Several metal nanostructures (such as Pd, Pt, and Au) have been synthesized in the confined water phase and some conjugated polymer nanostructures (such as PEDOT, PDPB, and P3HT) have been prepared inside the oil tube of hexagonal mesophases.^{15,44,45,51,118-121}

These mesophases are very versatile templates for the synthesis of nanomaterials. A. Lehoux *et al.* have reported synthesis (in hexagonal mesophases) and characterization of porous PdPt bimetallic nanoballs (formed by 3D-connected nanowires forming hexagonal cells) of controlled porosity and composition.⁴⁸

In this work, these porous bimetallic nanoballs with controlled of porosity and composition were used for ethanol oxidation in basic media. The electro-active surface area as well as the current are greatly enhanced with increasing the pore size of PdPt nanoballs.

III.2.1 Materials characterizations

a. Characterization of hexagonal mesophases by SAXS

The hexagonal mesophases that we used as templates to synthesize metal nanostructures are made of CTAB as surfactant, cyclohexane as oil, n-pentanol as co-surfactant, and salty water, the salt being a metallic salt (or a mixture of metallic salts) and NaCl. According to the previous results from our group, in order to control the diameter of the oil tubes, one can vary the volume of oil and the salt concentration, while

keeping the volume of water constant.⁴⁸ The schematic representation of the cross section of swollen hexagonal mesophases is shown in **chapter I (Figure 1.19)**.

The metallic salts of Pd and Pt are contained in the aqueous phase. When the volume of oil (here cyclohexane) increases, the salt concentration in the aqueous phases is increased simultaneously. The concentration of the metallic salt is always kept constant at 0.1 M. The ionic force is controlled by the addition of NaCl, whose concentration varies from 0 M – 0.5 M. The diameter of the oil-swollen tube (D) increases as the volume of cyclohexane increases, while the distance between the tubes (e), which is mainly controlled by the water over surfactant ratio (kept constant here) is almost constant.

Small Angle X-Ray Scattering (SAXS) was used to characterize the formation of hexagonal mesophases and to measure the diameter of the oil tube in hexagonal mesophases. According to SAXS, all samples have hexagonal geometry based on the peak positions, which are in the ratios of 1: $\sqrt{3}$: 2 (characteristic feature for hexagonal mesophases) (**Table 3.1**). The position of the first peak (q_0) is directly correlated to the lattice parameter (d_c) as defined by the equation $d_c = \frac{2}{\sqrt{3}} \frac{2\pi}{q_0}$. One can further relate the lattice parameter to the tube diameter (D) , where $D = 2d_c \sqrt{\left(\frac{\sqrt{3}}{2\pi}(1 - \phi_p)\right)}$. The position of the first peak is shifted towards lower wave vector when oil/water (O/W) ratio increased which indicated the swelling of the tube (**Figure 3.4 and Table 3.1**).

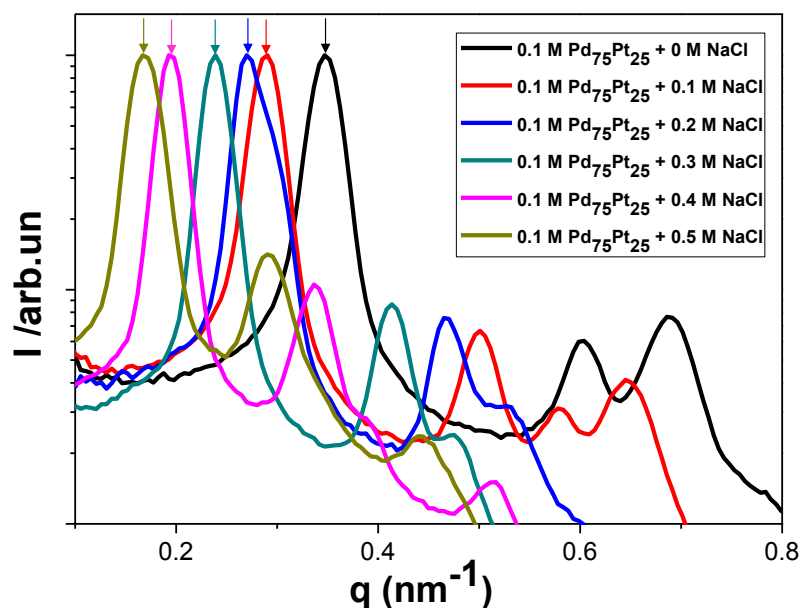


Figure 3.4 Scattered Intensity as a function of wave vector q for doped mesophases before irradiation comprising 0.1 M of metallic salts (Pd/Pt=75/25) and different concentrations of NaCl, as indicated, and oil contents with different concentrations. The arrows mark the first Bragg peak for the different samples synthesized in hexagonal mesophases with different O/W ratio (1.5, 2, 2.5, 3.25, 3.75, and 4.5).

Table 3.1 Numerical values of q_0 , q_1 , q_2 and ratio q_1/q_0 and q_2/q_0 for samples before irradiation.

Samples	O/W	q_0 (nm ⁻¹)	q_1 (nm ⁻¹)	q_2 (nm ⁻¹)	q_1/q_0	q_2/q_0
0.1 M PdPt + 0 M NaCl	1.5	0.348	0.603	0.69	1.732	1.982
0.1 M PdPt + 0.1 M NaCl	2.0	0.289	0.501	0.580	1.733	2.002
0.1 M PdPt + 0.2 M NaCl	2.5	0.269	0.468	0.529	1.739	1.966
0.1 M PdPt + 0.3 M NaCl	3.25	0.238	0.412	0.476	1.730	1.999
0.1 M PdPt + 0.4 M NaCl	3.75	0.194	0.340	0.390	1.74	2.007
0.1 M PdPt + 0.5 M NaCl	4.5	0.168	0.290	0.339	1.726	2.017

Based on equations 1.12 to 1.14, the value of d_c , D , and e have been calculated and displayed in **Table 3.2**. We find that the tube diameter varies between 18 to 40 nm, while the thickness of water channel is roughly constant (around 2.6 to 3 nm).

Table 3.2 The characteristic sizes of hexagonal mesophases (d_c , D , and e), which were obtained from SAXS spectra before irradiation.

CTAB	Aqueous phase			cyclohexane (mL)	O/W	d_c (nm)	D (nm)	e (nm)	
	water	Total Pd-Pt salts (M)	[NaCl] (M)						[Total salt] (M)
1.03 g	2 mL	0.1 M	0	0.1	2.98	1.5	20.89	18.03	2.6
			0.1	0.2	4	2	25.09	22.11	2.98
			0.2	0.3	5	2.5	26.95	24.13	2.82
			0.3	0.4	6.5	3.25	30.43	27.75	2.68
			0.4	0.5	7.5	3.75	37.31	34.36	2.95
			0.5	0.6	9	4.5	43.15	40.10	3.05

These hexagonal mesophases were used as nanoreactors for synthesis of bimetallic nanoballs. Hexagonal mesophases containing metallic salts were exposed to gamma irradiation with a dose rate about 3.8 kGy/h for 24 hours, a total dose of 91.2 kGy was applied to insure complete reduction of the metal precursors. A low dose rate is needed for the formation of nanoballs.⁴⁸ n-pentanol contributes to the reduction of metal ions on the radiolysis-induced seeds. After reduction, the color of the hexagonal mesophases turns from transparent to black, indicating the reduction of Pd(II) and Pt(II) to Pd(0) and Pt(0). XPS characterizations confirmed the complete reduction of Pt and Pd.⁴⁸

Stability of nanoreactor hexagonal mesophases

For the application of hexagonal mesophases as nanoreactors, the stability property is an important parameter. Previous studies have shown that these mesophases are very stable with irradiation.^{44,121} Here again the stability of these mesophases following irradiation was checked by comparing the SAXS profiles of the samples, before and after irradiation (**Figure 3.5**). The ratio of the first 3 peaks of the doped mesophases with Pt and Pd before and after irradiation is in the ratio 1: $\sqrt{3}$: 2, a characteristic feature for hexagonal mesophases. Only a small shift of the peak positions was observed, suggesting a weak contraction of the mesophase upon irradiation.

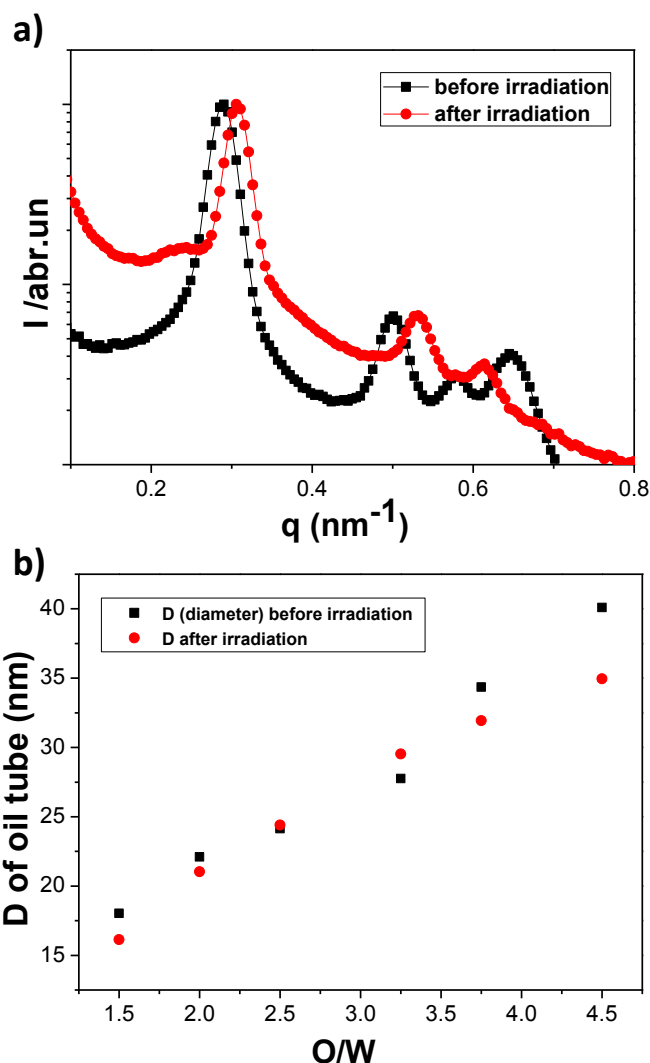


Figure 3.5 a) SAXS spectra of hexagonal mesophases containing metallic salts of Palladium and Platinum with the ratio of 3/1 ($\text{Pd}_{75}\text{Pt}_{25}$) before and after irradiation for the sample with $O/W = 1.5$; b) Diameter of the oil tubes, D , as the function of O/W ratio before and after irradiation.

Table 3.3 gives the numerical values of the first 3 peak positions of SAXS spectra for hexagonal mesophases with different O/W ratio after irradiation. The positions of the first peaks are shifted about 10% towards higher wave vector, which suggesting a weak contraction of mesophases upon irradiation. However, the peak positions are still in the expected for a hexagonal mesophase ratio of 1: $\sqrt{3}$: 2. This result suggests that hexagonal mesophases with different O/W ratios (from 1.5 to 4.5) are stable with irradiation.

Table 3.3 q_0 , q_1 , q_2 values and the ratios q_1/q_0 and q_2/q_0 after irradiation

Samples	q_0 (nm ⁻¹)	q_1 (nm ⁻¹)	q_2 (nm ⁻¹)	q_1/q_0	q_2/q_0
0.1 M PdPt + 0 M NaCl	0.388	0.670	0.773	1.726	1.992
0.1 M PdPt + 0.1 M NaCl	0.307	0.529	0.615	1.723	2.003
0.1 M PdPt + 0.2 M NaCl	0.258	0.444	0.515	1.723	1.999
0.1 M PdPt + 0.3 M NaCl	0.219	0.375	0.439	1.712	2.004
0.1 M PdPt + 0.4 M NaCl	0.207	0.355	0.440	1.715	2.125
0.1 M PdPt + 0.5 M NaCl	0.193	0.334	0.386	1.730	2.000

The comparison of the values of the diameter of the oil tube (D) and the thickness of the water channel of hexagonal mesophases before and after irradiation are given in **Table 3.4**. The lattice parameter before and after irradiation are comparable within 12%. The diameters of water channel are comparable.

Table 3.4 d_c , D, and e values of hexagonal mesophases before and after irradiation determined by SAXS.

Samples	d_c (nm)		D (nm)		e (nm)	
	Before	After	Before	After	Before	After
0.1 M PdPt + 0 M NaCl	20.89	18.70	18.03	16.14	2.6	2.56
0.1 M PdPt + 0.1 M NaCl	25.09	23.60	22.11	21.04	2.98	2.20
0.1 M PdPt + 0.2 M NaCl	26.95	28.15	24.13	24.41	2.82	3.74
0.1 M PdPt + 0.3 M NaCl	30.43	33.10	27.75	29.88	2.68	3.22
0.1 M PdPt + 0.4 M NaCl	37.31	35.00	34.36	31.94	2.95	3.06
0.1 M PdPt + 0.5 M NaCl	43.15	38.00	40.10	35.00	3.05	2.6

As mentioned before, the other advantage of using hexagonal mesophases as nanoreactors is the easiness to collect the nanomaterials after their synthesis. Pd and Pt bimetallic nanoballs can be easily extracted by adding 2-propanol, followed by centrifugation and washing several times with warm 2-propanol at the temperature around 50° C (to remove the excess of CTAB, which might inhibit the electrocatalytic activity of

the nanostructures). It has to be noticed that a relatively high amount of nanomaterials (few hundreds of mg to few grams) can be produced as the mesophases are doped with high concentration of metal precursors (0.1 M) and large volumes (larger than 100 mL) of mesophases can be irradiated.

b. Transmission Electron Microscopy (TEM)

Figures 3.6 and 3.7 show TEM images of PdPt nanoballs synthesized with different O/W ratios. TEM observations show that the nanomaterials synthesized in the confined aqueous phase of hexagonal mesophases are porous nanoballs of 100-200 nm diameters and formed by 3D-connected nanowires.

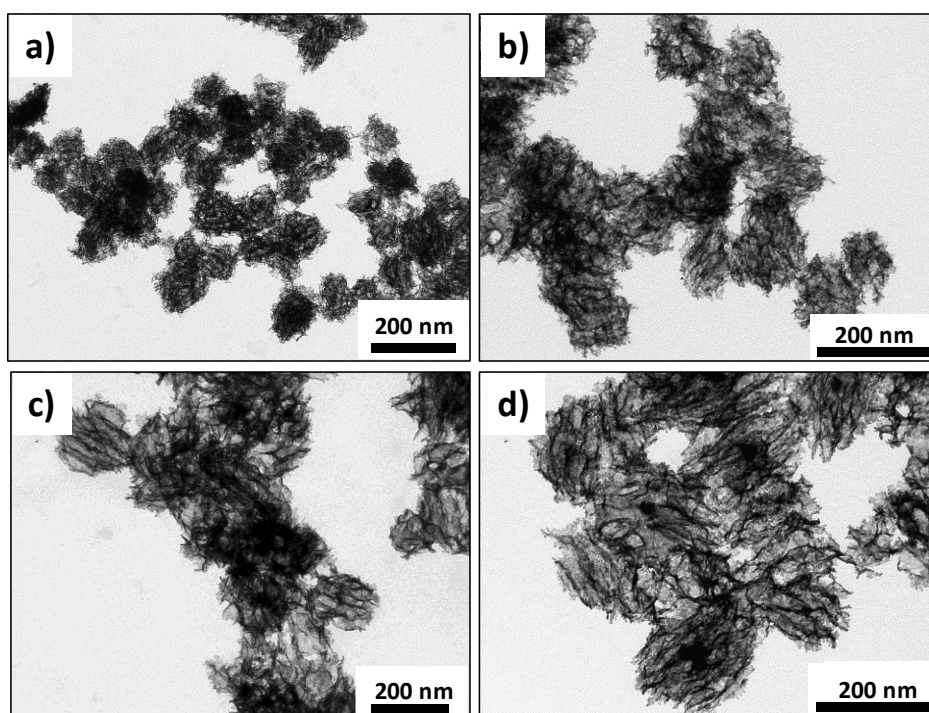


Figure 3.6 TEM images of $Pd_{75}Pt_{25}$ nanoballs using different O/W ratios: (a) 1.5; b) 2; c) 3.25; d) 3.75.

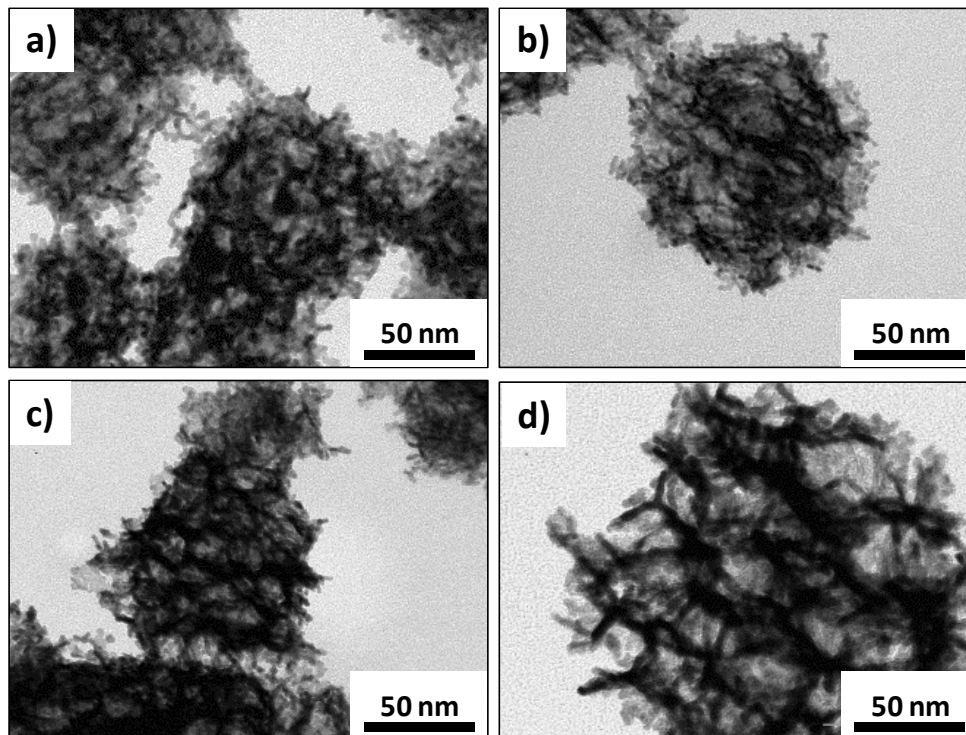


Figure 3.7 TEM images of Pd₇₅Pt₂₅ nanoballs using different NaCl concentrations: (a) 1.5; b) 2; c) 2.5; d) 3.75.

The nanoballs are constituted of 3D-interconnected metal nanowires, which were formed in the confined water phase of the hexagonal mesophases. The nanowires diameter is about 2.5 nm and is comparable to the distance between adjacent tubes. The pore sizes of nanoballs are equal to the diameter of the oil tube and increase with the O/W ratio (**Figure 3.8**). The pore size of nanoballs increases from 12 nm for O/W=1.5 to about 40 nm for O/W=4.5, as measured from the TEM images using ImageJ software. **Figure 3.8** shows that the pore size increases linearly with the O/W ratio.

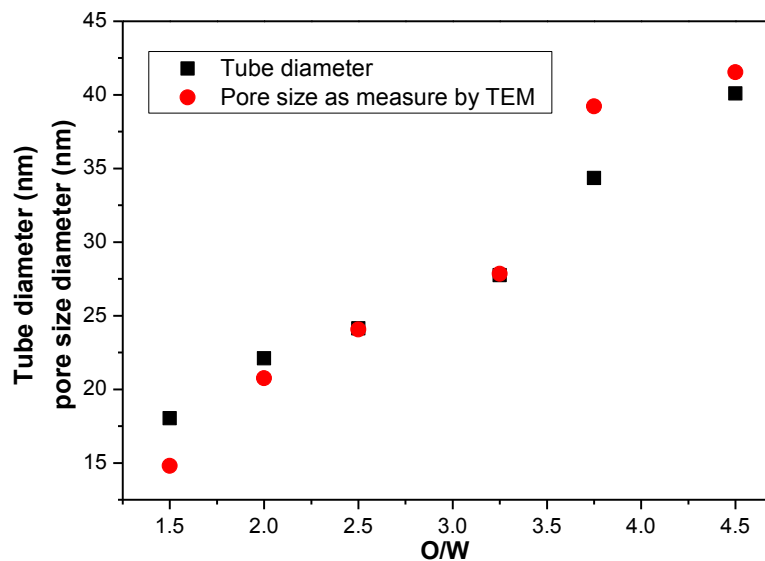


Figure 3.8 Tube diameter of soft template hexagonal mesophases and tube diameter of PdPt porous nanoballs as the function of O/W ratio.

c. Pore size measurement by SAXS-WAXS

The pore size measurements from TEM are based on a limited number of images. Therefore, it is necessary to perform other experiments. X-ray scattering spectra of the dry powder of nanoballs after extraction from hexagonal mesophases can be used to evaluate the pore size.

A typical spectrum, scattered intensity I as a function of scattering vector q , is displayed in **Figure. 3.9**. A weak peak is observed at q^* , which is characteristic of the pore size of nanoballs. The pore size can be evaluated using the equation below:

$$pore\ size = \frac{2\pi}{q^*} \quad (\text{Equation 3.8})$$

In the case of the sample with O/W ratio = 1.5, the position of q^* is at 0.39 nm^{-1} , and the calculated pore size around 16 nm, which corresponds to the pore size measured from TEM images (around 14.6 nm) for the same sample.

For q larger than q^* , one probes length scales smaller than the pore size. The power law decrease of I with q reflects the complex structure of the nanowire making the porous nanoballs. The cross-over from this regime to the regime of stronger decrease of I with q occurs at a wave vector of $q^{**} \approx 1.54\text{ nm}^{-1}$. This value corresponds to a characteristic size, $2\pi/q^{**} \approx 4\text{ nm}$, of the order of the thickness of the metallic wires of

the porous nanoballs, although slightly larger compared to the value measured from TEM images (2.5 nm).

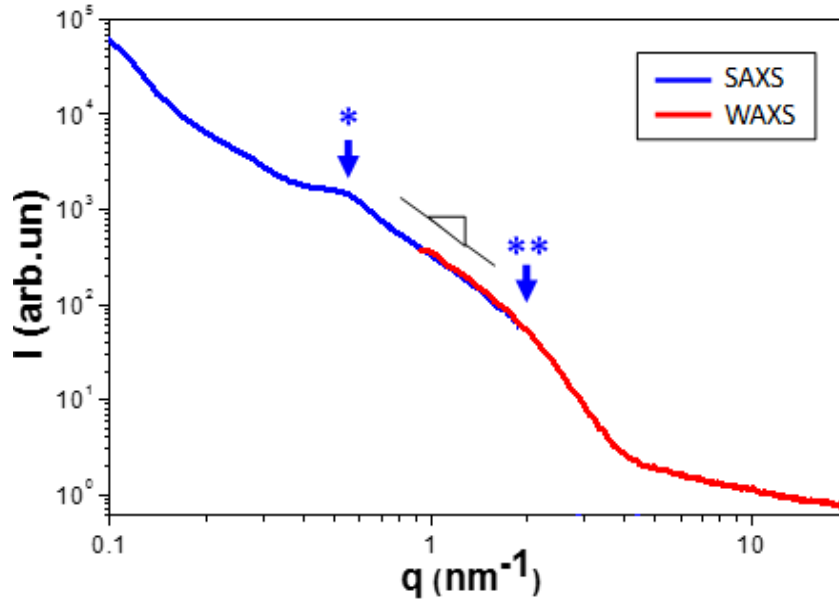


Figure 3.9 Scattering curve combining SAXS and WAXS for powder of nanoballs prepared in hexagonal mesophases with $O/W = 1.5$.

Figure 3.10 shows the values of the diameter of the tubes of the mesophases (before and after irradiation) and those of the pore sizes of the nanoballs (as measured by TEM and SAXS-WAXS) as a function of O/W ratio. Comparable values are measured for the pore size measured by X-ray scattering and by TEM. Moreover these values are comparable to the tube diameter of the mesophases, demonstrating the templating effect of the mesophase. Our results clearly show that the pore size of the nanoballs can be finely tuned by controlling the oil tube diameter.

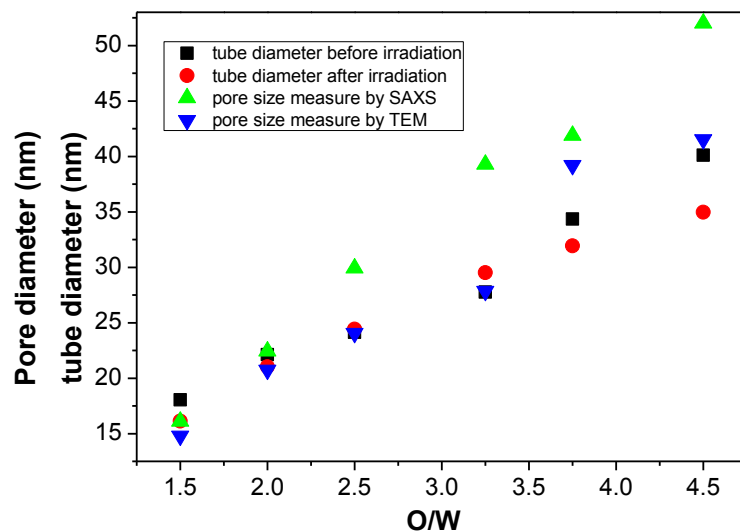


Figure 3.10 Tube diameters of mesophases (before and after irradiation) and pore sizes of nanoballs (as measured by TEM and SAXS-WAXS) as a function of O/W ratio.

d. Pore size measurement by BET

BET was used to determine the pore size of PdPt nanoballs ($\text{Pd}_{75}\text{Pt}_{25}$). These experiments were performed by Fabrice Audonnet (Université de Clermont). **Figure 3.11** shows that the pore size of $\text{Pd}_{75}\text{Pt}_{25}$ nanoballs increases when O/W increases (increase diameter of oil tube). However, a strange result observed for the sample synthesized in mesophases with O/W = 2, indeed the BET analysis of this sample is still needed to be repeated. However, the pore sizes measured by BET are much smaller compared to the TEM and SAXS-WAXS.

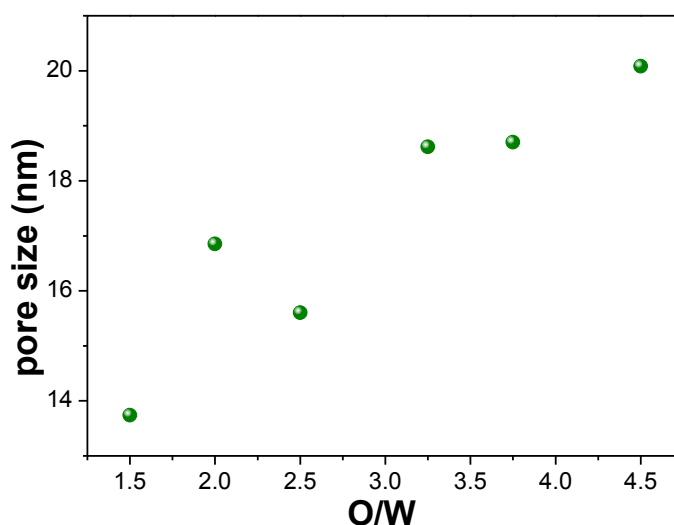


Figure 3.11 Pore sizes of $\text{Pd}_{75}\text{Pt}_{25}$ nanoballs measured by BET as the function of O/W ratio.

e. HAADF-STEM and EDS

In order to elucidate the distribution ratio of Pd and Pt on the surface of nanoballs, analysis using HAADF-STEM (High-Angle Annular Dark Field Scanning Transmission Microscopy) and EDS (Energy Dispersive X-Ray Spectroscopy) were performed on Pd₇₅Pt₂₅ nanoballs with different pore sizes. **Figure 3.12** shows the HAADF-STEM images of Pd₇₅Pt₂₅ nanoballs at the same scale with different pore sizes (synthesized in mesophases with different O/W ratio; 1.5, 3.25, and 4.5). The images in Figure 3.13 suggest that the ratio of Pd to Pt on the surface of nanoballs also changes when pore size increases. Pd is more dominant than Pt on the surface of nanoballs at higher pore size.

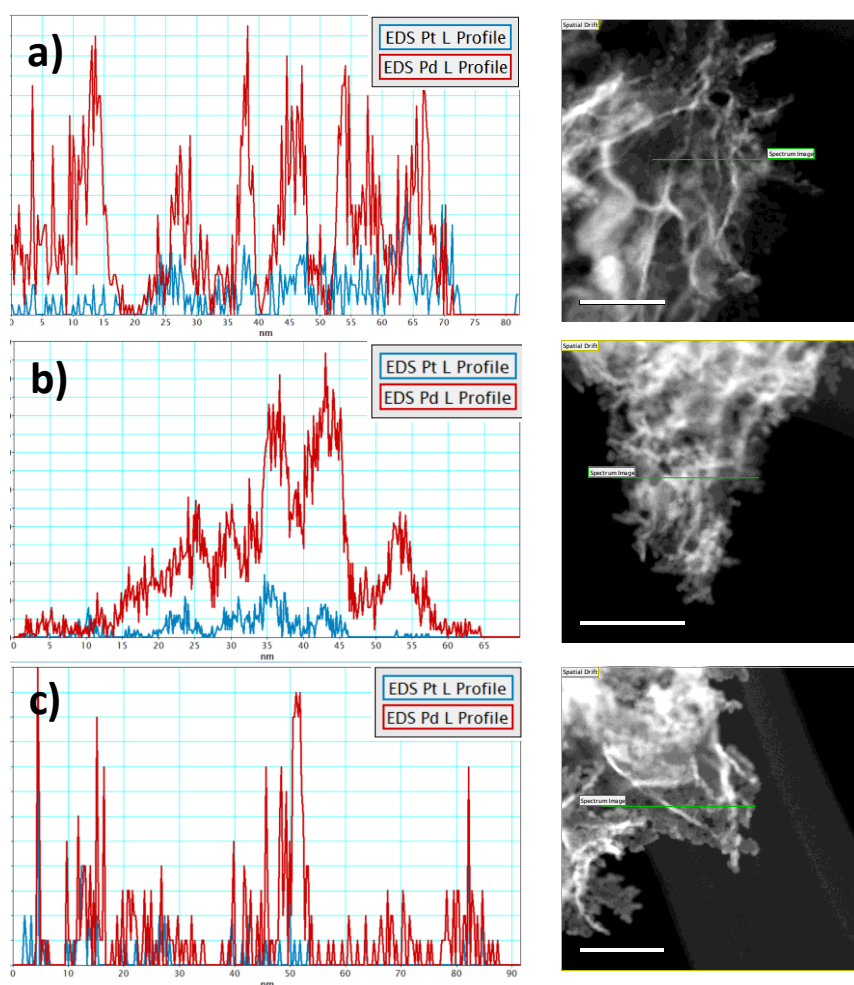


Figure 3.12 EDS profiles of Pd₇₅Pt₂₅ nanoballs of different pore sizes (synthesized in different O/W ratio; a) 1.5, b) 3.25, and c) 4.5) along with their corresponding HAADF-STEM images.

The quantifications of the Pd/Pt percentage on the surface of nanoballs taken from the EDS profile are plotted in graphs in **Figure 3.13**. Graph in **Figure 3.13** shows that the

Pd percentage increases from around 50% to 85% when the O/W ratio of the mesophases increases from 1.5 to 4.5 (which corresponds to the increase the porosity of nanoballs), while the percentage of Pt on the surface decreases from 50% to 15%. However, a strange result was obtained with the sample synthesized in mesophases with O/W = 2 (the one in red circle), and the experiment has to be repeated.

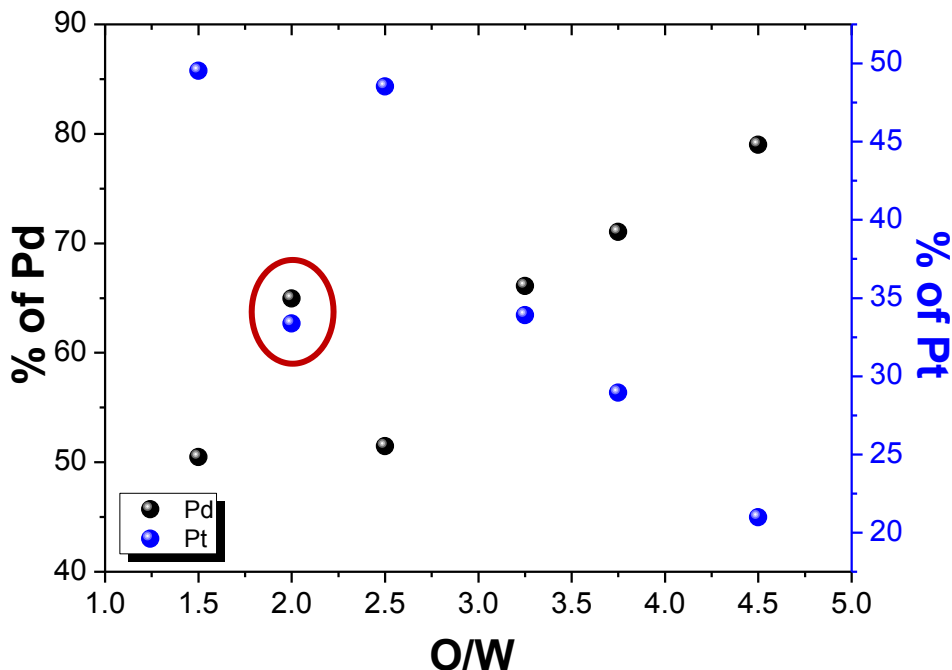
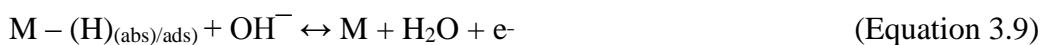


Figure 3.13 The percentage of Pd and Pt metals according to EDS profile on the surface of nanoballs synthesized in mesophases at different O/W ratio (corresponding to different pore size).

III.2.2 Application of PdPt nanoballs for electrooxidation of ethanol

a. Cyclic voltammetry of PdPt nanoballs in alkaline solution

Cyclic voltammetry was performed in alkaline media with 1 M of KOH as supporting electrolyte. The working electrode was a glassy carbon electrode modified with PdPt porous nanoballs, which were embedded in PDPB on its surface. **Figure 3.14** shows cyclic voltammogram of PdPt bimetallic nanoballs. According to the literature, at a potential range smaller than -500 mV vs Hg/HgO reference electrode, the oxidation of the absorbed and adsorbed hydrogen occurs.^{122,123}



At a potential range above -150 mV, an oxide layer of PdPt(II) forms on the surface of the catalyst. Although the mechanism of this oxidation process remains unclear, it has been widely accepted that OH⁻ ions are first chemisorbed at the initial stage on the oxide formation, which is usually observed in the potential range between -700 and -300 mV. The oxidation reaction follows this mechanism:¹²⁴



Following to the oxidation process, the sharp peak (at the potential around -225 mV) at the backward sweep (cathodic part/ reduction process) can be attributed to the reduction of the PdPt(II) oxide (eq 3.14)

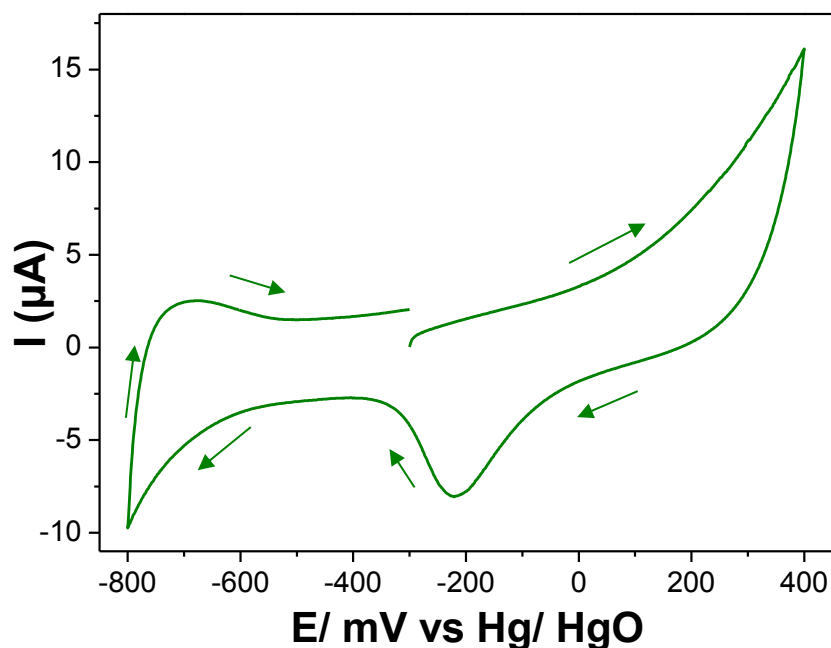


Figure 3.14 Cyclic voltammogram of PdPt bimetallic nanoballs in 1 M of KOH with a scan rate of 20 mV/s. The arrows indicate the direction of measurements.

b. Mechanism of ethanol oxidation on PdPt nanoballs used as electrocatalysts

Figure 3.15 shows a cyclic voltammogram of Pd₇₅Pt₂₅ nanoballs in 1 M of KOH in the presence of 1 M of ethanol. As it can be seen, after adding ethanol, the signals corresponding to the oxidation and reduction of PdPt nanoballs disappeared. The ethanol oxidation reaction starts around -600 mV and a peak centered at -125 mV is observed

during the forward scan. In the reverse scan, another peak is found centered at about -200 mV. The forward scan peak is related to the oxidation of freshly chemisorbed species issued from alcohol adsorption, while the reverse scan peak represents the removal carbonaceous species not completely oxidized in the forward scan.^{125,126}

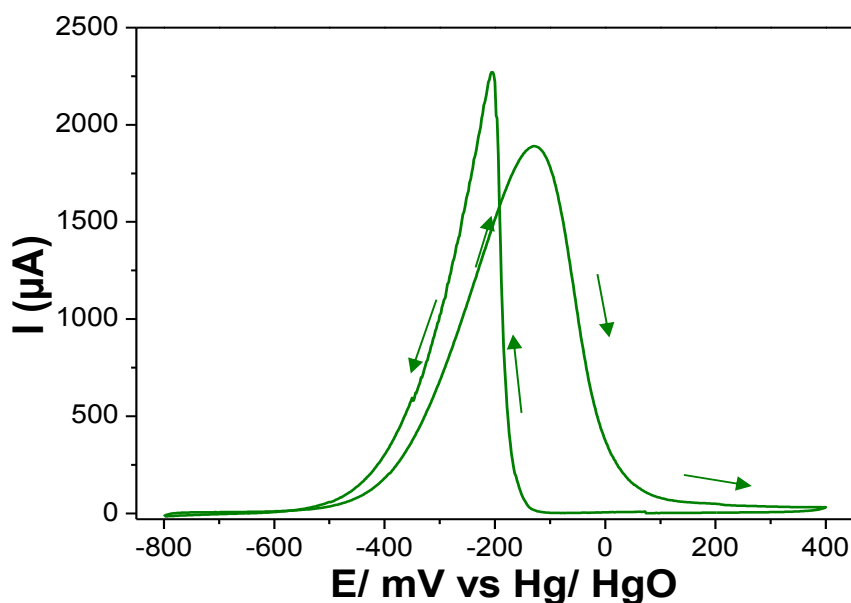


Figure 3.15 Cyclic voltammogram of Pd75Pt25 nanoballs in 1 M of KOH + 1 M of ethanol with the scan rate of 50 mV/s.

Zhou *et.al.* have shown for Pd material that most of ethanol was incompletely oxidized to acetate.¹²⁷ The selectivity for ethanol oxidation to CO₂ (existing as CO₃²⁻ in alkaline media) was determined as low as 2.5%. In a previous work, we have shown that the main final product of ethanol oxidation reaction (EOR) is acetate.¹²⁴

c. Tuning the composition of porous PdPt bimetallic nanoballs for ethanol oxidation reaction

Pt is the most active electrocatalyst for most of the reaction involved in fuel cells. However, pure Pt is not durable in alcohol oxidation reactions because of its poisoning by CO. Combining Pt with another metal such as Au or Pd can be an alternative way to solve these issues. Indeed, the bimetallic Pt-Pd nanostructures are expected to exhibit

enhanced activity.. Here, we show that Pd-Pt nanoalloys with porous nanoballs shapes exhibit high electrocatalytic activity for ethanol oxidation. Four different Pd/Pt ratio for the metal salts were used 0/1, 1/3, 1/1, 3/1 and 1/0 (corresponding to the synthesized nanostructures noted Pt₁₀₀, Pd₂₅Pt₇₅, Pd₅₀Pt₅₀, Pd₇₅Pt₂₅, Pd₁₀₀) while keeping a total salt concentration of 0.1 M.

Figure 3.16 shows cyclic voltammograms (CVs) for ethanol oxidation using PdPt nanoballs catalysts with different compositions. These CVs show that the ethanol oxidation activities are higher with bimetallic PdPt nanoballs compared to pure Pd and pure Pt nanostructures. Pd exhibits a higher activity and stability for ethanol oxidation compared to pure Pt (due to the poisoning effect with CO on the surface of Pt catalyst) (**Figure 3.16 and 3.17**). However, Pt gives higher ratio of forward peak current (if) to backward peak current (ib, which corresponds to the removal carboneous species, which are not completely oxidized in the forward scan) (if/ib)). Indeed, previous works suggest that Pt is more active for C-C bond cleavage compared to Pd, which selectivity for complete ethanol oxidation to carbonate in alkaline media is as low as 2.5 %.^{127,128} Bimetallic PdPt nanoballs show higher activity and stability compared to pure Pd and pure Pt due to synergetic effects between these two metals (**Figure 3.16 and 3.17**).

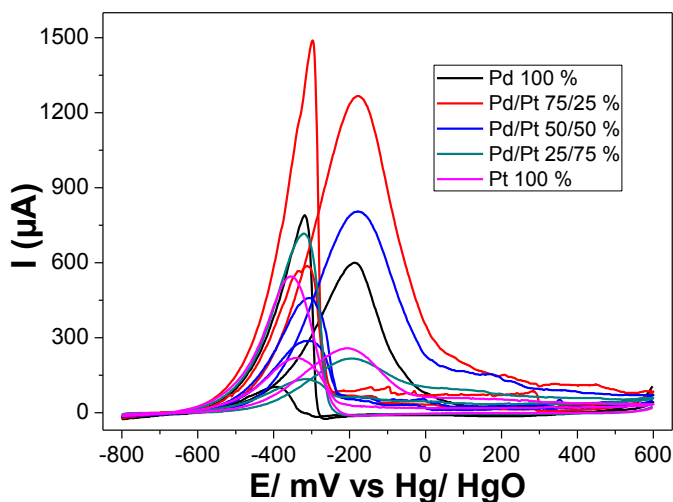


Figure 3.16 Cyclic voltammograms of Pd, Pt, and PdPt nanoballs with different composition (same pore size, $O/W = 1.5$) in 1 M of KOH + 1 M of ethanol after 50 cycles (scan rate 50 mV/s).

Chronoamperometry was used to monitor the stability of the catalyst for ethanol oxidation. **Figure 3.17** shows the chronoamperometry graph at a fixed potential (-0.3 V) for 1 hour. Pd₇₅Pt₂₅ gives the highest current as measured after 1 hour.

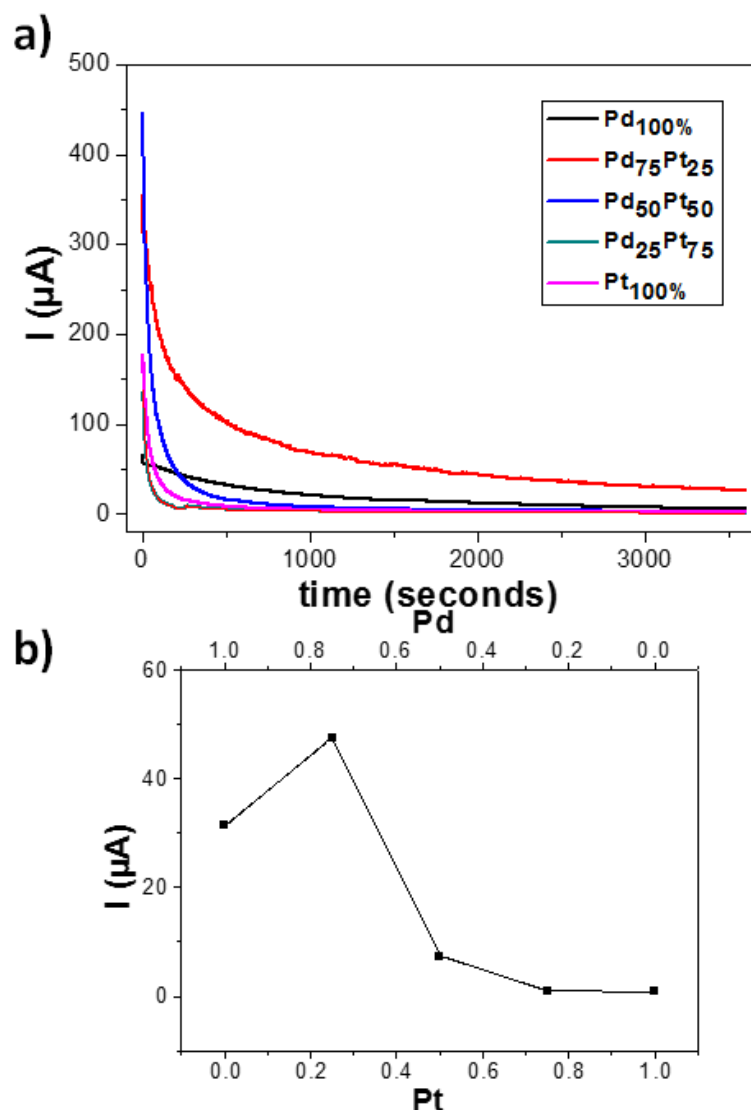


Figure 3.17. Chronoamperometry at the potential of -0.3 V with different ratios of Pd and Pt (a), current measured after 1h of chronoamperometry Versus the Pt fraction (bottom x axis) or the Pd fraction (top x axis) (b).

According to the literature, the ethanol oxidation using PdPt as electrocatalyst takes place on the surface via ethanol adsorption followed by reaction with hydroxyl ions leading to CH_3COO^- as the final product through the following reaction (Equation 3.16 to 3.17):



According to the band theory, the band center of Pd will be shifted upward, when it is combined with Pt.¹¹² This can further promote removal of adsorbed carbonaceous species (which inhibit the oxidation reaction of ethanol on the surface of the catalyst) and increase the adsorption of OH⁻ (as the rate determining step in ethanol oxidation reaction), and thus help to enhance the ethanol oxidation process. Furthermore, alloying Pt with Pd can suppress the poisoning effect of CO. Palladium metal can effectively adsorb water at lower potential. Rationally, the adsorbed CO on Pt surface and the availability of OH_{ads} on the Pd surface can lead to the oxidation reaction of CO into CO₂.

d. Influence of the pore size of pure Pd nanoballs on their electrocatalytic activity towards ethanol oxidation

Influence of the pore size on the electro Active Surface (EAS)

Electro active surface (EAS) is an important parameter that can determine the current produced during an electrocatalytic reaction. Cyclic voltammetry (CV) has been used to estimate the EAS. **Figure 3.18** shows the typical cyclic voltammogram of pure Pd nanoballs in 1 M of KOH solution. The blue area is associated to the desorption of hydrogen atoms, which were adsorbed/absorbed in the negative going sweep at the potential between -800 to -500 mV. On the other hand, the red area is associated to the Pd-oxide reduction peak.

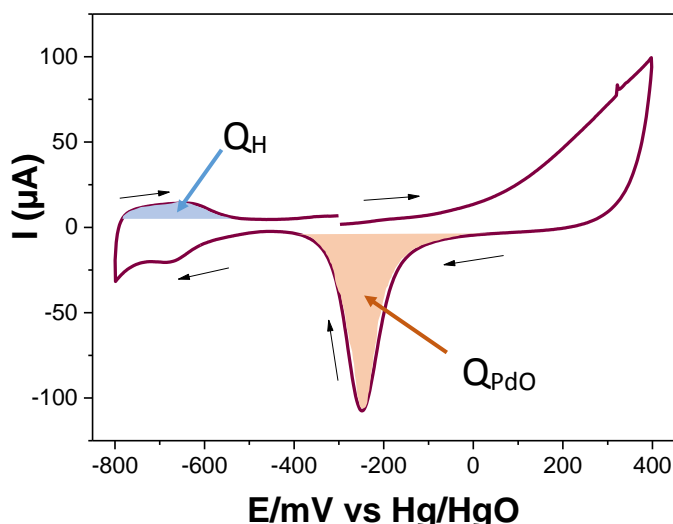


Figure 3.18 Cyclic voltammogram of pure Pd nanoball (O/W = 4.5) in 1 M of KOH at the scan rate of 20 mV/s.

According to the literature, the electrochemical active surface of Pd was measured through the integration of charges in the hydrogen desorption peak or in the Pd oxide reduction peak (Equation 3.22 and 3.23).^{117,129–131}

$$EAS = \frac{Q_H}{0.21} \quad (\text{Equation 3.18})$$

$$EAS = \frac{Q_{PdO \text{ reduction}}}{0.405} \quad (\text{Equation 3.19})$$

Where, Q_H is the calculated charge for hydrogen desorption, Q_{PdO} is the calculated charge for PdO reduction, 0.21 is the charge associated with monolayer adsorption of hydrogen, and 0.405 is the charge value assumed for reduction of PdO monolayer. The charge values are deduced from the integrals (surfaces) of the hydrogen desorption peak and the Pd oxide reduction peak. Table 3.5 and 3.6 give the charge value and electro active surface of Pd nanoballs which are calculated based of hydrogen desorption peak (table 3.5) and PdO reduction peak (table 3.6) .

Table 3.5 The EAS of pure Pd nanoballs as estimated from the area of Hydrogen desorption peak

Sample (O/W)	$Q(C) = (m_m/m_{cal}) * Q_{cal}$	EAS (cm²)
1.5	1.05E-05	0.050
2.5	4.42E-05	0.211
3.75	7.45E-05	0.355
4.5	8.64E-05	0.411

Table 3.6 The EAS of pure Pd nanoballs as calculated from the area of PdPt oxide reduction peak

Sample (O/W)	$Q(C) = (m_m/m_{cal}) * Q_{cal}$	EAS (cm²)
1.5	8.18E-05	0.202
2.5	2.87E-04	0.708
3.75	4.71E-04	1.162
4.5	5.47E-04	1.351

Figure 3.19a presents the cyclic voltammogram of Pd nanoballs synthesized in mesophases with different O/W ratio. The H adsorption-absorption/desorption peaks at the potential between -800 to -600 mV/s and PdO oxide reduction peaks at the potential around -225 mV increase with O/W ratio. **Figures 3.19 b,c** show the dependence of EAS (calculated based on the hydrogen desorption peak or based on Pd-oxide reduction peak) on the pore size (which is controlled by the O/W ratio, as shown above). The results show that the EAS increases with the pore size of the nanoballs. Indeed, large pore size can promote the mass transfer and effectively exposes the inner and outer surface to the reactants or the molecules involved in the electrocatalytic process.

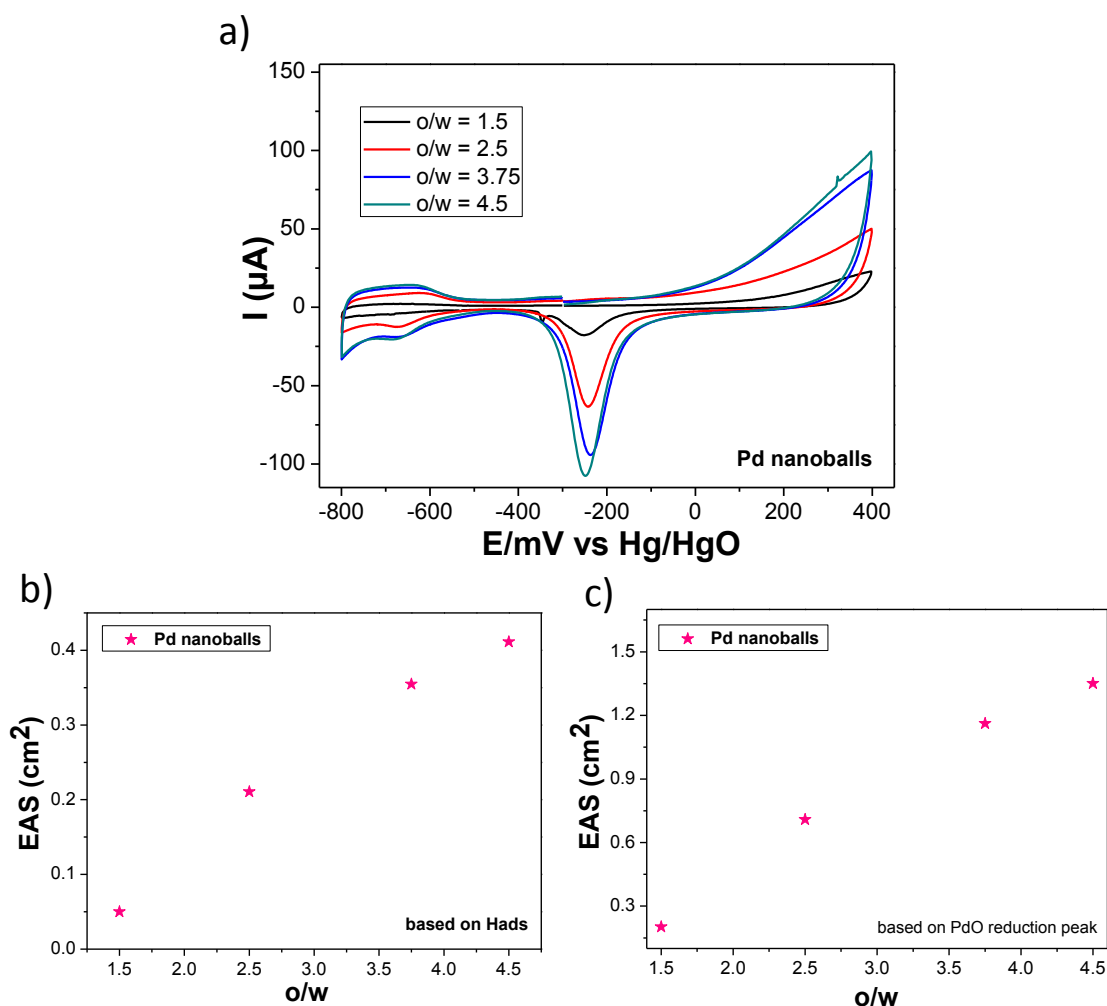


Figure 3.19 (a) Cyclic voltammetry of pure Pd nanoballs in 1 M of KOH; Electro active surfaces as a function of O/W ratio, which was measured based on hydrogen desorption peak; and (b) Pd-oxide reduction peak(c).

The method of EAS estimation from H_{ads} peak and PdO reduction peak gives two different values of EAS for a same sample. The difference could be explained by the fact that the $H_{\text{ads/abs}}$ peak is not only characteristic of H_{ads} . Moreover, in the literature, the EAS estimation from PdO reduction peak is controversial because it depends on the oxidation scan potential window. In order to estimate the EAS with more accuracy, CO stripping measurements are planned in collaboration with Teko Napporn from Université de Poitiers. However, these first EAS estimations showed a clear trend: the EAS increases with the porosity.

The electrocatalytic activities of pure Pd nanoballs with different pore sizes were tested for ethanol oxidation reaction. **Figure 3.20a and b** clearly shows that the current produced during ethanol oxidation increases with the pore size of the nanoballs. This is due to the fact that the electro active surface area increases with the pore size.

The activity of an electrocatalyst is quantified with a current density, which is calculated in normalizing the current with the EAS. The current density is highly enhanced when the O/W increases from 1.5 to 2.5. Then, if the O/W ratio is further increased from 2.5 to 4.5, the current density only slightly increases. As what has been explained in the previous part (in the section of porous materials in electrocatalysis), the porosity of nanomaterials not only controls the active surface area, but also the transport of reactant and products. We assume, at very small porosity of Pd nanoballs, the transport of reactant and product into and out of the electrocatalysts will be more difficult, thus resulting in lower current density.^{101,132}

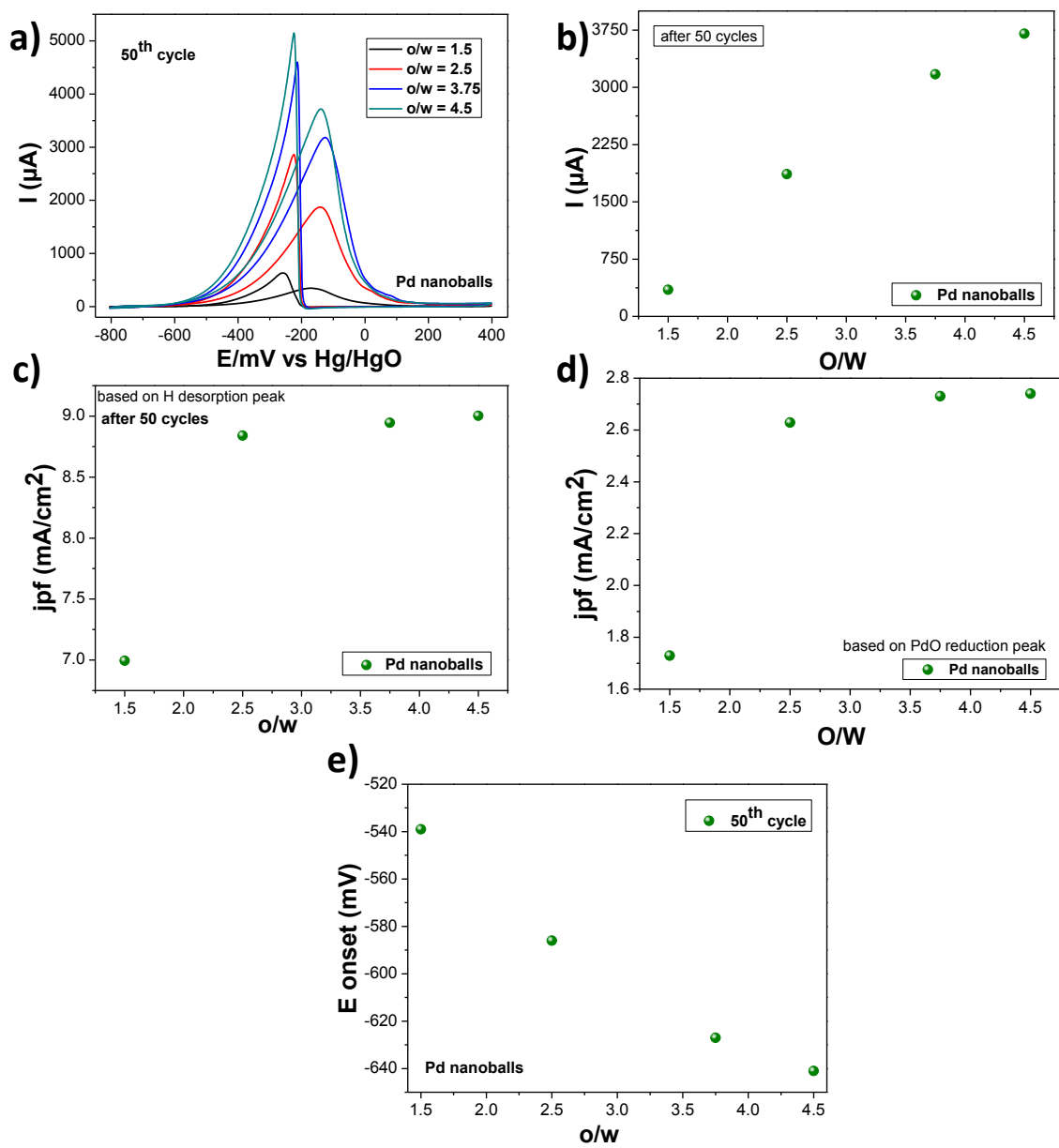


Figure 3.20 a) Cyclic voltammety of Pd nanoballs with different pore size in 1 M of KOH containing 1 M of ethanol at the scan rate of 50 mV/s; b) Forward peak current measured after 50 cycles as the function of O/W ratio; c) Current density after 50 cycles based on hydrogen desorption peak, d) Current density after 50 cycles based on PdO reduction peak. The line is a guide for the eye; e) E onset after 50 cycles as the function of O/W ratio.

Figure 3.20e gives the onset potential of ethanol oxidation reaction using pure Pd nanoballs with different pore sizes as catalysts. It is clearly shown that pure Pd catalyst with larger pore size gives a more negative onset potential. The negative potential shift

from -540 to -640 mV underscores that Pd nanoballs with larger pore size are thermodynamically more effective for ethanol oxidation reaction.

The onset potential is a potential at which the oxidation or reduction reaction starts to occur. The onset potential of an electrocatalytic reaction is frequently used as an indicator to compare the catalytic performance of electrocatalyst.¹³³ In this case, the onset potential is measured as the potential at which the ethanol oxidation reaction starts. The most appropriate way of determining onset potential is to draw a horizontal line in non-faradaic zone. The point where the line intersects with the curve for ethanol oxidation gives the value of onset potential (**Figure 3.21**).

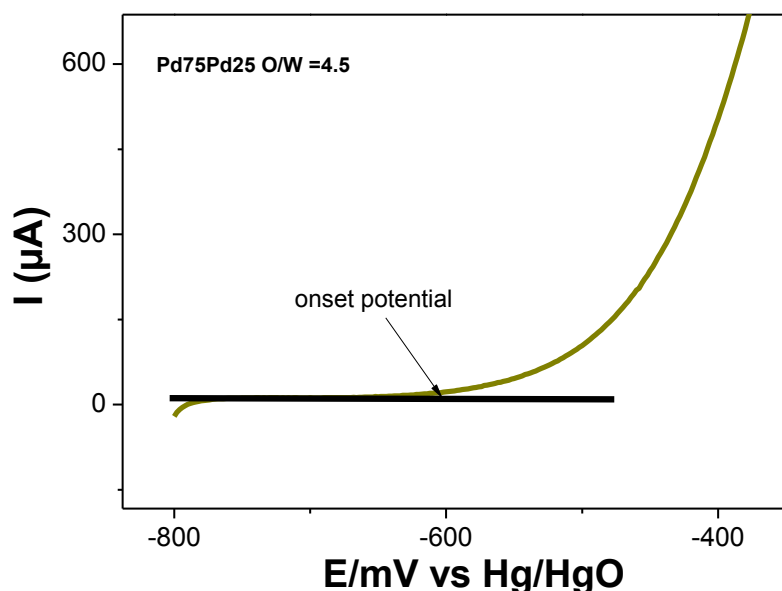


Figure 3.21 A zoom of cyclic voltammogram of ethanol oxidation reaction on Pd₇₅Pt₂₅ nanoballs (O/W = 4.5).

f. Influence of pore size of Pd₇₅Pt₂₅ nanoballs on their electrocatalytic activity towards ethanol oxidation

Influence of the pore size on the electro Active Surface (EAS)

The influence of the pore size on the electro active surface area was also studied using Pd₇₅Pt₂₅ nanoballs as they behave as the best catalyst in term of activity and stability for ethanol oxidation reaction in our system.

As already shown for pure Pd nanoballs, Pd₇₅Pt₂₅ nanoballs also show an increase of electro active surface with porosity as calculated from the surface charge in hydrogen desorption peak and in PdPt oxide reduction peak (**Figure 3.22**).

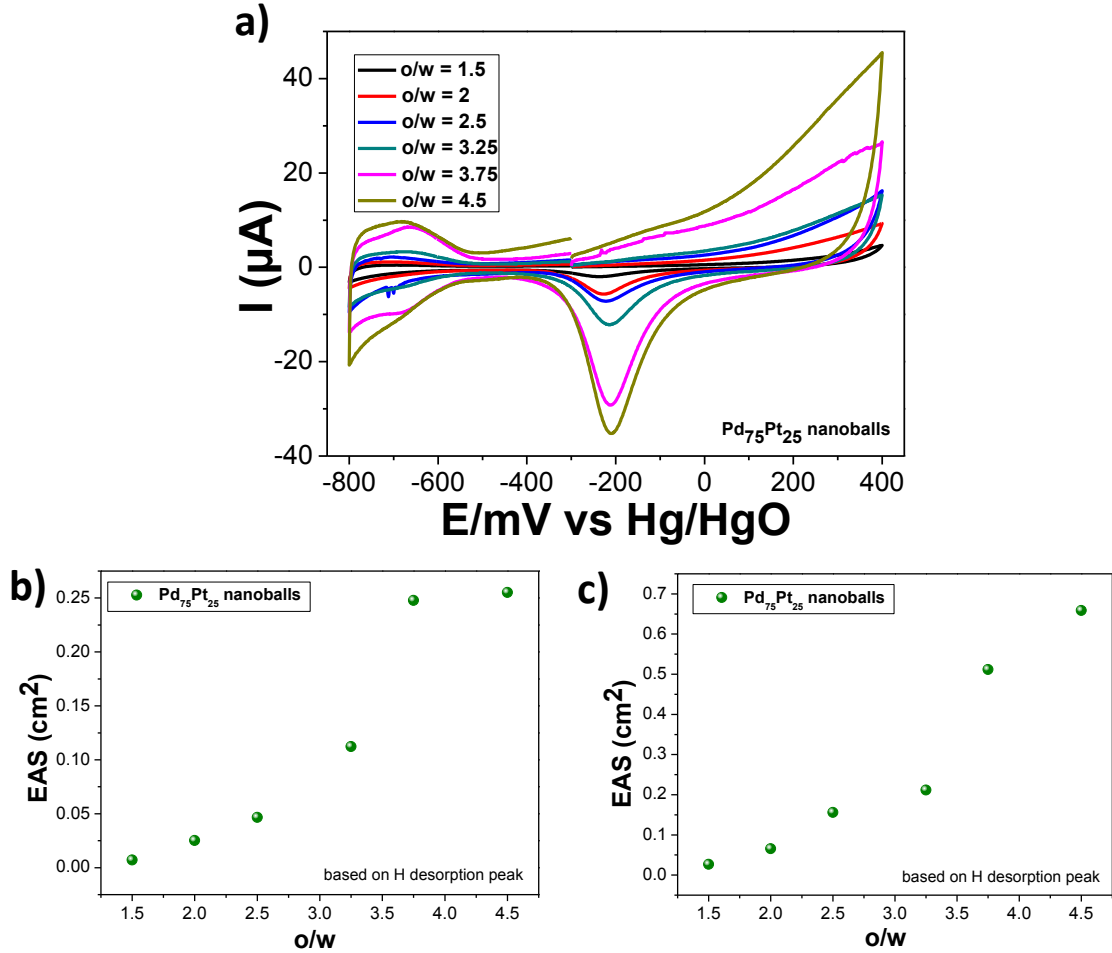


Figure 3.22 (a) Cyclic voltammetry of Pd₇₅Pt₂₅ nanoballs in 1 M of KOH; Electro active surfaces as the function of O/W ratios measured based on hydrogen desorption peaks, and (b) PdPt-oxide reduction peaks (c).

For Pd₇₅Pt₂₅ nanoballs, the equations to calculate electro active surface are given below:

$$EAS = \frac{Q_H}{0.21} \quad (\text{Equation 3.20})$$

$$EAS = \frac{Q_{PdPt-oxide}}{0.409} \quad (\text{Equation 3.21})$$

Where, Q_H is the calculated charge for hydrogen desorption, Q_{PdPt} oxide is the calculated charge for PdPt oxide reduction, 0.21 is the charge value of hydrogen

adsorption/desorption monolayer on the surface of electrocatalysts, and 0.409 is the charge value assume for reduction of Pd₇₅Pt₂₅ oxide monolayer. The charge value for Pd is known to be 0.405 mC cm⁻² ¹²⁹, while for Pt it is 0.420 mC cm⁻² ¹³⁴. Therefore, the charge value for Pd₇₅Pt₂₅ is calculated as below:

$$\begin{aligned} \text{charge value} &= (0.75 \times \text{charge value of Pd}) + (0.25 \times \text{charge value of Pt}) \\ &= (0.75 \times 0.405) + (0.25 \times 0.420) = 0.409 \text{ mC cm}^{-2} \end{aligned}$$

Tables 3.7 and 3.8 show the calculated charge value and electro active surface of Pd₇₅Pt₂₅ nanoballs as calculated from the area of hydrogen desorption peak (**Table 3.7**) and PdPt oxide reduction peak (**Table 3.8**).

Table 3.7 The EAS of Pd₇₅Pt₂₅ nanoballs as calculated from the area of Hydrogen desorption peak

Sample (O/W)	Q(C) = (mm/m _{cal})*Q _{cal}	EAS (cm ²)
1.5	1.49E-06	0.007
2	5.28E-06	0.025
2.5	9.79E-06	0.047
3.25	2.36E-05	0.112
3.75	5.20E-05	0.248
4.5	5.36E-05	0.255

Table 3.8 The EAS of Pd₇₅Pt₂₅ nanoballs as calculated from the area of PdPt oxide reduction peak

Sample (O/W)	Q(C) = (mm/m _{cal})*Q _{cal}	EAS (cm ²)
1.5	1.09E-05	0.027
2	2.68E-05	0.065
2.5	6.38E-05	0.156
3.25	8.65E-05	0.211
3.75	2.09E-04	0.512
4.5	2.69E-04	0.659

Influence of pore size of on their electrocatalytic activity for ethanol oxidation reaction

The electrocatalytic activity of Pd₇₅Pt₂₅ nanoballs with different pore sizes were tested for ethanol oxidation reaction. **Figure 3.23a and b** clearly shows that the current produced during ethanol oxidation increases with the pore size of the nanoballs, as seen above in the case of pure Pd nanoballs. Stability is an important parameter to determine the quality of an electrocatalyst. Here, we also perform chronoamperometry with different pore sizes of nanoballs at a constant potential of -300 mV to study the effect of the pore size on the electrocatalysts stability (**Figure 3.23 c and d**). The current produced at the time 0 and after 1 h of chronoamperometry increases with the pore size. The current after 1 h of chronoamperometry decreases by about 50 % compared to the initial current for all the samples. These chronoamperometry results suggest that the stability does not depend on the pore size of the catalysts.

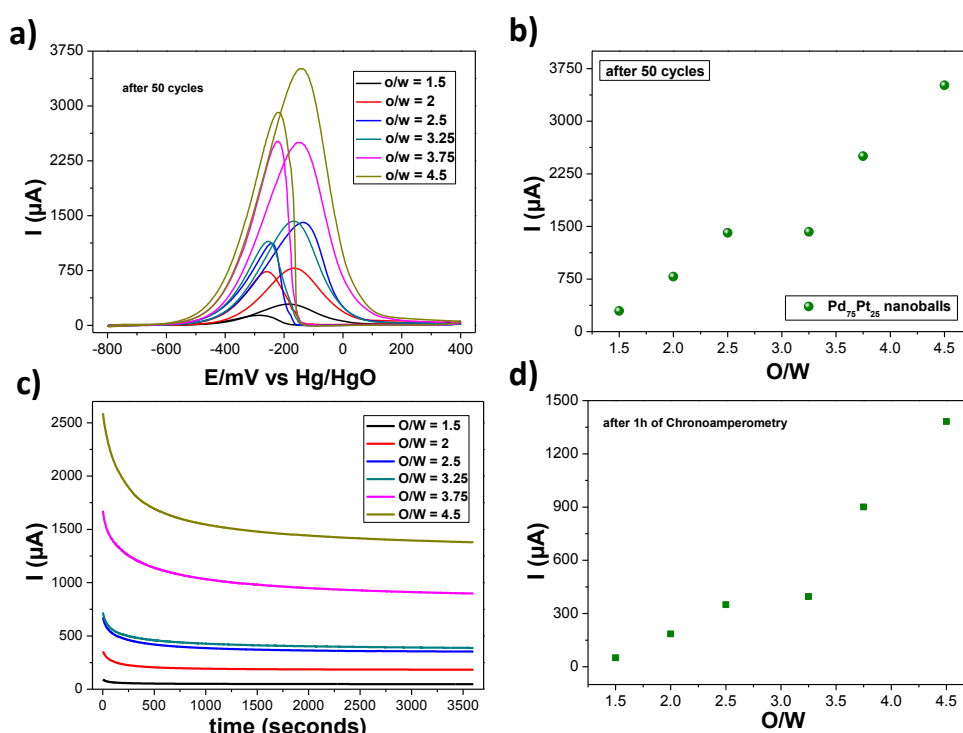


Figure 3.23 (a) Cyclic voltammetry of Pd₇₅Pt₂₅ nanoballs in 1 M of KOH + 1 M of ethanol at the scan rate of 50 mV/s with different O/W ratios; (b) the forward peak current after 50 cycles; (c) Chronoamperometry curves at -300 mV for 1 h for Pd₇₅Pt₂₅ nanoballs with different pore size, and (d) the current measure after 1 h of chronoamperometry.

Current density of the forward peak current to the electro active surface was used to define the catalyst activity. Surprisingly, in sharp contrast with our results for pure Pd nanoballs (fig. 3.18), the current density measured after 50 cycles decreases with the pore size of the nanoballs as shown in **Figure 3.24**. However, if we look at the numerical values, we can see that the current densities of the bimetallic Pd₇₅Pt₂₅ nanoballs (even the lowest one) are still larger than those of Pd nanoballs. The value of E onset is also shifted to a more positive potential, indicating that the ethanol oxidation with larger pore size of Pd₇₅Pt₂₅ nanoballs is thermodynamically less favorable. HAADF-TEM and EDS showed that the composition in Pd and Pt on the surface of nanoballs changed with the pore size. At larger pore size, the percentage of Pd on the surface of nanoballs is higher (at a fixed initial concentration), explaining the decrease of the current density with pore size. Higher amount of Pd on the surface at larger pore size is thus assumed to be the cause of less active electrocatalysts.

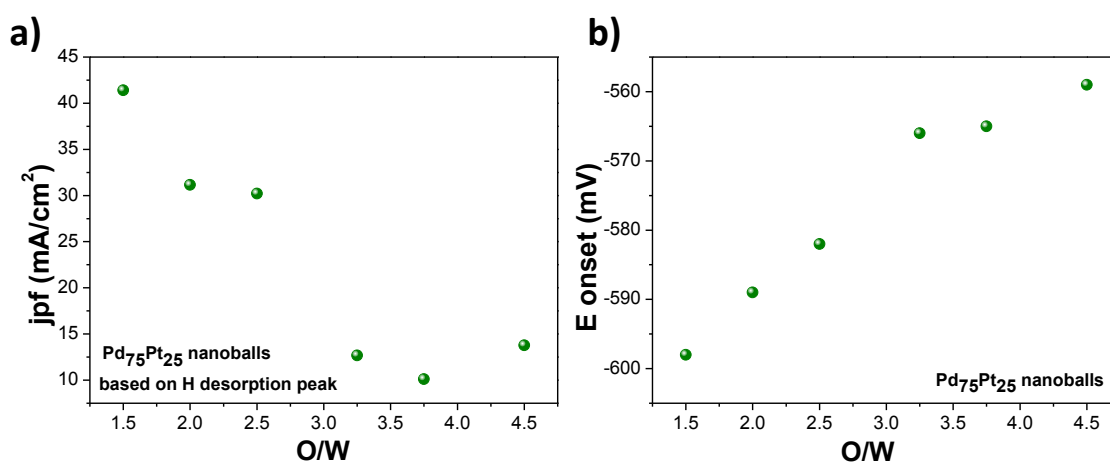


Figure 3.24 Current density (measured by the integration of forward peak current to the electro active surface (from hydrogen desorption peak)) as the function of O/W ratio (which fixes the pore size of nanoballs).

Conclusion

Porous Pd, Pt, and PdPt (with controlled compositions) nanoballs with tunable pore sizes were obtained by controlling the diameter of the oil tubes of hexagonal mesophases (which can be tuned by varying the ratio of oil to water). The mesophases doped with Pd and Pt complexes are stable with swelling. Analysis by TEM, BET, SAXS, and WAXS show that the pore sizes of nanoballs can be tuned from 16 to 45 nm. We

found that the pore size is equal to the diameter of the oil tube of the mesophase, proving a templating effect. These porous metal nanoballs were used as electrocatalysts for ethanol oxidation reaction in alkaline solution. The composition of Pd and Pt was also varied, and Pd₇₅Pt₂₅ appeared to be the best electrocatalyst in term of activity and stability for this reaction. Cyclic voltammetry analysis showed that the electro active surface increased with porosity, which then led to the current increase. In the case of Pd nanoballs, the current density increased when the pore size increased from 16 to 20 nm and reached a plateau for pore sizes higher than 20 nm. However, in the case of PdPt nanoballs, the current density decreased with the pore size. These phenomena were then explained thanks to HAADF-TEM and EDS characterizations, which showed that the composition in Pd and Pt on the surface of the nanoballs changed with the pore size. At larger pore size, on the surface the ratio Pd/Pt increases (at a fixed initial concentration), explaining the decrease of the current density with pore size. Higher amount of Pd on the surface at larger pore size is thus assumed to be the cause of less active electrocatalysts.

III.3 Synthesis of bimetallic (Au@Pd and Au@Pt core shell) and trimetallic AuPdPt nanostructures for ethanol and glucose oxidation reactions

Pd is widely used catalyst for ethanol oxidation reaction in alkaline condition. However, problem of relatively low catalytic activity and poor durability of Pd remains a significant challenge in the development of DEFCs. There are several ways to address this issue such as designing Pd porous nanostructures (which is expected can improve the active side by providing high surface area) and combining Pd with other metal which might improve catalytic activity because of the synergetic effect between the two or more metals.

In the previous part we have shown that, bimetallics of PdPt have higher activity and stability compared to monometallic of Pd and Pt. Furthermore, recent reports have demonstrated that the incorporation of Au into Pd give noteworthy enhancement of electrocatalytic performance for ethanol oxidation reaction.¹³⁵⁻¹³⁷ Here, we prepared Au@Pd, Au@Pt, and trimetallic of AuPdPt in hexagonal mesophases for ethanol oxidation reaction in alkaline solution

III.3.1 Material characterization

Here, like for the synthesis of PdPt nanoballs, we used the templates provided by hexagonal mesophases made of CTAB as surfactant, cyclohexane, brine, and n-pentanol as co-surfactant for synthesis of Au@Pd, Au@Pt, and AuPdPt nanostructures. The composition of Au/Pd and Au/Pt mixtures were varied as follows: Au₅Pd₉₅, Au₁₀Pd₉₀, Au₅Pt₉₅, Au₁₀Pt₉₀. The hexagonal mesophases containing Au (ethylenediamine gold (III) ([Au(en)₂]Cl₃)), Pd (Pd(NH₃)₄Cl₂) and/or Pt (Pt(NH₃)₄Cl₂) metallic complexes were exposed to gamma irradiation. The pentanol, used as co-surfactant, contributes to Au (III) and Pd (II) or Pt (II) reduction on the radiolysis induced seeds. After 24 hours of irradiation, a black gel was obtained.

TEM images (**Figure 3.25 and 3.26**) revealed the formation of core-shell nanostructures formed by a dense of core and a porous metal. The characterization using selected area electron diffraction (SAED) indicates that the core is gold, and the shell is made of Palladium or Platinum.^{88,104} **Figure 3.25** presents the TEM images of AuPd core-shell nanostructures with two Au/Pd ratios (Au₅Pd₉₅ and Au₁₀Pd₁₀). The two compositions yield comparable nanostructures: we find that the average size of the Au core and AuPd core shell mesoporous nanoballs is about 36 nm and 90 nm respectively (measured for 8 core-shell mesoporous nanoballs in **Figure 3.26c**). Gold is presumably reduced first, leading to particles with large Au cores. The templating effect provided by the mesophase is observed for Pd which is reduced on the Au core leading to a porous Pd shell formed by connected nanowires. The size of the cores are much larger than the confined aqueous phase of hexagonal mesophases.⁵¹ It has to be noted that the template is soft and the particles can grow creating few deformations (or defects) in the mesophases.

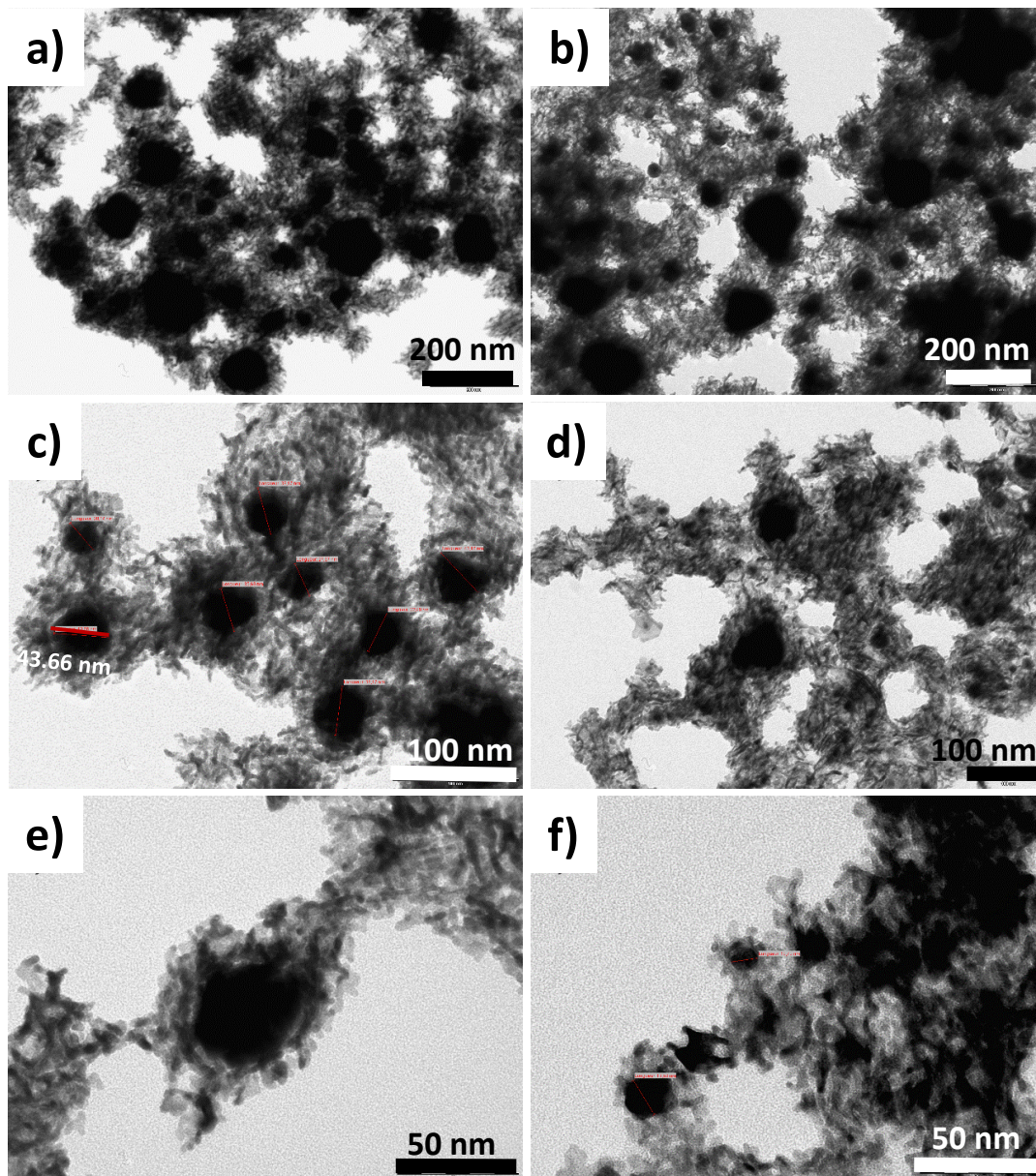


Figure 3.25 TEM images of Au@Pd core shell mesoporous nanoballs with different composition of Au and Pd; Au₁₀@Pd₉₀ (a, c, e) and Au₅@Pd₉₅ (b, d, f).

Figure 3.26 presents the TEM images of Au@Pt core-shell nanostructures with two ratios Au/Pt (10/90 and 5/95). Unlike Au@Pd, here the Au cores are much larger (around 90- 200 nm) for Au₁₀Pt₉₀ than for the samples comprising twice less Au precursor (around 40-90 nm) for. The shell are made by 3D-connected nanowires of Pt with 3 nm diameter (diameter of the water channel) forming pores with a hexagonal structure. Further characterization techniques such as HAADF-TEM, EDS, and XPS are necessary

to better characterize the structure and determine the oxidation states of Au@Pd and Au@Pt core-shell mesoporous nanoballs.

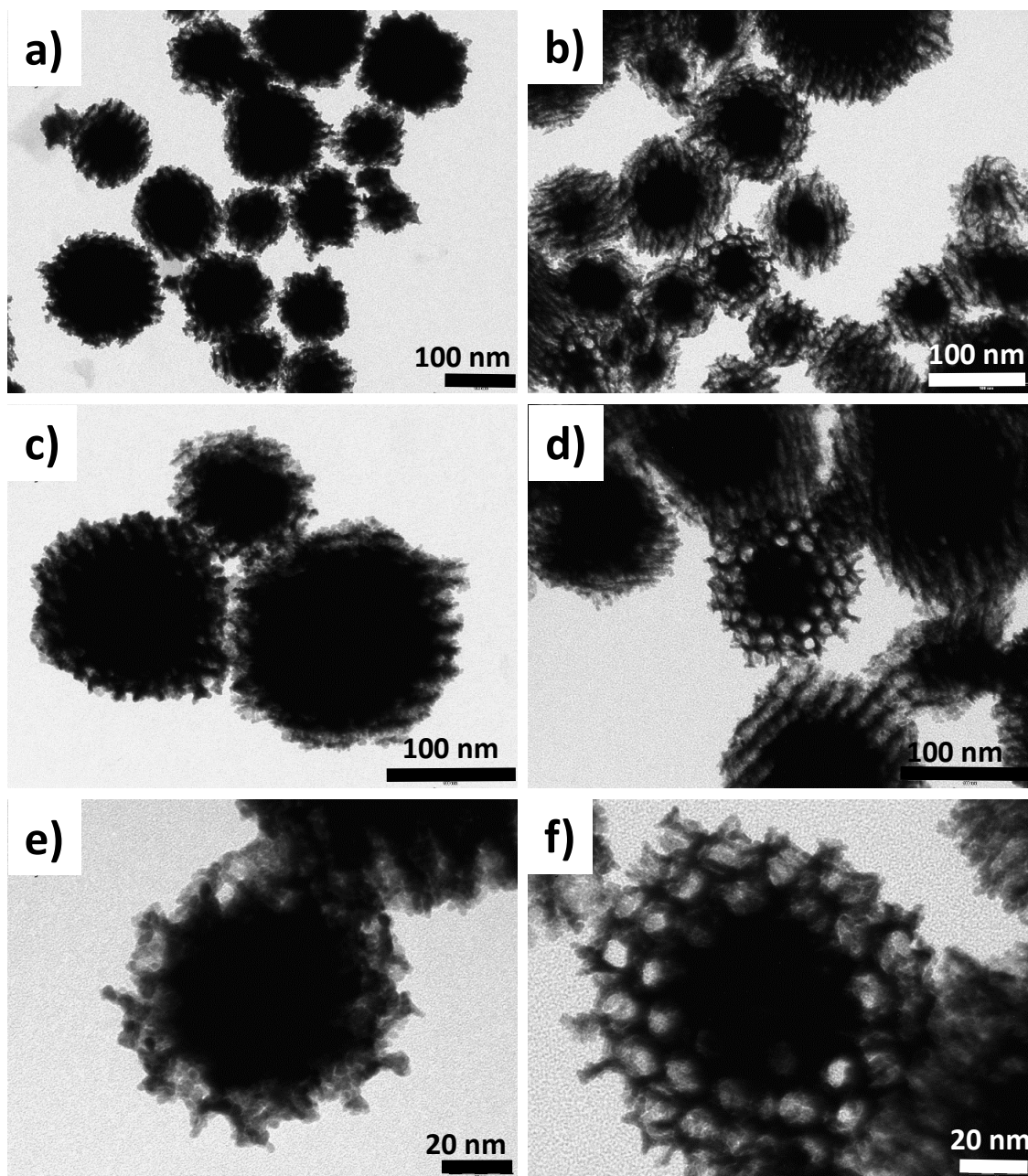


Figure 3.26 TEM images of Au@Pt core shell mesoporous nanoballs with different composition of Au and Pt; Au₁₀@Pt₉₀ (a, c, e) and Au₅@Pt₉₅ (b, d, f).

The formation of core-shell structure for the sample of Au@Pd and Pt@Pt can be due to use of low dose rate during radiolytic synthesis process. The electron transfer from Pd^I/ Pt^I or nascent Pd⁰/Pt⁰ induced by radiolysis to gold complexes (Au III or Au I)

occurring only at low dose rate when the reduction kinetics is slow. Previous results show that, in the case of synthesis of Au-Pt by electron beam (very high dose rate) produced alloys of Au-Pd, no formation of core-shell structure observed.¹³⁸

Like in the case of bimetallic of PdPt (which was also prepared in the soft template hexagonal mesophases and the reduction of metallic salt was induced by gamma irradiation), trimetallic $Au_5Pd_{70}Pt_{25}$ nanostructures are formed by porous nanoballs. There is no core of gold observed in this case. EDS mapping confirm the presence of Au, Pd, and Pt. The peak of Au is very weak, indeed these trimetallic nanostructures consist in only 5 % of Au (**Figure 3.27**). Further HAADF-STEM analysis is still needed to be performed to investigate the structure of AuPdPt, whether it is an alloy or not.

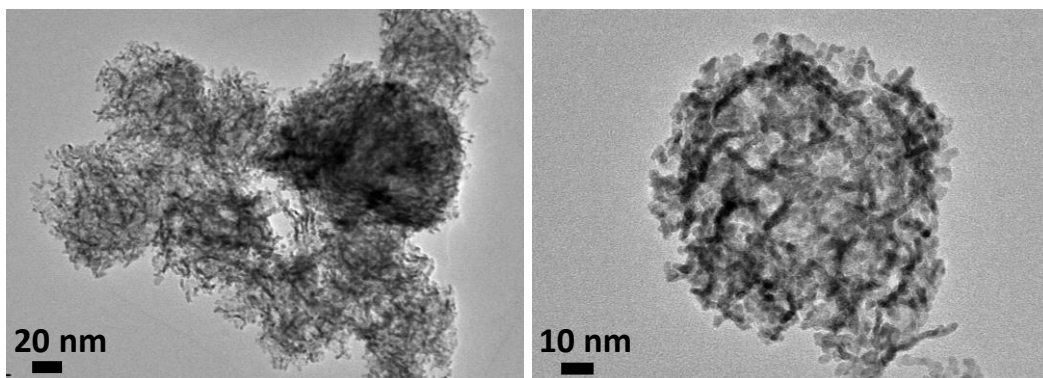


Figure 3.27 TEM images of $Au_5Pd_{70}Pt_{25}$ nanoballs synthesized in mesophases with dose rate of 3.5 kGy/h (total dose 84 Gy)

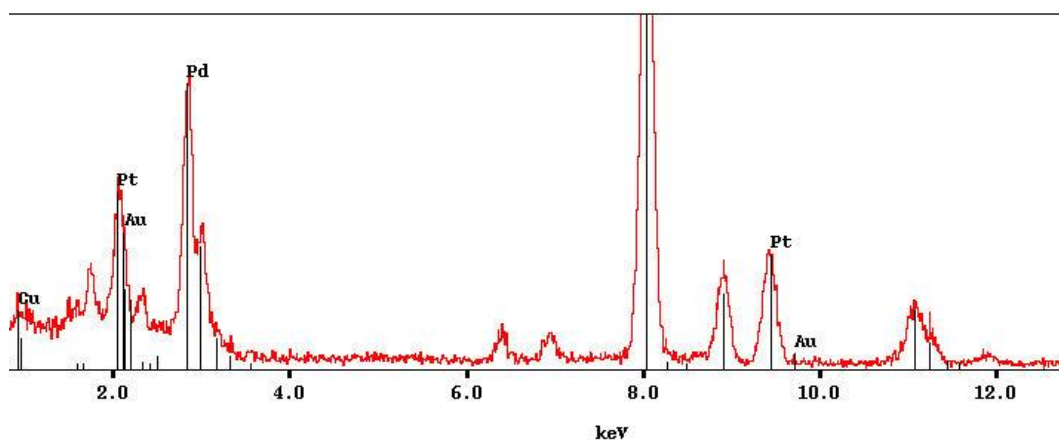


Figure 3.28 EDS profile of trimetallic of $Au_5Pd_{70}Pt_{25}$

III.3.2 Application of Au@Pd, Au@Pt, and AuPdPt for ethanol oxidation reaction

The electrocatalytic activity of Au@Pd and AuPdPt is tested for ethanol oxidation. The activity of these electrocatalysts is also compared to Pd nanoballs and Pd₇₅Pt₂₅ nanoballs. **Figure 3.29** presents cyclic voltammograms of electrocatalysts in 1 M of KOH. The working electrode is a glassy carbon electrode modified with samples (Pd, Pd₇₅Pt₂₅, Au₅Pd₇₀Pt₂₅ nanoballs, and Au₅Pd₉₅ core-shell) which were embedded in PDPB on its surface. Like in the case of Pd₇₅Pt₂₅ (which has been discussed in the previous part), at a potential range smaller than -500 mV vs Hg/HgO reference electrode, the oxidation of the absorbed and adsorbed hydrogen occurs.^{122,123} (equation 3.11)

At a potential range above -150 mV, an oxide layer of Pd, PdPt(II), AuPd(II), or AuPdPt(II) forms on the surface of the catalyst. Although the mechanism of this oxidation process remains unclear, it has been widely accepted that OH⁻ ions are first chemisorbed at the initial stage on the oxide formation, which is usually observed in the potential range between -700 and -300 mV. The oxidation reaction follows this mechanism on equation 3.12 – 3.14.¹²⁴

Following to the oxidation process, the sharp peak (at the potential around 286 to 228 mV) at the backward sweep (cathodic part/ reduction process), can be attributed to the reduction of the oxide layer of Pd, PdPt(II), AuPd (II), or AuPdPt(II) (following the reaction 3.15). Sample of Au₅Pd₉₅ (-282 mV) gives more negative onset potential compare to our Pd nanoballs (-272 mV). For the sample containing Pt, the reduction peak shift to the more positive potential; for Pd nanoballs the reduction peak of PdO is at -272 mV, while for Pd₇₅Pt₂₅ nanoballs the reduction peak of PdPt-O is at -230 mV. The reduction peak of Au₅Pd₇₀Pt₂₅ (-240 mV) nanoballs is more negative compare to Pd₇₅Pt₂₅ (-230 mV) nanoballs due to the presence of small amount of gold.

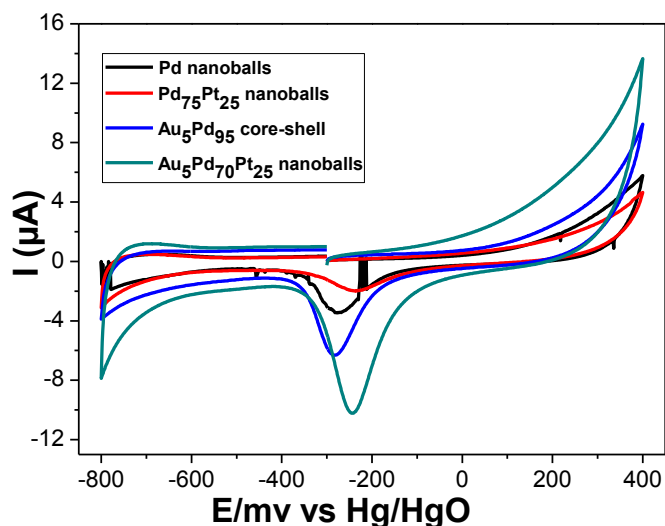


Figure 3.29 Cyclic voltammogram of Pd nanoballs, Pd₇₅Pt₂₅ nanoballs, Au₅Pd₉₅ core-shell, and Au₅Pd₇₀Pt₂₅ nanoballs in 1 M of KOH at the scan rate of 20 mV/s.

Figure 3.30 shows cyclic voltammogram of ethanol oxidation reaction using different electrocatalysts; Pd nanoballs, Pd₇₅Pt₂₅ nanoballs, Au₅Pd₉₅ core-shell, and Au₅Pd₇₀Pt₂₅. The incorporation of small amount of Au increases the ethanol oxidation activity. The electrocatalytic activity of Au₅Pd₉₅ is more than two times higher compared to pure Pd nanoballs and 56% higher compared to Pd₇₅Pt₂₅ nanoballs. Au₅Pd₇₀Pt₂₅ nanoballs give the highest activity for ethanol oxidation reaction compared to other electrocatalysts.

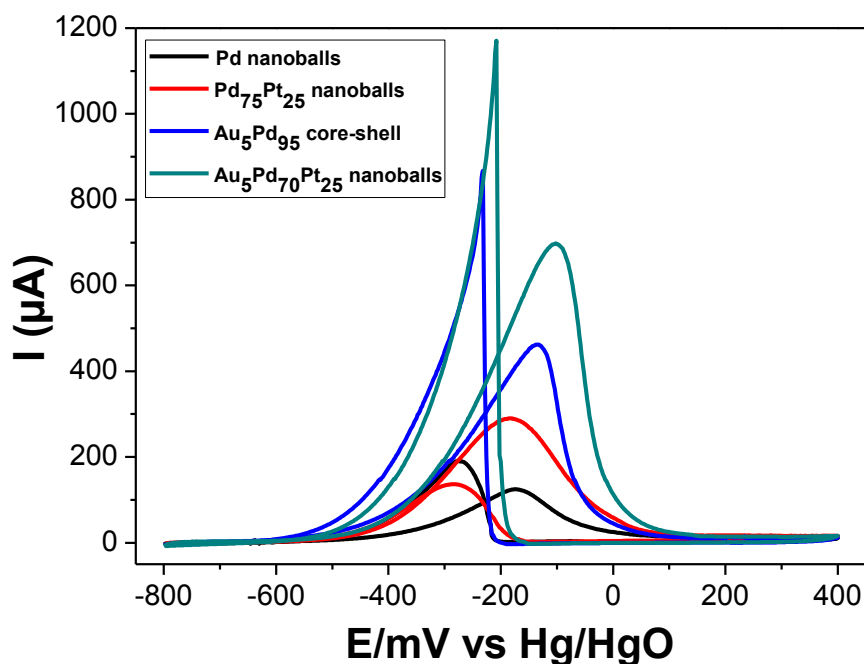


Figure 3.30 Cyclic voltammogram of Pd nanoballs, Pd₇₅Pt₂₅ nanoballs, Au₅Pd₉₅ core-shell (Au@Pd), and Au₅Pd₇₀Pt₂₅ nanoballs in 1 M of KOH + 1M of ethanol at the scan rate of 50 mV/s.

According to **Table 3.9**, the trimetallic of Au₅Pd₇₀Pt₂₅ has the most negative onset potential. The results shown here are still preliminary results. Many experiments are planned to complete this work, such as:

- Optimization of the composition of Au@Pd and Au@Pd core-shell for ethanol oxidation reaction.
- Calculate the electro active surface and current density of each sample
- Perform chronoamperometry experiments to study the stability of each sample with time.

Table 3.9 Onset potential of Pd nanoballs, Pd₇₅Pt₂₅ nanoballs, Au₅Pd₉₅ core-shell, and Au₅Pd₇₀Pt₂₅ nanoballs for ethanol oxidation reaction

Sample	Onset potential (mV)
Pd nanoballs	-533
Pd ₇₅ Pt ₂₅ nanoballs	-575
Au ₅ @Pd ₉₅ core-shell	-580
Au ₅ Pd ₇₀ Pt ₂₅ nanoballs	-586

III.3.3 Application of Au@Pd, Au@Pt, and AuPdPt nanostructures for glucose oxidation reaction

Application of Au@Pd, Au@Pt, and AuPdPt nanostructures for glucose oxidation reaction was investigated in collaboration with Teko Napporn (Université de Poitiers).

Figure 3.31 shows the cyclic voltammograms (CVs) of glassy carbon (red) and Au₁₀@Pt₉₀ in 0.1 mol L⁻¹ NaOH recorded at 20 mV s⁻¹ et at 20 °C. The CV profile obtained for the disk of glassy carbon corresponds to that observed in the literature with a large double layer along the potential range. The CV of Au₁₀@Pt₉₀ shows typically three potential regions: the hydrogen adsorption-desorption region (from 0.05 to 0.43 V), the double layer region followed by the formation and the reduction of the oxides at the nanomaterials surface. In the hydrogen region, two reversible peaks related to hydrogen adsorption and desorption were observed between 0.2 and 0.4 V vs. RHE. The CV profile did not reveal any presence of gold. Probably the gold is not at the surface but in the bulk. Therefore, the present CV profile is close to that of pure platinum.

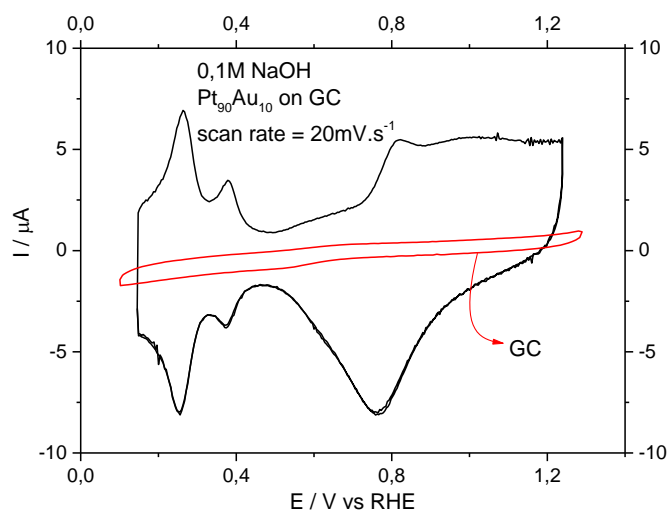


Figure 3.31 Cyclic voltammogram of Au₅Pd₇₀Pt₂₅ nanoballs in 0.1 M of NaOH recorded recorded at the scan rate of 20 mV/s.

CO Stripping

Figure 3.32 shows cyclic voltammogram of CO stripping experiment of Au₁₀@Pt₉₀. The first CV (red): During the positive scan, the oxidation of CO starts around 0.3 V vs. RHE with two pre-peaks followed by the main oxidation peak centred at 0.65 V (**Figure 3.32**). It is well known in the literature the origin of these pre-peaks

which could depend on the experimental conditions, the nature of the electrode, its surface composition and crystallographic orientation, and also the catalysts support which can play a key role. Investigations made by Urchaga et al. have shown that the mechanism of the CO stripping is mostly governed by Eley-Rideal pathway.^{139,140} After the oxidation of CO, the surface of the nanomaterials is oxidized. During the negative potential scan the reduction of the oxides at the electrode surface occurs with the maximum current of about $0.8 \mu\text{A}$ at 0.75 V vs. RHE . The CV obtained after the CO stripping has confirmed the supporting electrolyte and the electrode are free of CO (second cycle in black line).

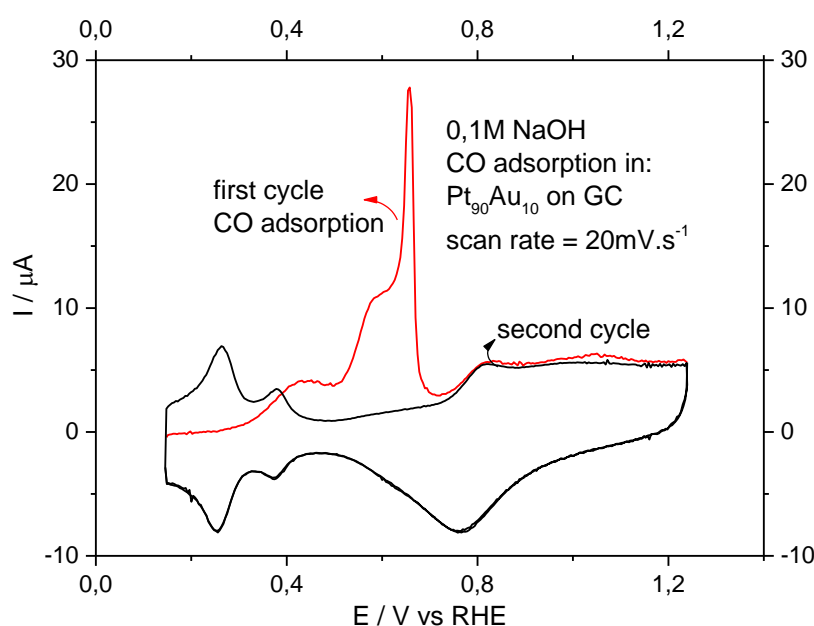


Figure 3.32 CO stripping on $\text{Pt}_{90}\text{Au}_{10}$ in 0.1 mol L^{-1} NaOH recorded at 20 mV s^{-1} and at $20 \text{ }^{\circ}\text{C}$.

Glucose oxidation

The oxidation of glucose was performed on these nanoparticles in the same supporting electrolyte in presence of 10 mmol L^{-1} of glucose (**Figure 3.33**). During the positive potential going, the oxidation of glucose starts before 0.2 V with a first oxidation peak at 0.3 V followed by a second one at 0.7 V vs. RHE . Another oxidation peak was observed around 1.05 V . During the negative potential sweep, two oxidation peaks were observed at 1.05 V and 0.7 V .

According to the literature³, the first oxidation peak observed during the positive scan corresponds to the dehydrogenation of glucose which leads to the formation of

glucono-lactone. The glucono-lactone is transformed to gluconate by hydrolysis. The low oxidation potential observed for glucose at Au₁₀@Pt₉₀ is benefit for the use of this catalyst as electrode material for glucose/oxygen fuel cell.

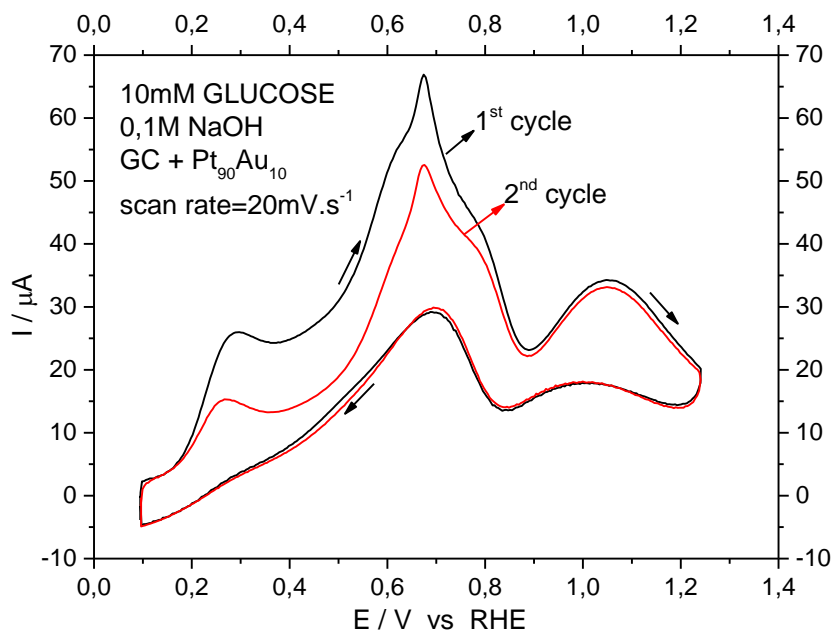


Figure 3.33 Cyclic voltammogram of Pt₉₀Au₁₀ in 0.1 mol L⁻¹ NaOH + 10 mmol L⁻¹ glucose recorded at 20 mV s⁻¹ and at 20 °C .

III.4 Synthesis of PtNi porous nanostructures for H₂ evolution reaction

H₂ is regarded as one of the cleanest fuels, thus it has received a lot of attention from the energy and environmental research community. Pt has been well known as the most active material for H₂ evolution reaction (HER), however, the high price and scarcity of Pt are still the biggest obstacle for hydrogen technology development. Combining Pt with other metals, especially 3d transition metals, such as Fe, Co, Ni, and Cu is expected to improve their electrocatalytic activity, and most importantly reduce the usage of precious Pt. Typically, Pt doping with Ni has been proved among one of the most effective strategy for many important reaction.^{141,142}

III.4.1 Material characterization

Pt₈₅Ni₁₅ porous nanostructures prepared in doped mesophases (with the ratio Pt/Ni=85/15) were synthesized by radiolysis technique with two different source of irradiation: gamma irradiation (low dose rate) and electron beams (high dose rate). The dose rate delivered by the electron accelerator (located in LCP, Orsay) is 720 kGy/h, which is much higher compared to that of gamma irradiation (3.5 kGy/h). The dose rate fixes the reduction kinetics and previous studies have shown that high dose rate induces formation of nanoalloys, while low dose rates often leads to formation of core-shell structures (where the less noble metal is in the core). Therefore, an alloy structure of PtNi is expected through the synthesis by electron accelerator, while a core-shell structure is expected by gamma irradiation.¹² Because of the alloy structure, higher activity could be obtained because a synergetic effect between Pt and Ni.

Figure 3.34 shows TEM images of Pt₈₅Ni₁₅ porous nanostructures synthesized by gamma and electron beams. The samples prepared by gamma rays give nanoballs structures with small core inside (see HRTEM images in **Figure 3.35**), which probably corresponds to Ni core (**Figure 3.34 a and b**). Whereas, porous Pt₈₅Ni₁₅ with more homogeneous shapes were observed for the sample prepared by electron beams (**Figure 3.34 c and d**), and there is no core of Ni observed in this case. We assume that for the sample synthesized by electron beams, there is a formation of Pt₈₅Ni₁₅ alloy nanostructures due to a very high dose rate used during the synthesis. However, HAADF-STEM characterization will be performed to confirm the formation of a PtNi alloy structure.

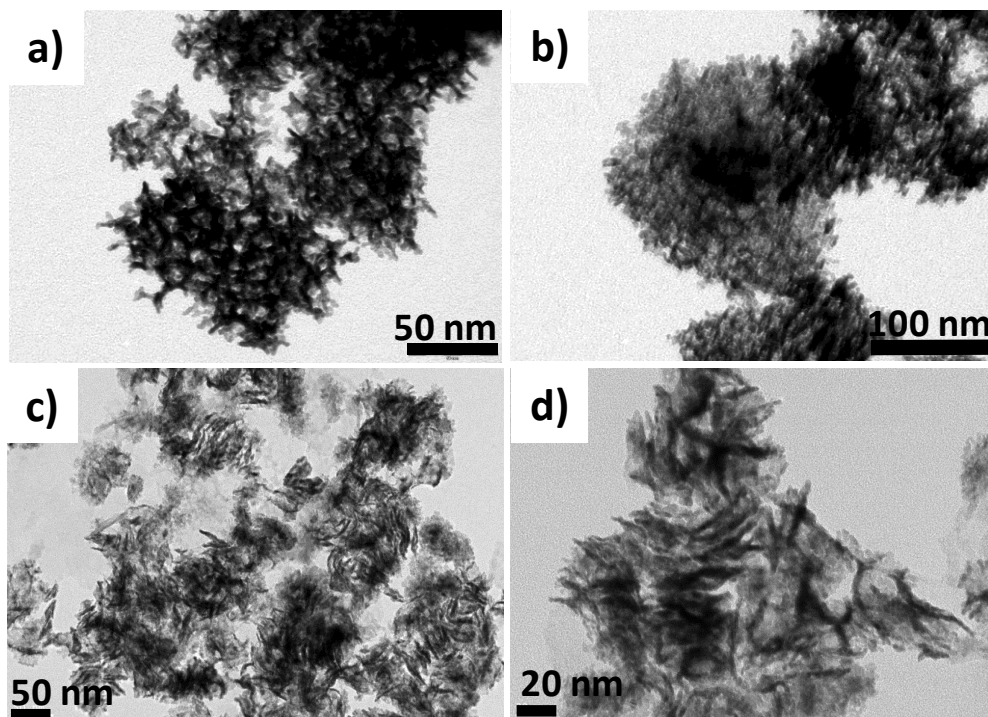


Figure 3.34 TEM images of $Pt_{85}Ni_{15}$ porous nanostructures synthesized by gamma (**a** and **b**) and electron beam (**c** and **d**).

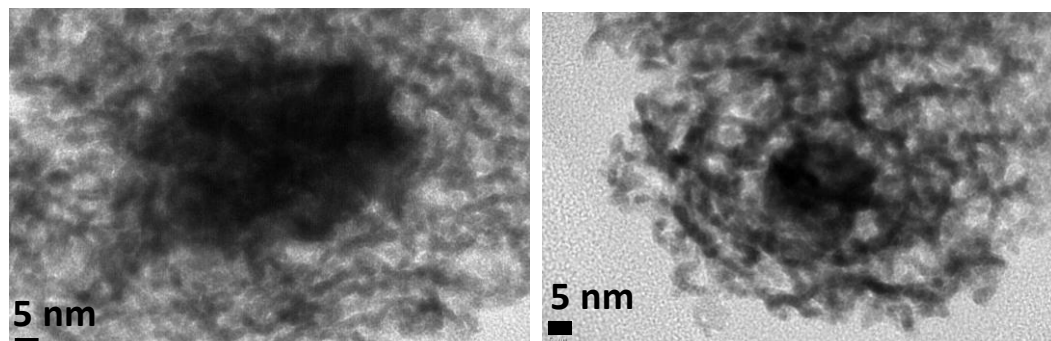


Figure 3.35 HTEM images of $Pt_{85}Ni_{15}$ porous nanostructures (showing a core-shell structure) synthesized by gamma irradiation.

XPS is used to analyze the chemical composition and determine the oxidation states of Ni and Pt in PtNi nanostructures synthesized in mesophases by gamma irradiation and electron accelerator. XPS signals of both samples indicate the presence of both Pt and Ni on the surface of the nanostructures (**Figure 3.36 a and b**). Br (coming from the surfactant CTAB (cetylpyridiniumbromine)) is observed for both samples. Indeed Br^- is strongly adsorbed on the metal surface and is difficult to be removed by

washing. A comparison of Pt4f for both samples is presented in **Figure 3.36c and d**. The peaks with binding energy at 71.38 eV and 74.58 eV are observed in both samples, and are assigned to Pt4f_{7/2} and Pt4f_{5/2}, correspondingly. Those two peaks indicate the presence of metal Pt (Pt0). Other peaks at binding energy of 73.28 eV and 76.48 eV, which correspond to Pt4f_{7/2} and Pt4f_{5/2} are only observed for the sample of Pt₈₅Ni₁₅ synthesized by electron accelerator. Those peaks indicate the presence of PtO in the sample of Pt₈₅Ni₁₅ synthesized by electron beam. Indeed, during irradiation, depending on the source of irradiation, the samples were inserted into two different vessels. PtO observed for sample synthesized by electron beams can be due to the presence of O₂, which was not completely removed by degassing with N₂. These experiments will be repeated.

The Ni2p XPS spectra for both samples are quite similar (**Figure 3.36 e and f**). In both samples, Ni2p_{3/2} peak is identified at 856 eV, which is attributed to the presence of Ni(II) and confirm the presence of NiO. The exposition of samples to air during the drying process may cause the partial oxidation of sample and formation of NiO cluster. XPS results also indicate the presence of Ni(0) in both sample at 852.5 eV.

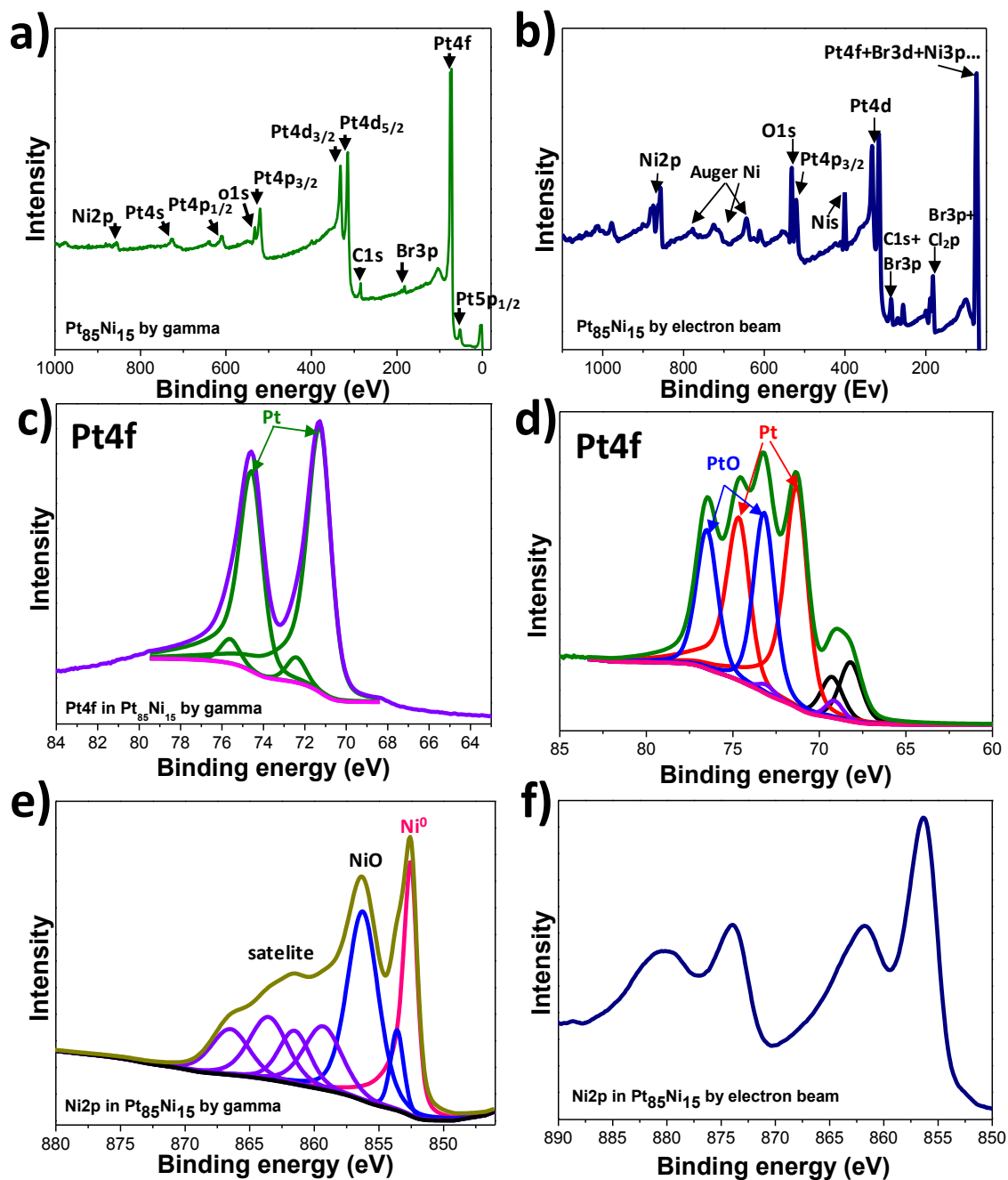


Figure 3.36 XPS spectra of porous $Pt_{85}Ni_{15}$ nanostructures prepared by gamma irradiation (a, c, e) and by electron beam (b, d, f)

III.4.2 Application of PtNi for H_2 evolution

The electrocatalytic activity of porous $Pt_{85}Ni_{15}$ is tested for H_2 evolution reaction. The sample is deposited on glassy carbon electrode and coated with Nafion. The experiment is conducted in 0.05 M of H_2SO_4 . **Figure 3.37** shows cyclic voltammograms of Pt nanoballs, $Pt_{85}Ni_{15}$ synthesized by gamma and electron beams. The electrocatalytic

activity of Pt₈₅Ni₁₅ synthesized by electron beam is almost double of Pt₈₅Ni₁₅ synthesized by gamma irradiation (-227 μA) for Pt₈₅Ni₁₅ synthesized by electron beam and -141 μA for Pt₈₅Ni₁₅ synthesized by gamma irradiation). The difference in activity must be due to the different nanostructures (alloys vs core/shell) or to the presence of Ni oxides. However, the activity of PtNi nanostructures is lower compared to pure Pt nanoballs (-352 μA). Experiments with different Pt/Ni ratios will be conducted to find less expensive electrocatalysts with higher activity.

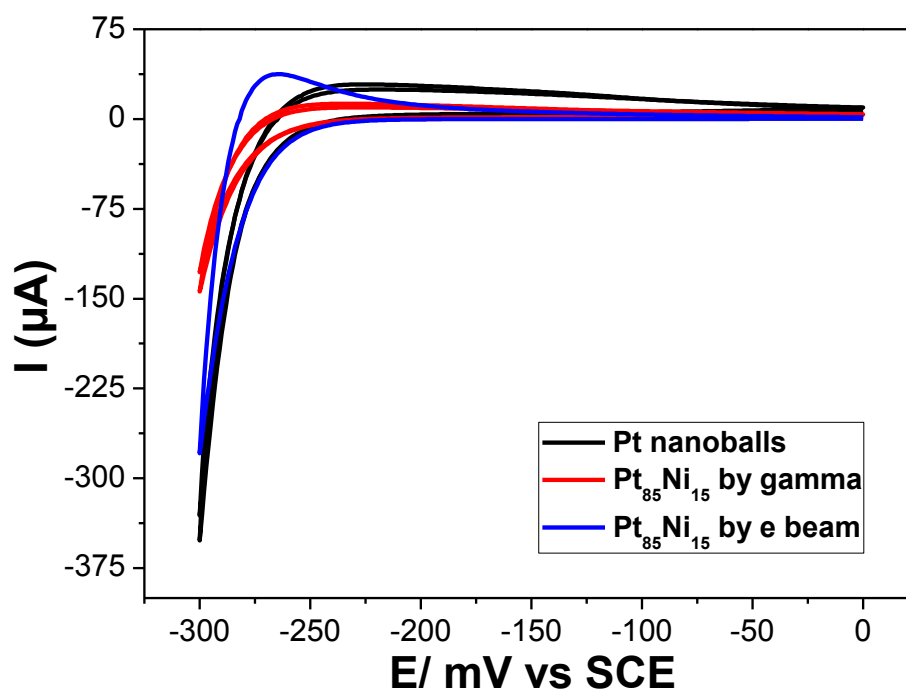


Figure 3.37 Cyclic voltammetry of Pt nanoballs, Pt₈₅Ni₁₅ synthesized by gamma irradiation, and Pt₈₅Ni₁₅ synthesized by electron beam in

III.5 Conclusion

Several metal nanostructures such as PdPt, Au@Pd, Au@Pt, and PtNi nanostructures with controlled of size, composition and structure have been successfully synthesized in the aqueous phase of hexagonal mesophases. These metal nanostructures are very active for several reactions which are usually used in the anodic part of fuel cells.

- **The synthesis of porous PdPt with controlled of pore size and compositions.** Here, the compositions of PdPt were optimized for ethanol oxidation reaction, and PdPt nanostructures with the ratio of 3/1 appear as the best electrocatalyst for this reaction. The pore size of PdPt nanoballs are controlled with the swelling ratio of

O/W in mesophases. The electro active surface as well as the current increase with the pore size.

- **Au@Pd and Au@Pt core-shell and AuPdPt**

These materials were used for ethanol and glucose oxidation reaction. Au₅Pd₇₀Pt₂₅ nanostructures appear as the best electrocatalyst for ethanol oxidation reaction compared to Au₅@Pd₉₅, pure Pd nanoballs, and Pd₇₅Pt₂₅ nanoballs. Other experiments will be conducted to optimize the composition of these bi- and trimetallic nanostructures and to calculate their electro active surface as well as their current density.

- **PtNi porous nanostructures**

PtNi nanostructures were synthesized at different dose rates. A core-shell structure is observed for the sample synthesized by gamma (low dose rate), while probably an alloy structure is obtained by electron beam. Further characterization namely HAADF-STEM and EDS will be performed to better characterize these nanostructures. The activity of Pt₈₅Ni₁₅ nanostructures for H₂ evolution is lower than that of Pt nanoballs.

CHAPTER IV

Conjugated Polymer

Nanostructures Synthesized in

the Oil Phase of Hexagonal

Mesophases for Photocatalysis

under Solar Light

Conjugated Polymer Nanostructures Synthesized in the Oil Phase of Hexagonal Mesophases for Photocatalysis under Solar Light

The term photocatalysis is used to describe a chemical reaction process in which photons are used to activate a substance (catalysts). Photocatalysis is a rapidly developing field of research with a wide industrial and environmental applications, such as self-cleaning surfaces, mineralization of organic pollutants, disinfection of water and air, production of renewable energy resources, and organic synthesis. The abundant, clean, and safe energy of the sun to activate this process makes photocatalysis a suitable, non-hazardous, and economically viable technology to degrade organic pollutants (in water and air) and to produce clean energy through solar fuels.

Titanium dioxide (TiO_2) is the most commonly used semiconductor for photocatalysis because of its good photocatalytic activity, low price, high stability and non-toxicity. However, TiO_2 is only active under UV light irradiation (band gap equal to 3.2 eV for anatase and 3.0 eV for rutile), while solar light consists of only 4% of UV light (Fig. 4.1). Doping of TiO_2 with N, C, S or its surface modification with plasmonic metal nanoparticles (Ag, Au, Pt) to enhance its photocatalytic activity under solar light is therefore a very active field of research.^{57,143–153}

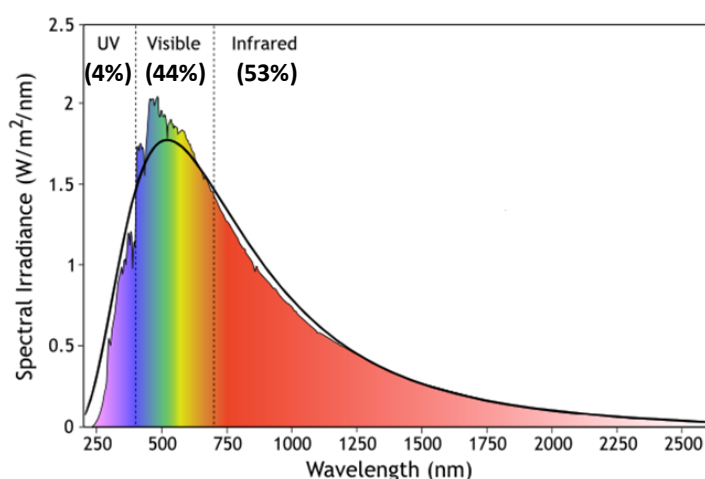


Figure 4.1 Solar radiation spectrum.¹⁵⁴

With the discovery of conductive polyacetylene in 1978, conjugated polymers (CPs) have received significant interest from both scientific and engineering communities.¹⁵⁵ The combination between the superior electronic properties of semiconductors (such as high conductivity, mechanical and thermal stability) and the advantages of organic materials (low cost and easy processing) render CPs promising materials for a variety of opto-electronic applications such as solar cells, light emitting diode, field-effect transistors, etc.^{156–161}

Recently, our research team has shown that conjugated polymers (in particular Polydiphenylbutadiyne) (PDPB) and Poly(3,4-ethylenedioxythiophene (PEDOT)) emerge as a new class of photocatalysts very active under visible light.^{58,162} In this context, we have shown that the nanostructuring of PDPB and PEDOT polymers, thanks to their synthesis in soft templates formed by hexagonal mesophases, leads to an enhancement of their photocatalytic activity.^{58,162}

Here, we extend our work to study the photocatalytic activity of poly(3-hexylthiophene) (P3HT) nanostructures. P3HT is a widely used conjugated polymer for photovoltaic applications. Synthesis of P3HT nanostructures in hexagonal mesophases, their photocatalytic application for water treatment, study of the photocatalytic mechanism, and the enhancement of the photocatalytic activity after deposition on a solid support will be discussed.

This chapter is divided into 4 parts: introduction, theoretical background, and synthesis and application of conjugated polymer P3HT nanostructures for water depollution (synthesis, characterization, photocatalytic application and mechanism).

IV.1 Theoretical background and bibliography

IV.1.1 Heterogeneous photocatalysis

Photocatalytic reactions can occur either homogeneously or heterogeneously. In homogeneous photocatalysis, the reactants and the photocatalysts exist in the same phase, while in heterogeneous photocatalysis, the reactants and photocatalysts are in different phases. However, heterogeneous photocatalysts are more extensively studied due to their easy separation and reutilization process rendering heterogeneous photocatalysts more favorable for large scale of applications.

The process of heterogeneous photocatalysis can be performed in various media such as gas phase, pure organic liquid phases or aqueous solutions. As for classical heterogeneous catalysis, the overall process can be decomposed into five independent steps:¹⁶³

1. Transfer of the reactants in the fluid phase to the surface
2. Adsorption of a least one of the reactants on the surface?
3. Reaction in the adsorbed phase
4. Desorption of the product(s)
5. Removal of the products from the interface region

The photocatalytic reaction occurs in the adsorbed phase (Step 3). The only difference with conventional catalysis is the mode of activation of the catalyst in which the thermal activation is replaced by a photonic activation. The activation mode is not concerned with steps 1, 2, 4 and 5, although photoadsorption and photodesorption of reactants, mainly oxygen, do exist.

The term heterogeneous photocatalysts is mainly used in cases where a light absorbing semiconductor photocatalysts is used, which is in contact with either a liquid or a gas phases.

IV.1.2 Photocatalytic process

Photocatalysis is a light-driven chemical process over the surface of a photocatalysts that can degrade organic pollutants (**Figure 4.2a**), reduce CO₂ or split water into H₂ and O₂ (**Figure 4.2b**) When a semiconductor absorbs a photon with an energy equal or larger than its band gap, the electron at the valence band will be excited to the conduction band, leading to electron-hole pairs. A large part of electron and holes recombine. When they escape recombination, they can react with molecules present at the surface of the photocatalyst. In the presence of O₂, the generated electrons (e⁻) can react with oxygen to lead to the oxidative superoxide radical O₂^{-•}, while the OH⁻ react with holes and produce HO[•] radical (**Figure 4.2b**). On the contrary, in the absence of O₂, the electron electrons (e⁻) react with H⁺ to lead H₂ (**Figure 4.2b**) (a co-catalyst generally required in this process).

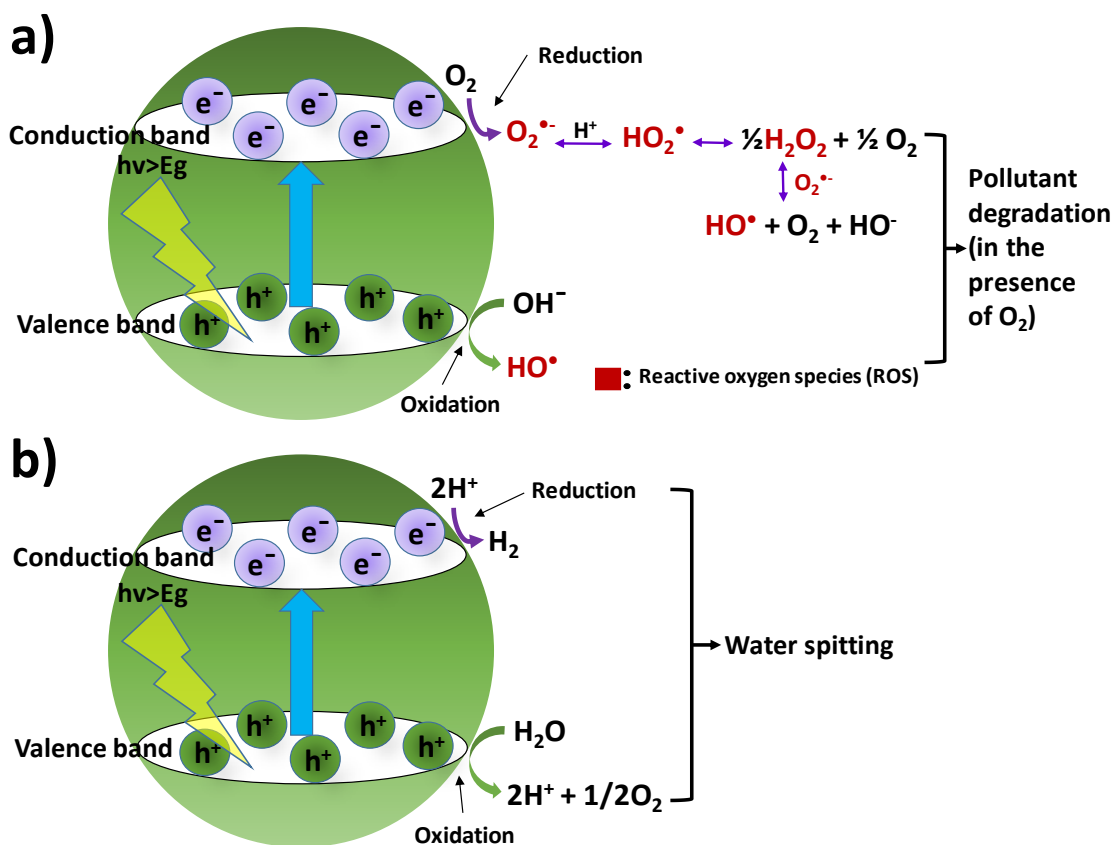


Figure 4.2 Photocatalytic mechanism of pollutant degradation (a) and water splitting (b).

IV.1.3 Conjugated polymers

In chemistry, a conjugated system consists of a structure, which presents connected π -orbitals with delocalized electrons.¹⁶⁴ Based on this, conjugated polymers are organic macromolecules whose structure is characterized by a backbone of alternating single and multiple bonds with overlapping π -orbitals, which results in a system of delocalized electrons.¹⁶⁵ The chemical structures of several conjugated polymers are presented in **Figure 4.3**.

Traditionally, polymers are known as very good electrical insulators, and most of their applications had relied on their insulating properties.¹⁶⁶ However, around 1960-1970, Weiss and co-workers showed that certain classes of polymers such as polypyrrole and polyaniline exhibit signs of conductivity.¹⁶⁷ This was then followed by Shirakawa and co-workers, who demonstrated that the addition of chlorine, bromine, or iodine to polyacetylene films resulted in a highly conductive (doped) materials.¹⁶⁸ This discovery

has initiated number of researches in the field of conducting polymer, and has brought Shirakawa and co-workers to get the Nobel prize award in Chemistry in 2000.

Compared to inorganic materials, where the structure and properties at molecular level are more difficult to adjust, we can more easily tune the physicochemical properties of conjugated polymers by their molecular design.¹⁶⁹

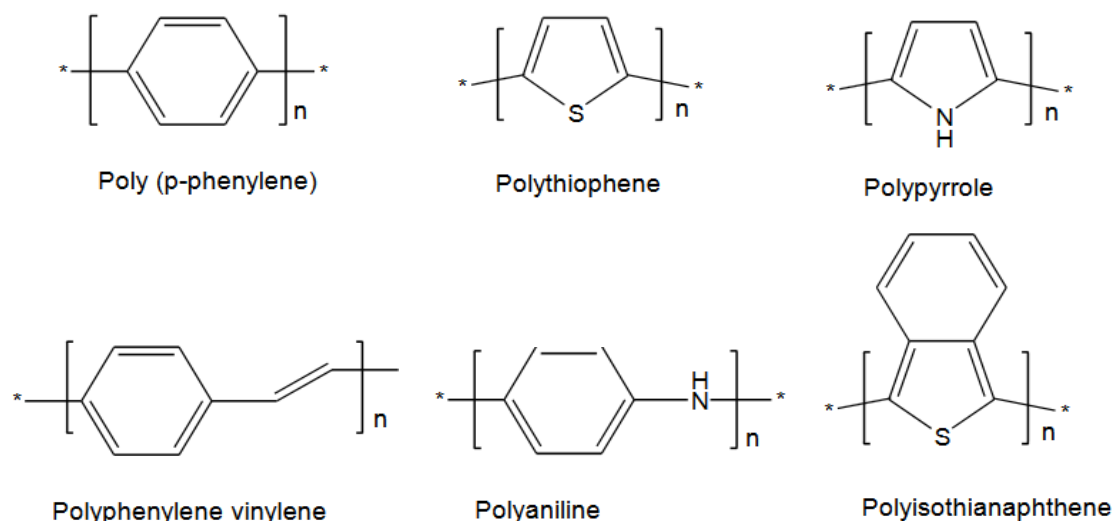


Figure 4.3 Typical (shown uncharged) structures of conjugated polymer

In conjugated polymer, electrons are able to move from one end of the polymer to the other through the extended p-orbital system.¹⁷⁰ Hence conjugated polymers are known to be either semiconductors or conductors, which are related to how bands and shells of electrons form within a compound. The band theory is employed to explain the mechanism of conduction in conjugated polymer. The theory originates from the formation of energy bands in polymer materials from discrete orbital energy levels found in single atom systems.¹⁷¹

The band theory

The chemical approach to band theory is to relate it to molecular orbital theory. In molecular orbital theory, using $H_{(1)}$ and $H_{(2)}$ hydrogen atoms as an example (**Figure 4.4**), an atomic molecular orbital from $H_{(1)}$ atom can overlap with an atomic molecular orbital of $H_{(2)}$ atom, resulting in the formation of two molecular orbitals known as the bonding and antibonding molecular orbitals.¹⁷² These are delocalized over both atoms,

and the bonding molecular orbital possess a lower energy than the $H_{(1)}$ and $H_{(2)}$ atomic orbital, while the antibonding molecular orbital has a higher energy.

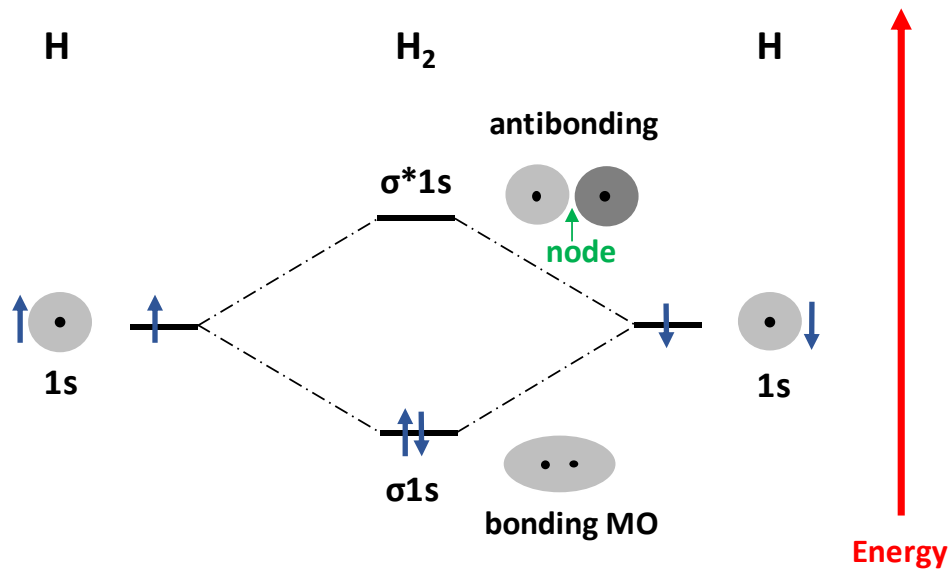


Figure 4.4 Molecular orbital in diatomic molecule.

The energy band that results from the bonding orbitals of a molecule is known as the valence band (VB), while the conduction band (CB) is as a result of the antibonding orbitals of the molecule as illustrated in **Figure 4.4**. The width of individual bands across the range of energy levels is called band width. VB represents the highest occupied molecular orbital (HOMO) and CB represents the lowest unoccupied molecular orbital (LUMO).¹⁷³ The gap between the highest filled energy level and lowest unfilled energy level is called band gap (E_g). The band gap of semiconducting materials is between 0.1 - 3.2 eV. **Figure 4.5** presents the band diagram of insulating, semiconducting, and conducting materials. In conjugated polymers, the value of the band gap depends on the extend of delocalization and the alternation of double and single bonds.¹⁷³

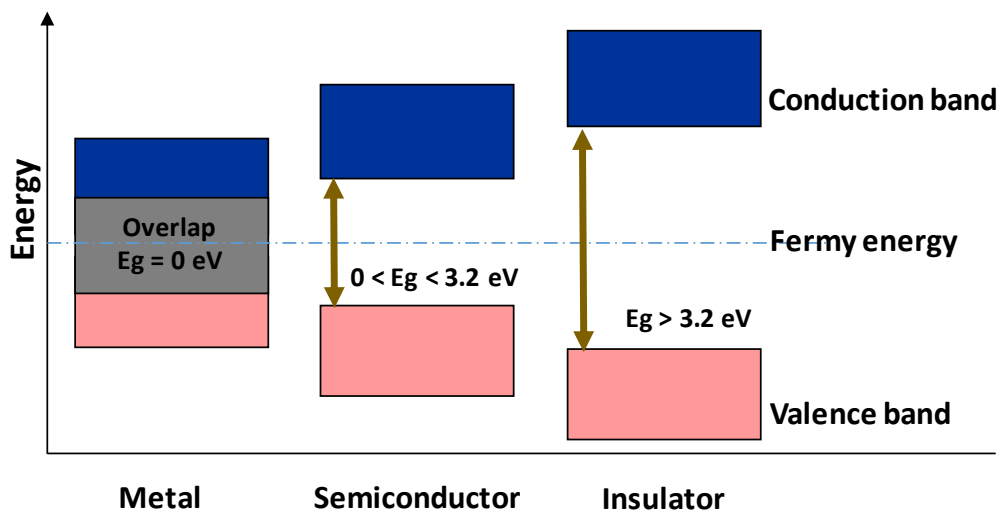


Figure 4.5 Energy band diagram demonstrating band gaps (Fermi level is the term used to describe the top of the collection of electron energy levels at absolute zero temperature).

IV.1.4 The importance of nanostructuring of conjugated polymers for photocatalytic application

A significant change in several physicochemical properties of conjugated polymer nanostructures has been observed compared to their bulk counterpart.^{46,162} Conjugated polymer nanostructures exhibit high conductivity, stability, high surface area, unique optoelectronic properties, flexibility, and processibility.^{174,175}

Previous works by H. Remita and coworkers have reported for the first time photocatalytic activity of conjugated polymer nanostructures under visible light for application in depollution.^{46,119,162} They have shown that nanostructuring of conjugated polymer PDPB is a key factor in photocatalysis application. PDPB (Polydiphenylbutadiyne) nanofibers (synthesized in soft templates) showed high photocatalytic activity for methyl orange (MO) and phenol degradation under visible light, while the bulk PDPB (synthesized without soft templates) showed no activity (**Figure 6**).⁴⁶ This activity under visible light was much higher than plasmonic TiO₂ (titania modified with Ag nanoparticles). The difference in photocatalytic activity between nano and bulk PDPB is due to larger size (providing lower surface to volume ratio) and the presence of more defects in bulk PDPB favoring higher e⁻-h⁺ recombination. The dependence of photocatalytic activity on the size of photocatalysts has been also observed in the case of TiO₂.^{176,177}

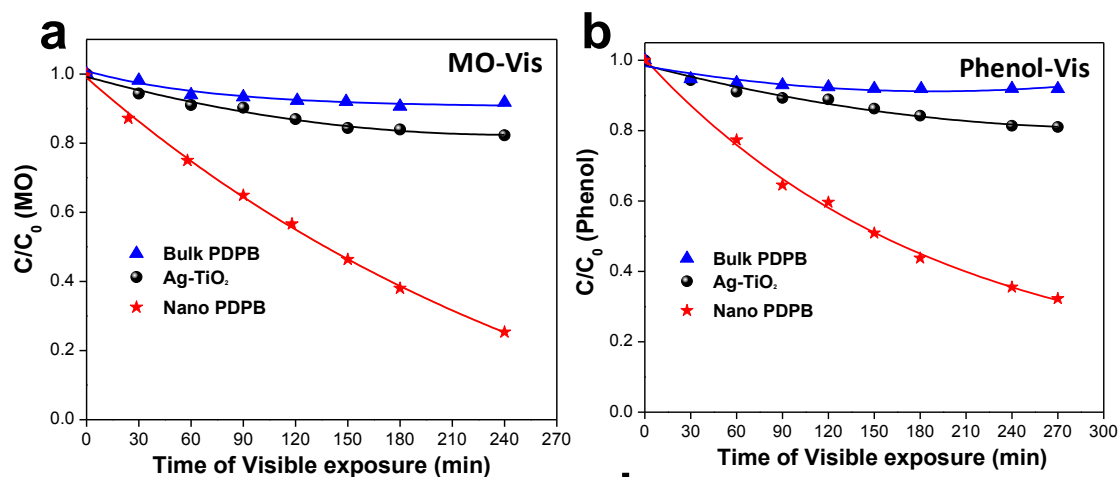


Figure 4.6 Photocatalytic degradation of (a) methyl orange and (b) phenol in the presence of commercial P25 TiO₂ and Ag-TiO₂, and of the synthesized bulk PDPB and nano PDPB, under visible light ($\lambda > 450$ nm). The concentrations of nano PDPB, Ag-TiO₂ and TiO₂ in water were 1 mgmL⁻¹. Initial concentrations C₀ were 6×10^{-5} mol L⁻¹ for MO and 3.7×10^{-3} mol L⁻¹ for phenol.⁴⁶

Not only the size but also the shape of a photocatalyst is important. Other conjugated polymer, Poly(3,4-ethylenedioxythiophene) (PEDOT), has been successfully synthesized in soft template hexagonal mesophases by chemical polymerization process using oxidant FeCl₃ by H. Remita's group. Depending on the conditions of the polymerization, different shapes of PEDOT nanostructures such as spindles (with the thickness of 40 nm and the length about several hundred nanometers) and vesicles (diameter around 1 μ m) can be formed.⁴⁷ Interestingly, PEDOT nanospindles showed a very high photocatalytic activity for methyl orange (MO) and phenol degradation, both under UV and visible light. Whereas, PEDOT vesicles are less active under UV light and even have almost no activity under visible light for MO and phenol degradation (**Figure 4.7**).⁵⁴

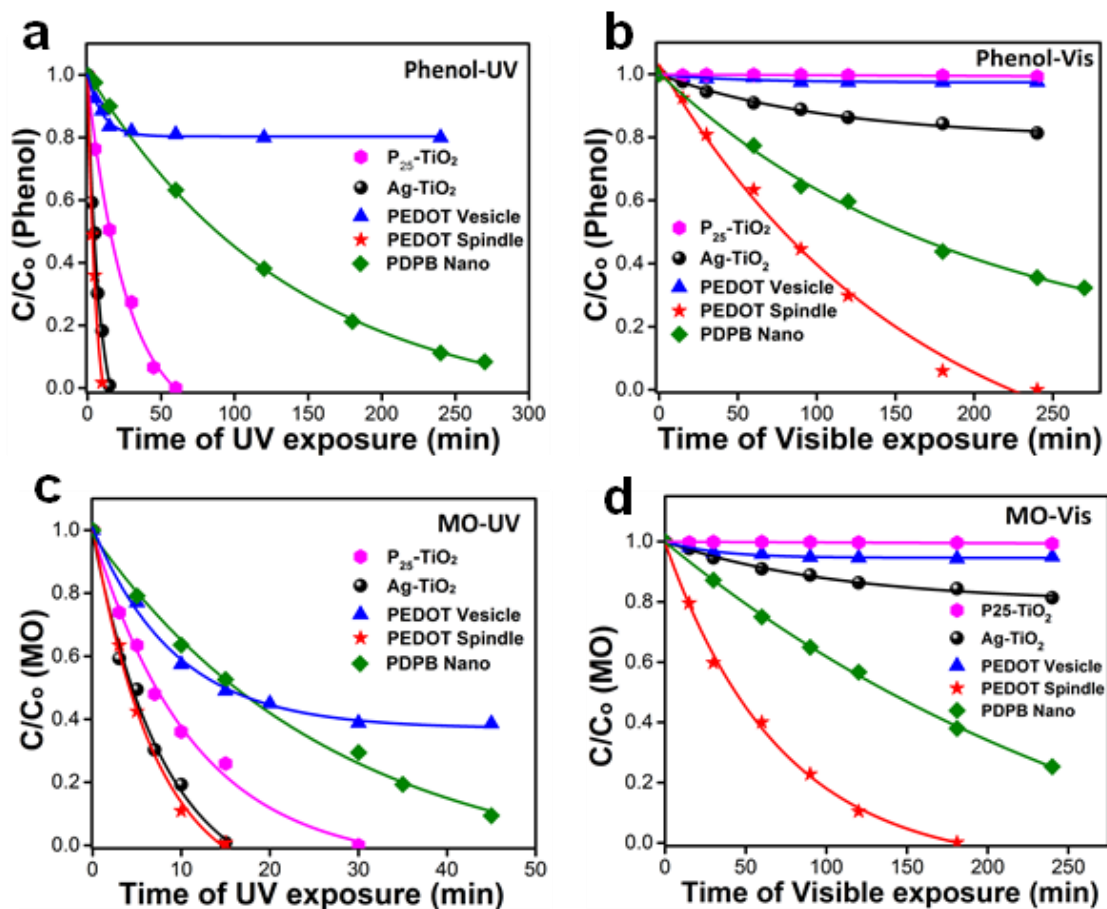


Figure 4.7 Photocatalytic degradation of (a, b) phenol and (c, d) methyl orange (MO) in the presence of commercial P25 TiO₂ and Ag-TiO₂, PDPB nanofibers and the synthesized PEDOT vesicles and PEDOT nanospindles under UV (a, c) and visible light ($\lambda > 450$ nm) (b, d) irradiation.⁵⁴

IV.2 Synthesis and application of conjugated polymer poly (3-hexylthiophene) for pollutant degradation under visible light

There are several important issues that need to be addressed in the field of heterogeneous photocatalysis. The first one is to develop semiconductors, which are active under visible light. The second one is to enhance the quantum yield of light conversion by decreasing the charge carrier (electrons and holes) recombination. As already been mentioned in the general introduction, TiO₂, a widely used semiconductor in photocatalysis, is only active under UV light, which accounts for only 4% of the total solar light.

In application, to avoid filtration difficulties, an immobilization of the photocatalyst is necessary. For application of titania in air and water depollution, many works have focused on the deposition and immobilization of TiO₂ on different supports such as glass beads or plates, on a non-woven glass fiber fabric, steel, or on porous materials, avoiding the separation step of the titania powder. Whatever the support, the immobilization of titania lowers in general its photoactivity because of the difficulty for the UV photons to reach a part of the solid.¹⁷⁸

Conjugated polymer (CP) materials for photocatalysis have been a very hot topic field of research since the last decade. CPs combine the properties of organic materials (low cost and easy processing) and the properties of semiconductor materials (such as high conductivity, mechanical and thermal stability).¹⁵⁶⁻¹⁶¹

Among conductive conjugated polymers, poly(alkylthiophenes) have emerged as one of the most popular class. Poly(3-hexylthiophene) (P3HT) is an organic semiconductor that has been mainly used for the fabrication of transistors, photovoltaic cells, strain sensors, and light emitting devices. P3HT appears to be the most commonly used CPs in organic photovoltaics because of its desirable electronic properties.¹⁷⁹ The incorporation of P3HT into other semiconductors such as TiO₂ or Bi₂MoO₆ has led to the improvement of the photocatalytic activity.^{180,181}

Here, we show for the first time that nanostructures of P3HT are also highly efficient for the degradation of pollutants under UV and visible light. These photocatalysts, which are very stable with cycling, can furthermore, be easily deposited on a flat solid support (quartz or glass) for photocatalytic application. Interestingly, we measure a much faster kinetics for the degradation of pollutant once P3HT nanostructures are deposited on a solid surface.

IV.2.1 Material characterizations

The hexagonal mesophases are characterized by small angle X-ray scattering (SAXS). **Figure 4.8** shows SAXS of mesophases containing monomer 3HT (which was transparent), mesophases containing FeCl₃, and mesophases containing P3HT and FeCl₃. The positions of the first 3 peaks are in the ratio of 1, $\sqrt{3}$, and 2, characteristic peaks of hexagonal mesophases.

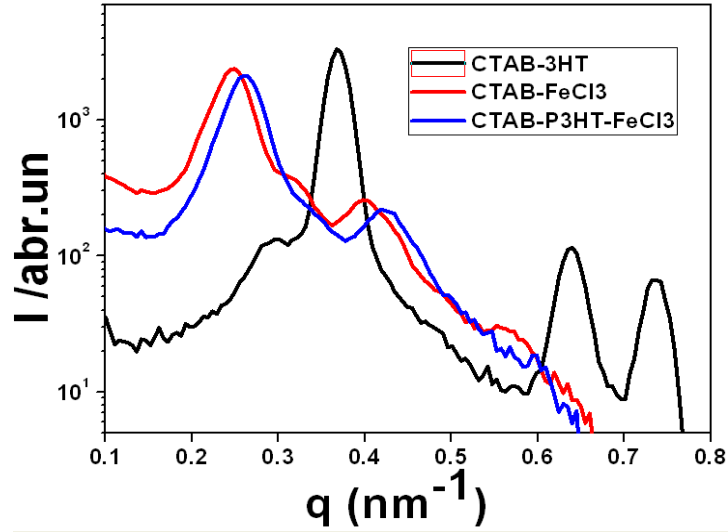


Figure 4.8 Small Angle X-Ray Scattering (SAXS) of 3 different mesophases: Mesophases containing monomer 3HT, mesophases containing FeCl₃, mesophases containing P3HT and FeCl₃.

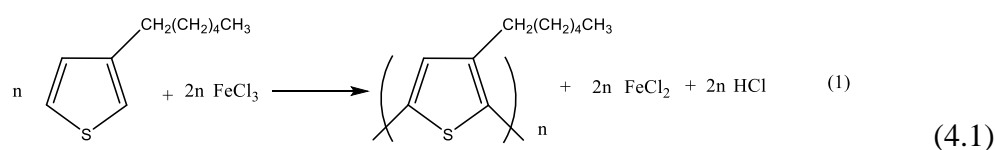
The position of the first peak (q_0) can directly correlate to the lattice parameter (d_c) as define by the equation $d_c = \frac{2}{\sqrt{3}} \frac{2\pi}{q_0}$. One can futher relate the lattice parameter to the tube diameter (D), where $D = 2d_c \sqrt{\left(\frac{\sqrt{3}}{2\pi}(1 - \phi_p)\right)}$. Data are presented in Table 4.1.

Table 4.1 Diameter of oil tube of hexagonal mesophases as measured by the position of the first 3 peaks in SAXS ($q_0, q_1, q_2 =$ position of the first, second, and third peak).

Sample	1 st peak		2 nd peak		3 rd peak		D (nm)
	$q_0(\text{nm}^{-1})$	q_0/q_0	$q_1(\text{nm}^{-1})$	q_1/q_0	$q_2(\text{nm}^{-1})$	q_2/q_0	
CTAB-3HT	0.37	1	0.64	1.7297	0.74	2	19.6
CTAB-FeCl ₃	0.244	1	0.4	1.64	1.967	1.967	29.7
CTAB-P3HT-FeCl ₃	0.264	1	0.424	1.606	1.897	1.897	27.4

Swollen hexagonal mesophases are used as templates for the synthesis of P3HT nanostructures. These mesophases are composed of oil-swollen surfactant tubes arranged on a triangular lattice in water. The hydrophobic domain of the mesophases can

accommodate high concentrations (up to 0.1 M) of 3HT monomer, which is polymerized by oxidation with FeCl₃ according to Reaction (4.1):



Here, polymerization proceeds inside the confined oil tubes (toluene phase) of diameter ≈ 27 nm (according to SAXS in **Table 4.1**). Hexagonal mesophases containing only monomers are colorless (**Figure 4.9**), transparent and birefringent, while the mesophases containing FeCl₃ are also translucent and birefringent, but yellow, because of the absorption properties of FeCl₃. The oxidant (FeCl₃) and monomer (3HT) are dispersed in separate volumes of toluene, in order to avoid polymerization prior to mesophase formation.

Once incorporated sequentially in the mesophase, the color of the mixture turns first into green-brown, and then orange upon continuous vortex (**Figure 4.9b**). The as-prepared P3HT structures can be easily extracted from the mesophases by simple washing with ethanol, followed by centrifugation (insert a of **Figure 4.9c**). After drying an orange solid powder of P3HT is obtained (Inset b of **Figure 4.9c**).

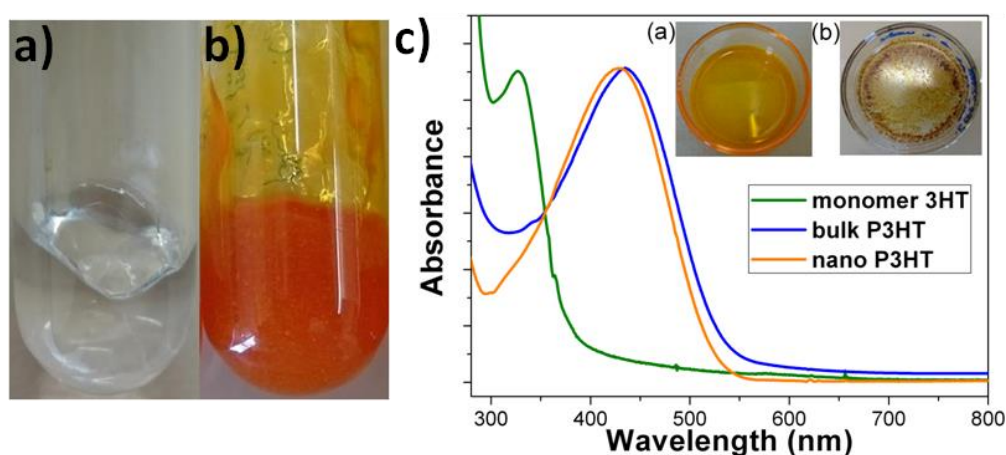
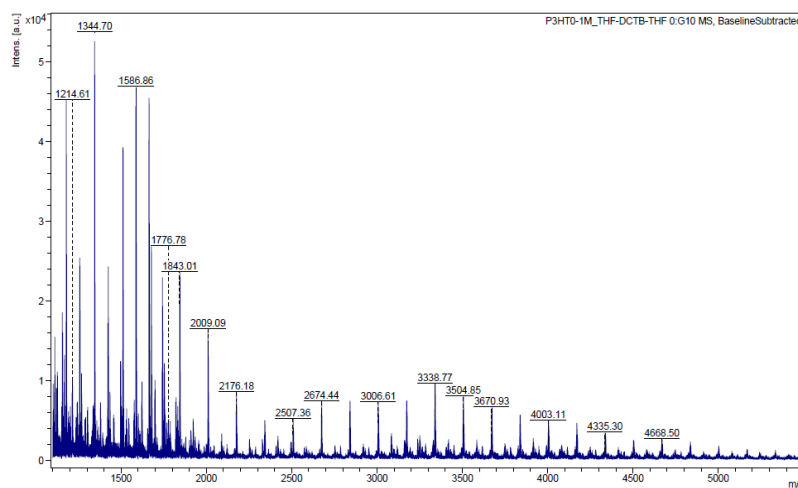
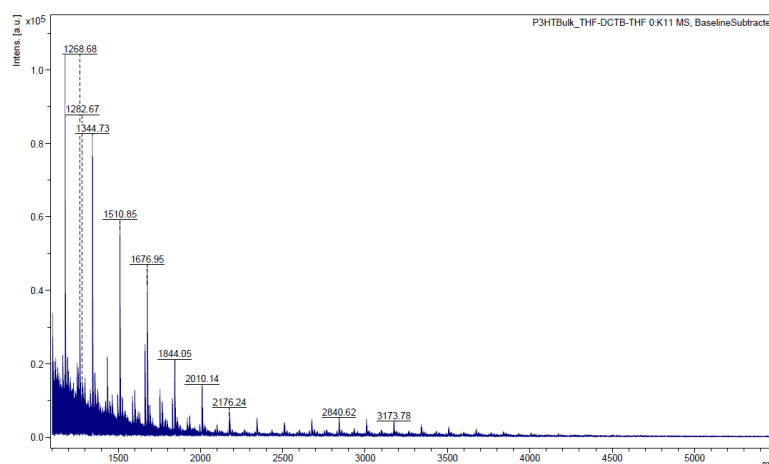


Fig 4.9 Pictures of hexagonal mesophases doped with (a) 3HT monomer and (b) P3HT polymer; (c) Normalized UV-Visible spectra of the 3HT monomer, nano P3HT, and bulk P3HT in chloroform, **Inset:** Pictures of nano P3HT extracted in ethanol (a) and after drying (b).

Figure 4.9c shows the UV–vis absorption spectra of the 3HT monomers and that of P3HT polymer structures (synthesized with and without mesophases, denoted respectively as nano P3HT and bulk P3HT). The 3HT monomer exhibits an absorption peak at 329 nm. After polymerization, the peak at 329 nm disappears, and a new peak around 428 nm for nano P3HT and 435 nm for bulk P3HT appears, which indicates the complete polymerization of P3HT. The absorption is due to the $\pi - \pi^*$ interband transition. The optical bandgap can be estimated from the absorption edge as equal to 550 nm (2.25 eV). The maximum molecular weight of nano P3HT, as determined by Maldi-TOF (Matrix Assisted Laser Desorption/Ionization Time of Flight) mass spectroscopy, is found to be 4668 g mol⁻¹ which corresponds to about 28 repeated units of 3HT monomers (**Figure 4-10**).



(a)



(b)

Figure 4.10. Maldi-TOF mass spectra of nano (a) and bulk (b) P3HT.

Figure 4.11 shows attenuated total reflectance Fourier transform infrared spectroscopy (ATR-FTIR) spectra of the monomer 3HT, and of nano and bulk P3HT. The spectra of nano and bulk P3HT are similar, although their absorption bands are slightly shifted, and in good agreement with the literature.¹⁸² Three peaks are observed in the interval (3000–2850) cm^{-1} for all samples. These peaks are characteristic of C–H bonds on the hexyl side chain, and are assigned respectively to the asymmetric C–H stretching vibrations of CH_3 (2956 cm^{-1}) and CH_2 - (2920 cm^{-1}) moieties, as well as the symmetric C–H stretching vibration in CH_2 - (2850 cm^{-1}) moieties. The peak around (1454–1460) cm^{-1} (found also for all samples) is associated with a symmetric C–C ring stretching vibration. In the fingerprint region, the IR absorption peaks for 3HT monomer at 766 cm^{-1} and 832 cm^{-1} are ascribed to the C–H out-of-plane stretching vibration of the 2,5-substituted thiophene ring. These peaks are no longer observed for nano and bulk P3HT, which confirms the quantitative polymerization of the thiophene monomers. The peaks at 627 and 678 cm^{-1} are associated to the absorption of C–S–C bonds of the thiophene ring. The characteristic in-plane and out-of-plane rocking vibration of $-(\text{CH}_2)_n$ -group can also be observed at (716–720) cm^{-1} .

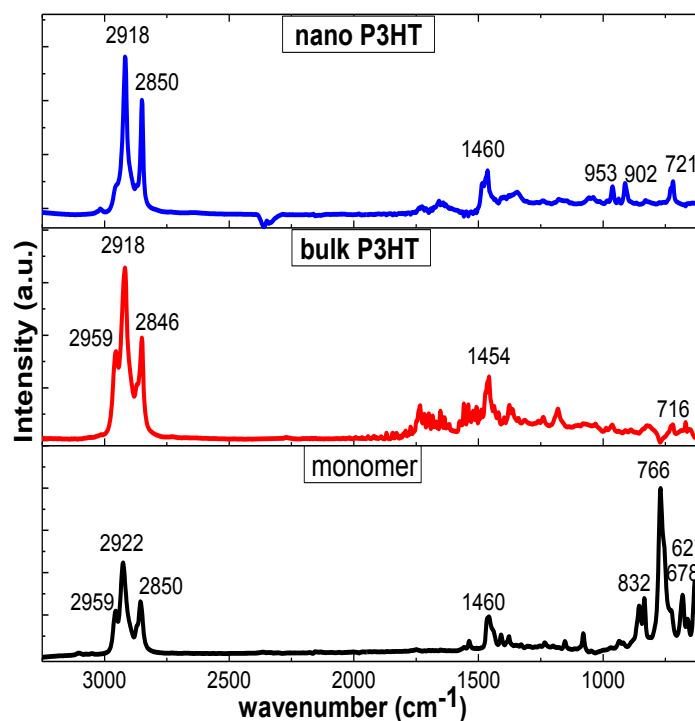


Figure 4.11 ATR-FTIR spectra of the 3HT monomers and of nano P3HT and bulk P3HT polymers.

Transmission Electron Microscopy (TEM) images (**Figure 4.12**) show that bulk P3HT forms large aggregates of several hundred nanometers. By contrast, the polymer nanostructures synthesized in hexagonal mesophases are constituted of connected nanowires of diameter about 30 nm. Note that the diameter of the P3HT nanowires corresponds to the diameter of the cylinder of the hexagonal mesophase determined by SAXS (see **Figure 4.8** and **Table 4.1**) attesting the templating effect of the soft mould.

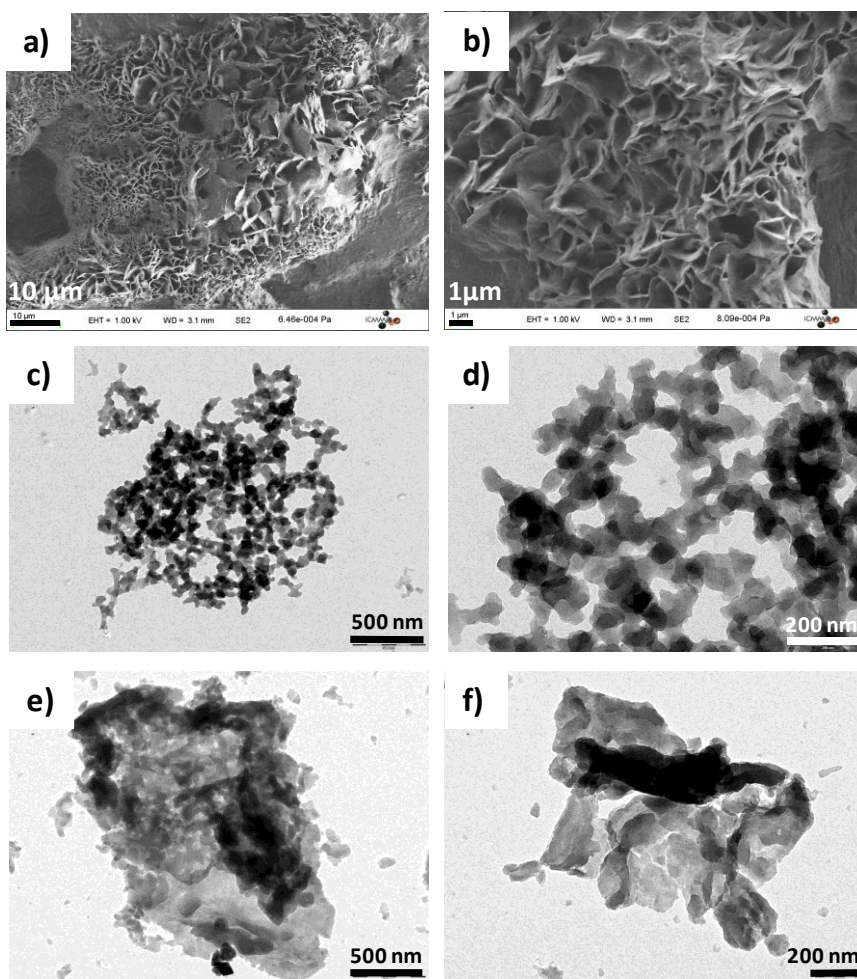


Figure 4.12 SEM images of nano P3HT dispersed in ethanol (**a and b**); TEM images of nano P3HT (**c and d**) (in mesophases) and bulk P3HT (**e and f**) (without mesophases)

Atomic Force Microscopy combined with infrared spectroscopy (AFMIR) allows concomitant investigation of the surface topography and chemical structure. The surface topography of P3HT synthesized in hexagonal mesophases highlights the presence of elongated like structures while P3HT synthesized in bulk solution shows large plates

(around 10 μm size), which were probably formed by aggregation of smaller particles on the ZnSe substrate during deposition (**Figure 4.13 a, d**).

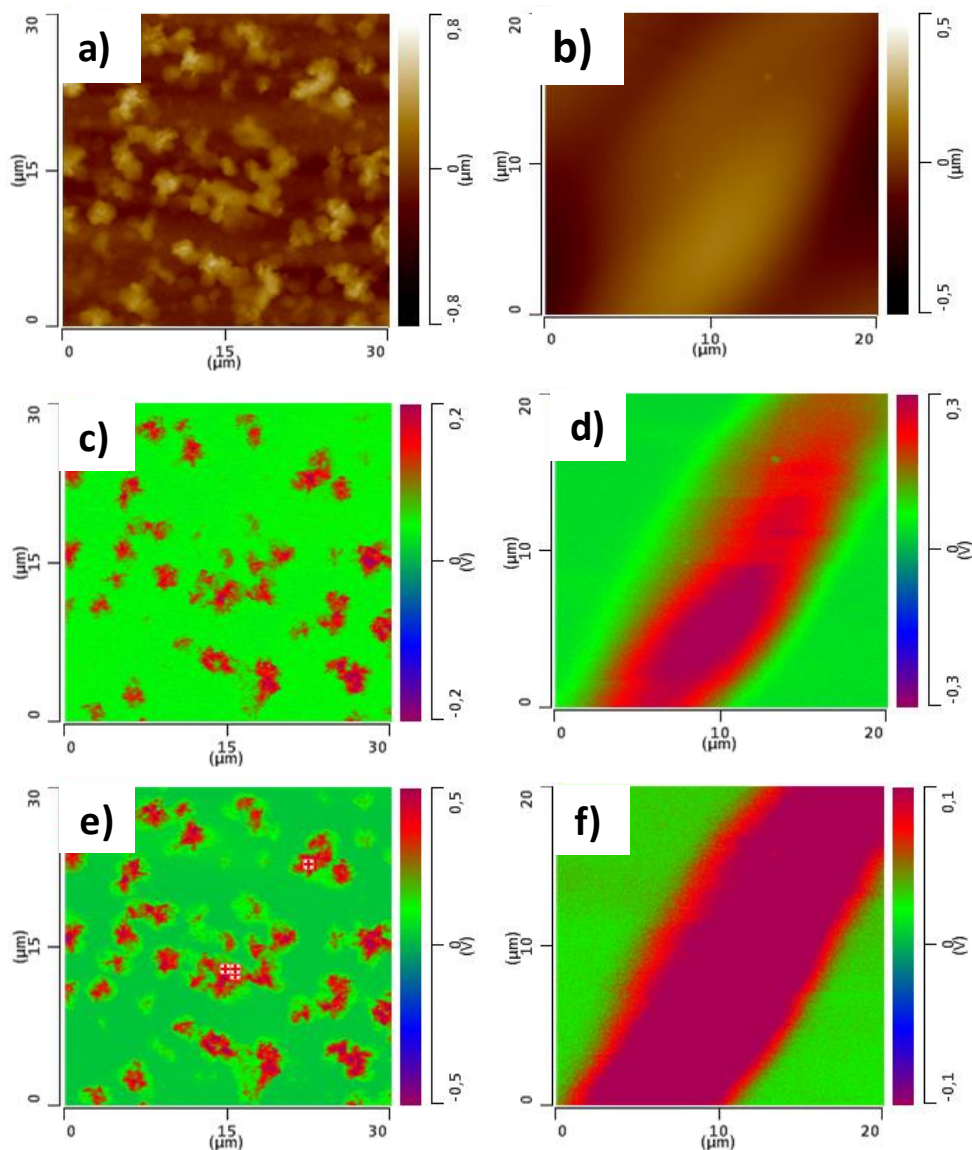


Figure 4.13 AFM topography for nano P3HT (**a**) and bulk P3HT (**b**), chemical mapping at 1456 cm^{-1} for nano (**c**) and bulk (**d**) P3HT, chemical mapping at 2928 cm^{-1} for nano (**e**), and bulk (**f**) P3HT.

IV.2.2 Photocatalytic tests

The photocatalytic activity of P3HT is evaluated for water depollution. Phenol is chosen as a model pollutant, as it has long been proposed as standard test molecule.¹⁸³ Prior to any photocatalytic tests, dark adsorption tests of bulk P3HT and nano P3HT are

performed, by putting into contact the polymer samples with the model pollutants in the absence of irradiation. In this case, no adsorption is observed on the polymer structures. The photocatalytic activity of bulk and nano P3HT was evaluated by measuring the decomposition rate of phenol in water under both UV–vis (xenon lamp) and visible light (using a long pass filter $\lambda \geq 400$ nm) (**Figure 4.14**).

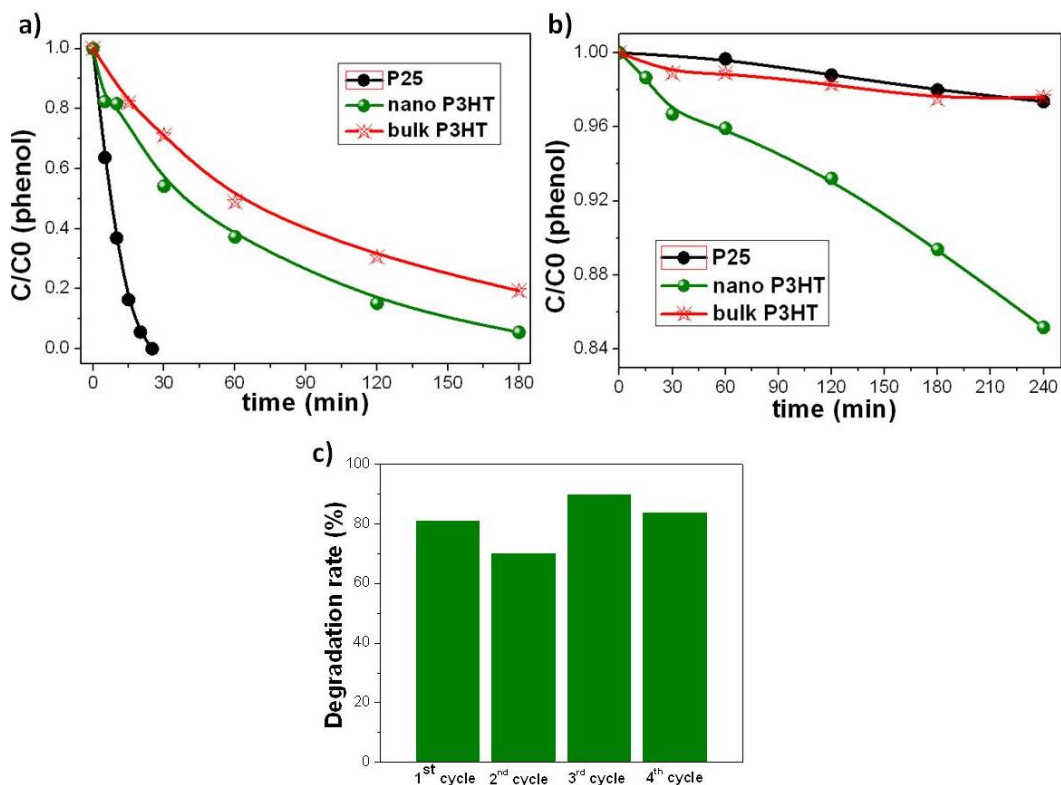


Figure 4.14 Photocatalytic tests of P3HT (in suspension) under UV-visible (a) and visible light ($\lambda > 400$ nm) (b) for the degradation of phenol in water solution; (c) Photocatalytic degradation rate of phenol using nano P3HT up to 4 cycles after 180 minutes irradiation under UV-visible light irradiation.

For applications, it is important to obtain stable photocatalysts. Therefore, the stability of P3HT nanostructures with cycling is investigated (**Figure 4.14c**). We find that the photocatalytic activity is very stable up to 4 cycles, suggesting that P3HT nanostructures could be efficiently reused after repeated cycles.

The photocatalytic activities of bulk P3HT and nano P3HT are compared to that of commercial TiO_2 , P25 (which is very active under UV light) and to that of nanofibers of PDPB, which have been reported recently.⁵⁸ Nano P3HT demonstrates a good photocatalytic activity for phenol degradation under UV–vis light: a 25% degradation is

reached after 15 min, while with bulk P3HT 13%, degradation is achieved after the same irradiation time (**Figure 4.14a**). This activity is higher than that of PDPB nanofibers under UV light (but much lower than that of P25) (see **Figure 4.15**).

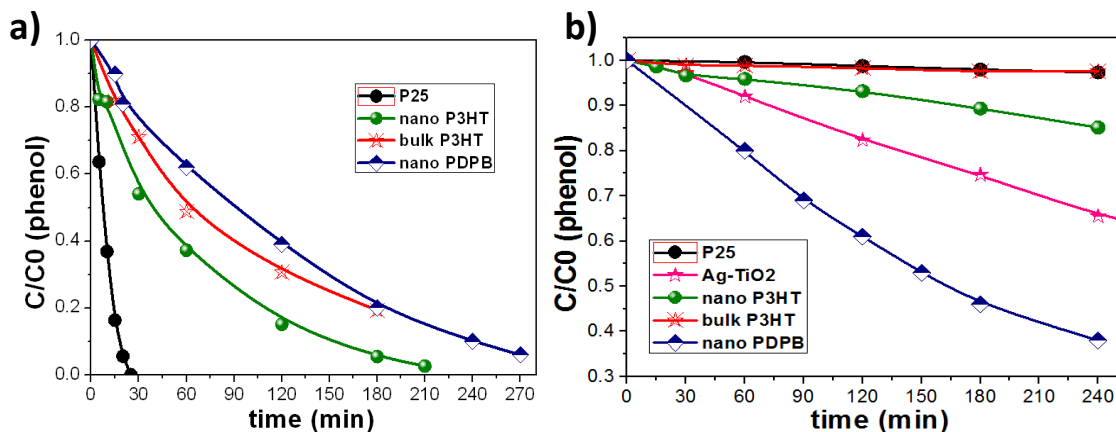


Figure 4.15 Photocatalytic test of TiO_2 (P25), nano P3HT, bulk P3HT, and nano PDPB under UV-visible (**a**) and visible (**b**) light irradiation.

The total mineralization of phenol is followed using as a common technique, the disappearance of the total organic carbon (TOC) for expressing the detoxification level of water. The P3HT nanostructures were able to fully oxidize the organic pollutant, with an almost complete mineralization of carbon into CO_2 and H_2O . Indeed, TOC measurements indicate about 87% of mineralization of phenol after 240 min under UV light. These results suggest that the conducting polymer nanostructures are able to mineralize organic pollutants.

Interestingly, under visible light, nano P3HT still exhibits a high photocatalytic activity, higher than that of bulk P3HT: 16% photo degradation of phenol is achieved after a 240 min irradiation with nano P3HT, while only 3% degradation is obtained with bulk P3HT (**Figure 4.14b**). Nevertheless, this activity is lower than that of Ag-TiO₂ and PDPB under visible light (see **Figure 4.15b**). Other photocatalytic tests conducted with Rhodamine B also show high photocatalytic activity of the P3HT nanostructures under UV and visible light (see **Figure 4.16**).

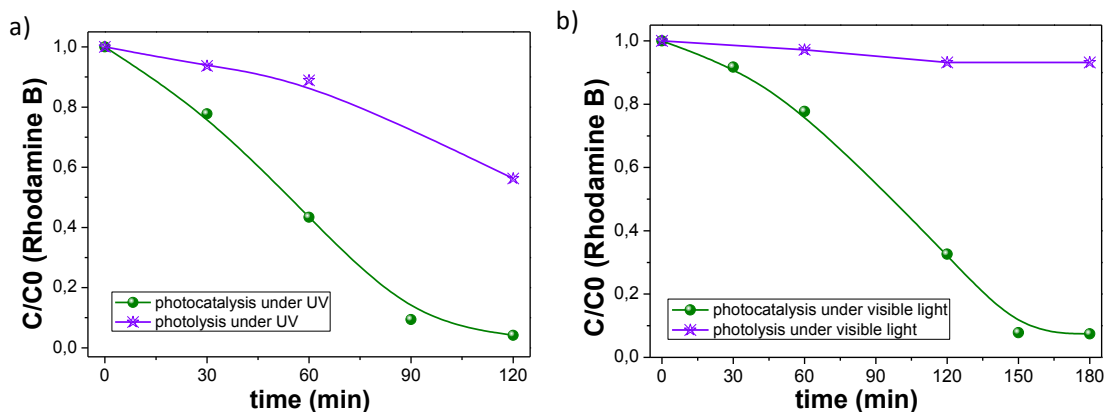


Figure 4.16 Photocatalytic degradation of Rhodamine B using nano P3HT and its photolysis (blank experiments without the photocatalyst): **a-** under UV-visible light, and **b-** under visible light ($\lambda > 400$ nm).

The difference in the photocatalytic activity between nano and bulk conjugated polymer nanostructures have already been reported for other conjugated polymers (PDPB and PEDOT) and have been assigned to the presence of more defects in bulk polymers favoring higher electron-hole recombination.^{58,162}

In order to understand the origin of the photocatalytic activity of P3HT nanostructures under UV and visible light, it is necessary to investigate their electronic properties. The oxidation and reduction potentials of bulk and nano P3HT are determined under similar experimental conditions to estimate, using cyclic voltammetry (CV) measurements, both the energy level of the highest occupied molecular orbital (HOMO) and the energy of lowest unoccupied molecular orbital (LUMO) from the ionization potential and the electronic affinity, respectively, as well as the band gap. We find that the main p-doping (oxidation) process occurs at onset potentials of +0.79 V (bulk P3HT) and +0.81 V (nano P3HT) while n-doping starts at -1.82 V (bulk P3HT) and -1.76 V (nano P3HT) yielding an electrochemical gap $E_{\text{gap elec.}} = 2.61$ eV (bulk P3HT) and 2.57 eV (nano P3HT) in a first approximation as shown in **Figure 4.17**. Further, a careful look at CV may give hints to explain the differences between the photocatalytic properties of nano P3HT and bulk P3HT, especially in the p-doping part. Indeed, a very small current can be recorded between -0.1 V to 0.5 V with an onset at around 0.095 V vs Ag before the main onset oxidation for nano P3HT. Upon p-dedoping process, a reverse behavior (small negative current) is also observed in the same potential window. This effective

redox system (see arrow in **Figure 4.17a**) is typical of the presence of structural defects hence creating interband/microstates energetic levels. As a matter of fact, at the vicinity of these defects, the bandgap is much lower and the HOMO level is raised (see **Figure 4.17**). The low bandgap implies the possibility of a more efficient injection of carriers, potentially useful for applications in optoelectronics or electrocatalysis. Such interband levels have already been observed in the case of PDPB.⁵⁸

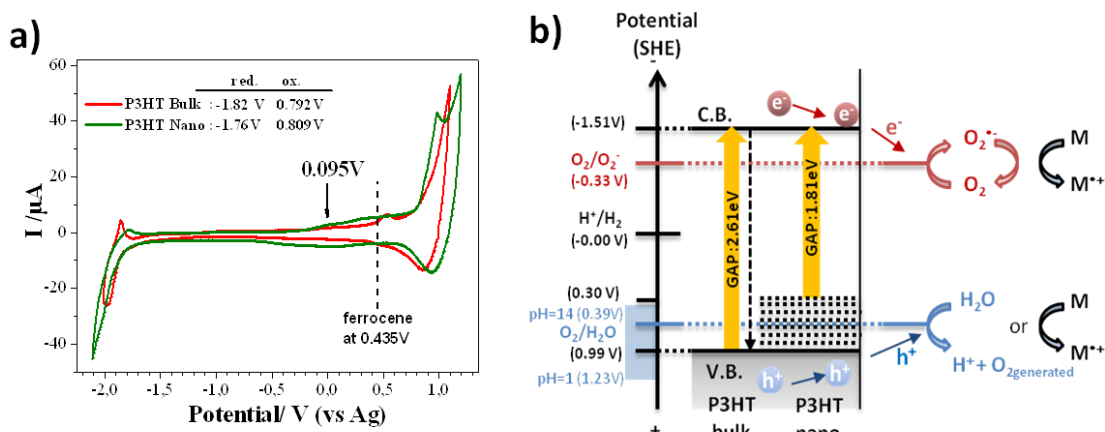


Fig 4.17 (a) Cyclic voltammetry of bulk (red curve) and nano P3HT (green curve) recorded at 20 mV/s in acetonitrile and 0.1M TBAPF₆. Ferrocenium/ferrocene (Fc⁺/Fc) redox potential has been measured at the end of each experiment in order to calibrate the pseudo reference electrode (0.435V vs. Ag in the present study). The HOMO/LUMO energetic levels of P3HT are determined as follows: E_{HOMO} (eV) from ionization potential = $-4.8-e$ ($E_{ox_onset}-0.435$) and E_{LUMO} (eV) from electronic affinity = $-4.8-e$ ($E_{red_onset}-0.435$). **(b)** Possible photocatalytic mechanism with charge separation in nano and bulk P3HT with both electron reducing oxygen and hole oxidizing water. Consequently, the holes and generated oxidative radicals can oxidize organic pollutants (noted as M). O₂ generated at the valence band level (V.B.) can contribute to the O₂ reduction at the conduction band level (C.B.).

IV.2.3 Photocatalytic mechanism

Light irradiation of P3HT with photons of energy exceeding (or equal to) the band gap ($E \geq 2.6$ eV or $\lambda \leq 477$ nm) induces the formation of excitons and charge carriers. Their relaxation generates luminescence. The absorption and emission properties of P3HT as well as the dynamics of the excited states and charges have already been studied,

both in solution and in films, mainly for regioregular P3HT.^{184–188} We find that nano P3HT presents fluorescent properties, but the emission spectrum depends on the excitation wavelength (**Figure 4.18 a**). For excitation above 400 nm the dependence is weak as the emission spectrum exhibits a similar broad structureless band with a maximum slightly shifted from 563 ($\lambda_{exc} = 400$ nm) to 561 nm ($\lambda_{exc} = 450$ nm). By contrast, for excitation below 400 nm, the emission spectrum changes more drastically as a shoulder appears around 480 nm, which suggests the presence of another emissive state. That is confirmed by the excitation spectra registered at different wavelengths (**Figure 4.18 b**). Indeed, the excitation spectra obtained for the main emission band peaking around 560 nm are alike presenting a broad band with a maximum around 400 nm and resemble the absorption spectrum. In contrast, the excitation spectrum related to the emission at 475 nm differs significantly: it is structured with a maximum at ~ 340 nm and two features at ~ 370 and ~ 430 nm, revealing the existence of higher energy excited states that do not relax entirely to the lowest emissive states. Consequently, excitation in the UV domain (below 380 nm) does not generate the same excited states as the excitation in the visible part, which may account for different photocatalytic activities under UV and visible light. A detailed study of the excited states and charge carriers is under progress.

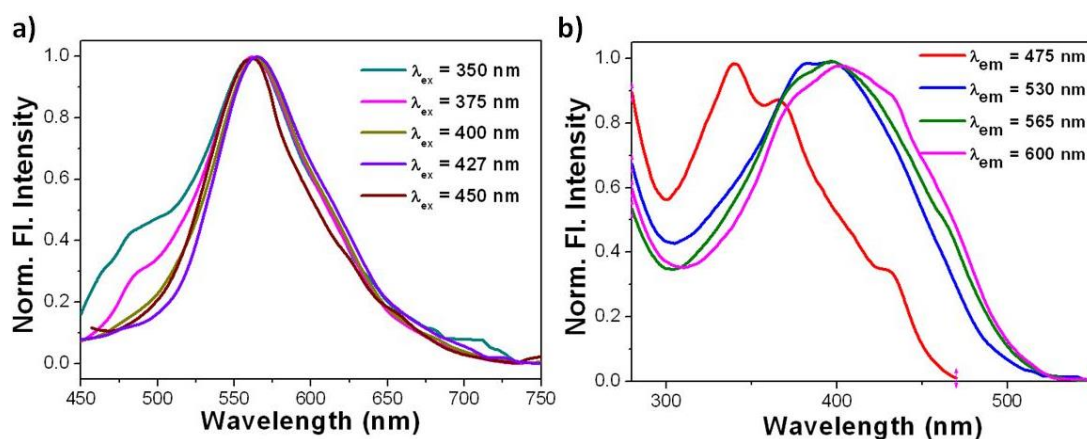
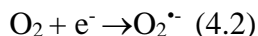
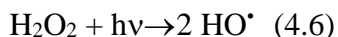


Figure 4.18 Normalized emission (a) and excitation (b) spectra of nano P3HT in chloroform.

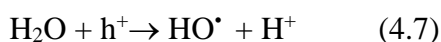
When electrons and holes escape from recombination, they can migrate to the surface and react with oxygen, water or other molecules at the interface. Electrons react with oxygen to form the oxidizing $O_2^{\cdot-}$ superoxide radical ($E^0(O_2/O_2^{\cdot-}) = -0.33$ V_{SHE}):



However, $\text{O}_2^{\bullet-}$ is very reactive radical and can oxidize molecules and transform into HO^{\bullet} through the following reactions:



While in HOMO level, the holes might react with HO^- (or H_2O) to yield oxidative HO^{\bullet} radicals:



In order to identify the species that are responsible for photodegradation activity of nano P3HT, experiments were carried out with Cu^{2+} and 2-propanol as electrons and holes scavengers, respectively. Data show that the presence of Cu^{2+} slows down the degradation kinetics (**Figure 4.19**). Cu^{2+} reacts with electrons to yield Cu^+ , and this reaction is in competition with reaction (2). The presence of Cu^{2+} causes a decrease in the production of $\text{O}_2^{\bullet-}$ in the photocatalytic system, which leads to a decrease in the degradation kinetics. The photodegradation efficiency of phenol is reduced from 94% to 40% in the presence of 0.01 M of Cu^{2+} after 3 h under UV-vis light irradiation (see Fig. 4.19).

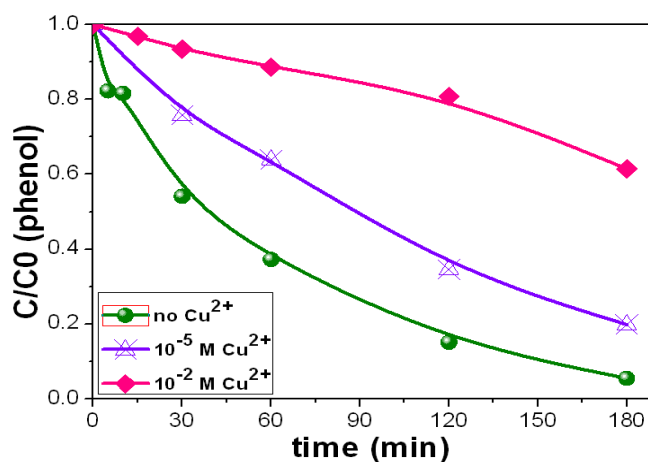


Figure 4.19 Photocatalytic degradation of phenol using nano P3HT in the presence or not of Cu^{2+} (at different concentrations) as electron scavenger.

In addition, in the absence of O_2 , the activity of P3HT for phenol degradation decreases from 95% to 30% after 3 h UV-vis irradiation (**Figure 4.20**).

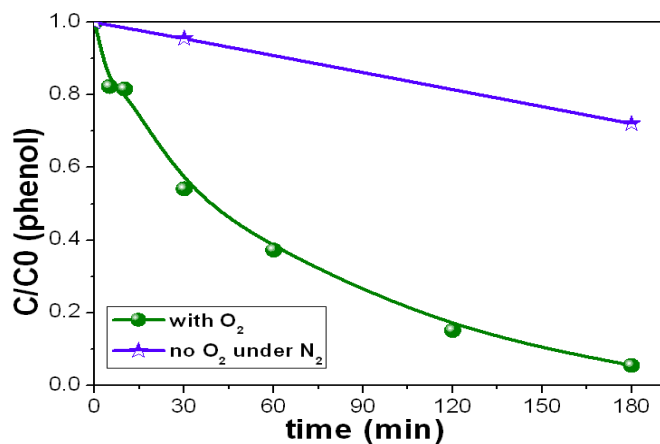


Figure 4.20 Photocatalytic phenol degradation using nano P3HT with and without O_2 .

Furthermore, experiments have been conducted in the presence of 2-propanol known to scavenge the holes and HO^\bullet radicals very efficiently. The experiments conducted in the presence of O_2 and 2-propanol do not show any decrease in photocatalytic degradation of phenol (**Figure 4.21**). According to the HOMO level of P3HT, the reaction between the holes and H_2O is not thermodynamically favorable.

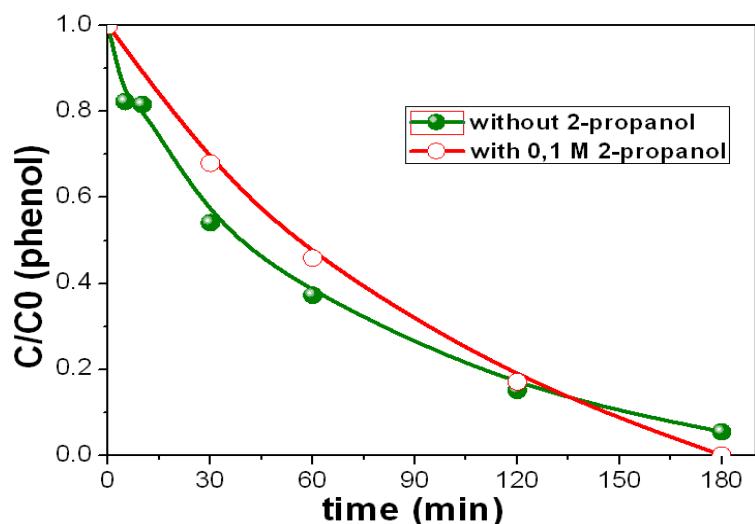


Figure 4.21 Photocatalytic test using nano P3HT in the presence of 2-propanol as a hole scavenger.

Additional experiments are conducted with other scavengers: Benzoquinone and tert-butanol are used as $O_2^{\cdot-}$ (superoxide radical) and HO^{\cdot} scavengers, respectively. Fig. V.14 shows that the presence of tert-butanol as HO^{\cdot} radical scavenger does not inhibit the photocatalytic activity of P3HT for phenol degradation, while the photocatalytic tests conducted with benzoquinone show no degradation of phenol. All these experiments prove that photodegradation of phenol by P3HT is mainly caused by $O_2^{\cdot-}$ superoxide radical formed from the reduction of oxygen (O_2) or generated oxygen (O_2 generated).

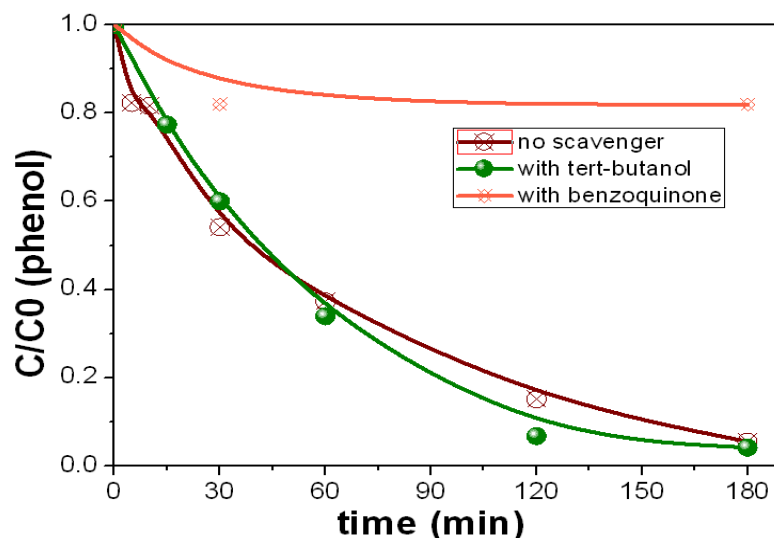


Figure 4.22 Photocatalytic test using nano P3HT in the presence of benzoquinone and tert-butanol as $O_2^{\cdot-}$ and HO^{\cdot} radical scavengers, respectively.

Moreover, a remarkable result is that phenol degradation is faster with nano P3HT than with bulk P3HT (**Figure 4.14 a and b**). Several phenomena could explain those results. First, the nanometric size is expected to induce an increase of the specific surface area, which involves degradation reactions. Second, higher electron-hole recombination is expected to occur in bulk P3HT because of higher volume and higher number of defects. Finally, the presence of microstates above the HOMO level for nano P3HT, as observed in CV measurements, is certainly crucial. Indeed, under illumination, the holes can react more easily with water to form oxygen with microstate energy levels close to $E_0(H_2O/O_2)$.

A possible mechanism for the oxidation of organic pollutants is proposed based on the band gap structure of P3HT and on the experiments with scavengers. **Figure 5b** summarizes the charge carrier generation under irradiation and formation of ROS

(Reactive Oxygen Species) (HO^\bullet and $\text{O}_2^{\bullet-}$) responsible for the oxidation and degradation of the pollutants. These results confirm that $\text{O}_2^{\bullet-}$ is the main involved radical in the photocatalytic mechanism with P3HT (**Figure. 4.17 b**).

IV.2.4 Deposition of nano P3HT on a support for photocatalytic application

Because of its chemical structure, P3HT is very hydrophobic. Hence, P3HT nanostructures aggregate in water, resulting in a loss of surface area. Therefore, the photocatalytic tests in water suspensions containing phenol are not optimized, and explain the high uncertainties (10%) obtained with degradation tests (see for example **Figure 4.14**). On the other hand, for practical applications, it is important to avoid the separation step of the powder in suspension and to develop deposition of the photocatalytic material on solid supports such as quartz slides, glass, fabric fibers, etc. **Figure 4.23 a** and **b** show Scanning Electron Microscopy (SEM) images of the P3HT nanostructures on quartz slides. When deposited on a flat support, the nanostructures self-assemble upon chloroform (used as solvent) evaporation because of London interactions between the non-polar carbon chains and π - π stacking between the polarizable aromatic rings to form large plates forming flowers. **Figure 4.23c** shows a suspension of P3HT nanostructures in a quartz cell containing an aqueous solution with phenol and **Figure 4.23d** shows a quartz slide coated with nano P3HT inside a quartz cell containing a phenol solution irradiated with visible light. Photocatalytic tests are performed with P3HT deposited on quartz slides from a suspension in chloroform. **Figure 4.23 e** shows that phenol degradation kinetics is highly accelerated with deposited P3HT nanostructures. This is the first time that conjugated polymer nanostructures are deposited on a support for photocatalytic applications. This result shows that the photocatalytic activity can be much enhanced with the supported conjugated polymers photo-catalysts (contrary to what it is generally obtained with deposited TiO_2)¹⁷⁸ and opens new perspectives for applications because no separation step is required. Optimization of the deposition of the CP on different supports is under study.

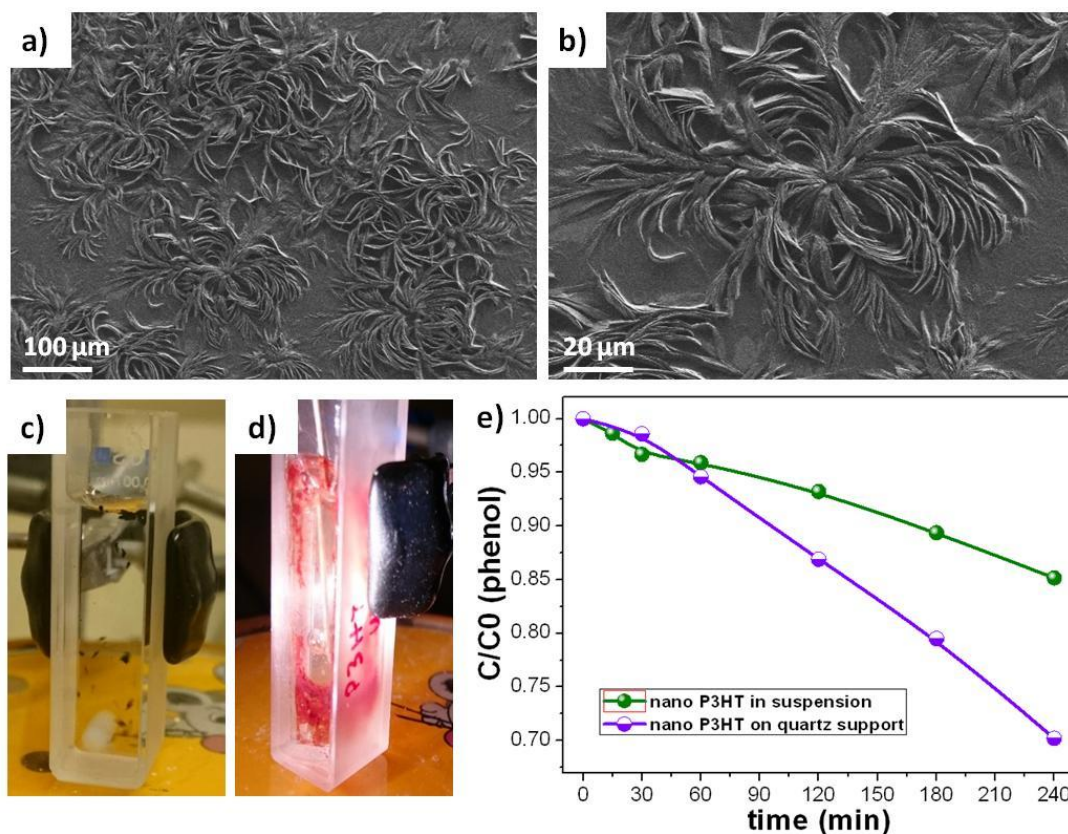


Figure 4.23 (a-b) SEM images of nano P3HT deposited on a quartz slide (from a chloroform solution) at two different magnifications; (c) nano P3HT suspension in aqueous solution containing phenol; (d) A quartz slide coated with nano P3HT inside a quartz cell containing a phenol solution irradiated with visible light; (e) Photocatalytic degradation of phenol using nano P3HT in suspension and nano P3HT on a quartz slide under visible light.

IV.3 Conclusion

In conclusion, P3HT nanostructures synthesized in hexagonal mesophases present a high photocatalytic activity under UV and visible light. These photocatalysts are very stable with cycling. Our results demonstrate that $O_2^{\cdot-}$ is the main radical responsible for the degradation of phenol taken as model pollutant. These conjugated polymer nanostructures can be easily deposited on solid supports. When deposited on quartz slides, the photocatalytic activity of the polymer nanostructures is much enhanced. These results open new perspectives for application of these conjugated polymers in photocatalytic reactors and in self-cleaning surfaces. Further studies will optimize the deposition of these nanostructures on different supports for practical applications.

Chapter V

Synthesis of Pt-PDPB (Polydiphenylbutadiyne) Nanocomposites in Hexagonal Mesophases

Synthesis of Pt-PDPB (Platinum-Polydiphenylbutadiyne) Nanocomposites in Hexagonal Mesophases

V.1 Introduction

Conjugated polymers have drawn a lot of attention since their discovery in 1960 by Weiss and co-workers who showed that certain classes of polymers such as polypyrrole and polyaniline exhibit conductivity properties.¹⁶⁷ The combination of the features of organic materials (low cost and easy processing) and of those of inorganic semiconductor materials (mechanical and thermal stability) makes conjugated polymers promising materials for a variety of opto-electronic applications such as solar cells, light emitting diodes, field-effect transistors, etc.^{156–161} As described in chapter IV, previous works of our group have shown that conjugated polymer nanostructures such as PDPB (Polydiphenylbutadiyne), PEDOT (poly(3,4-ethylenedioxythiophene), and P3HT (poly(3-hexylthiophene)) are very active photocatalytic materials for degradation of organic pollutants under visible light.^{58,119,162}

We have also shown that PDPB nanostructures can be employed as supporting polymers for Pd nanoplates used as electrocatalysts for ethanol oxidation reaction in basic media (**Figure 5.1**).¹²⁴

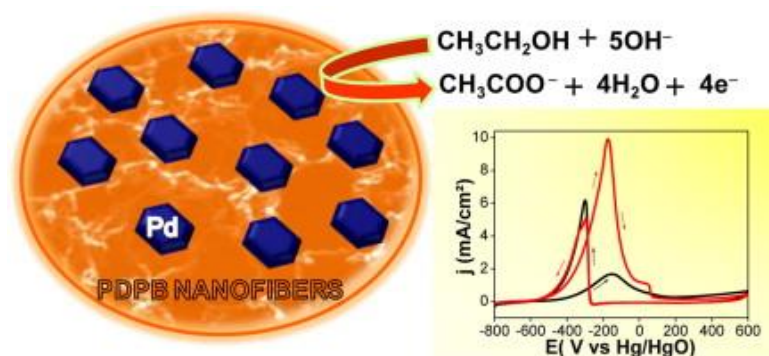


Figure 5.1 An illustration of conjugated polymer PDPB-supported Pd nanoplates for ethanol oxidation reaction in alkaline media with corresponding cyclic voltammogram of PDPB – Pd nanoplates in 1M of KOH + 1M of ethanol.¹²⁴

PDPB nanostructures are synthesized in hexagonal mesophases through gamma or UV irradiation to induce the polymerization process. The diameter of PDPB

nanostructures is controlled by the diameter of the oil tubes of the mesophase. **Figure 5.2** shows TEM images of PDPB nanostructures with different diameters prepared in hexagonal mesophases with different swelling ratios.

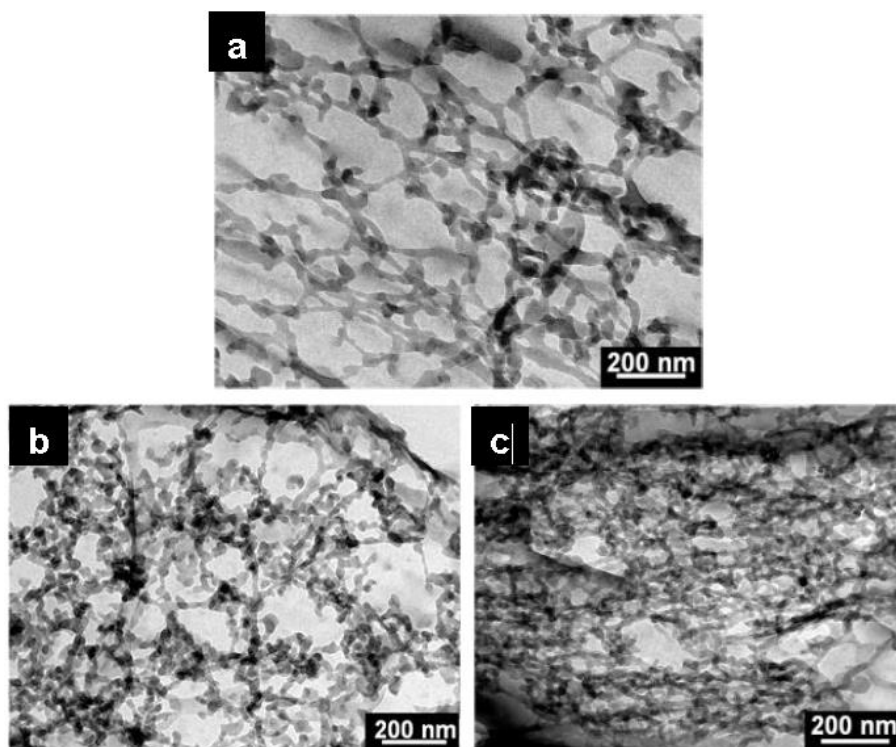


Figure 5.2 TEM images of PDPB nanostructures prepared in hexagonal mesophases with different diameter of oil tubes: **a)** $D = 20.9$ nm, **b)** $D = 11.8$ nm, and **c)** 6.68 nm through radiolysis technique.¹²⁰

The electrocatalytic activity of Pd nanoplates was evaluated using different supports: PDPB nanostructures, bulk PDPB, and Nafion, a commercial polymer electrolyte. Nafion is a widely used conducting polymer for application in fuel cells, however it is expensive and toxic. **Table 5.1** presents the comparison of the electrochemical performance of Pd nanoplates on different supporting polymers, and clearly shows that Pd nanoplates once supported on PDPB nanostructures give the highest current density and the most negative onset potential as compared to the other supporting materials (bulk PDPB and Nafion). Those values suggest that PDPB nanostructures are the best supporting polymer for Pd nanoplates for ethanol oxidation in alkaline media.¹⁸⁹

Indeed, it is well known that nanostructuring of polymers allows a uniform distribution of metal nanoparticles and therefore assists in enhancing the electrocatalytic activity.^{94,190}

Table 5.1 Comparison of electrochemical performance of Pd nanoplates on different supporting polymers.¹⁸⁹

Electrode	Forward current density (mAcm ⁻²)	Onset potential (mV)
PDPB nanostructures	9.91	-570
PDPB bulk	7.05	-557
Nafion	3.53	-520

Composite systems made by modified conjugated polymers with metal nanoparticles can show enhanced photocatalytic and electrocatalytic properties.^{191,192} In particular, Jana and co-workers have shown that gold nanoparticles-conjugated polymer (Au-P3HT) composites demonstrated a high photocatalytic activity under visible light. The increase in activity of the Au-P3HT composite has been attributed to the electronic interaction of the semiconducting polymer P3HT with the Au nanoparticles. The composite can exhibit a bathochromic shift of the absorption band and a significant photoluminescence quenching of P3HT.¹⁹³ It has to be mentioned that the polymer was not nanostructured in their case.

In the literature, different reviews report about synthesis of metal and conjugated polymer nanostructures.^{181,193} Synthesis of metal and conjugated polymer nanostructures in hexagonal mesophases, and their application in fuel cells and in photocatalysis have been presented in the previous chapters of this thesis. Mesophases can be doped with high concentrations of precursors, which can be located in the water phase and/or in the oil phase. Metal nanomaterials can be synthesized in the water phase (metal precursors are in general soluble in water) and polymer nanostructures in the organic/oil phase (the precursors are often soluble in organic solvents). Therefore, we can extend the synthesis of nanostructures using hexagonal mesophases as templates to one pot synthesis of metal-polymer nanocomposites by radiolysis or by chemical methods. It appears as a simple and convenient way to produce metal-polymer nanocomposites with well controlled size, shape, and composition. Metal-polymer nanocomposites are expected to have interesting

electronic properties and can find wide applications in electrocatalysis and photocatalysis (water depollution and H₂ production under visible light irradiation).

Here we present synthesis and characterization of Pt-PDPB nanocomposites prepared in soft template hexagonal mesophases.

V.2 Material characterization

V.2.1 Small Angle X-Ray Scattering (SAXS)

The hexagonal mesophases used as templates to synthesize Pt-PDPB nanocomposites are made of CpCl (cetylpyridinium chloride) as surfactant, cyclohexane containing 3.38 M of DPB (1,4-diphenylbutadiyne) monomer (oil phase), n-pentanol as co-surfactant, and water containing a metallic salt (Pt(NH₃)₄Cl₂·H₂O) at a concentration of 0.1 M. **Figure 5.2** represents a scheme of a hexagonal mesophase (O/W = 1.5) containing the metallic salt in the aqueous phase and the monomer in the oil phase.

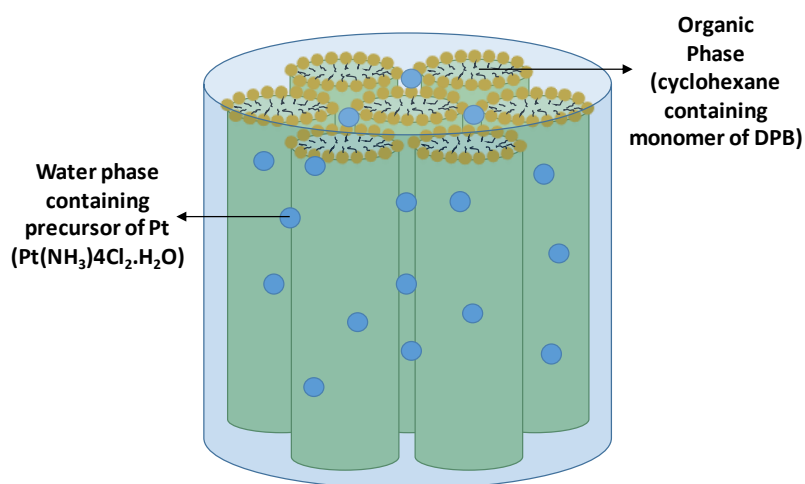


Figure 5.2 A hexagonal mesophase (containing a metallic salt and a monomer) used as soft templates to synthesize composite nanomaterials.

The formation of hexagonal mesophases is checked by small angle x-ray scattering (SAXS). **Figure 5.3** shows the SAXS spectra of mesophases containing only Pt salt, only DPB monomer and both Pt salt and DPB monomer. In all cases, hexagonal mesophases are obtained, as demonstrated by the presence of three Bragg peaks whose relative positions are those theoretically expected for a hexagonal phase (**Table 5.2**). The positions of the SAXS peaks, for the mesophases containing metallic salts and those

containing DPB monomer are very similar. However, a very small shift to smaller wavenumbers is observed for the mesophases containing Pt salt and DPB monomer, indicating a small increase in the diameter of the tubes, from 16.5 to 17.3 nm (**Table 5.2**).

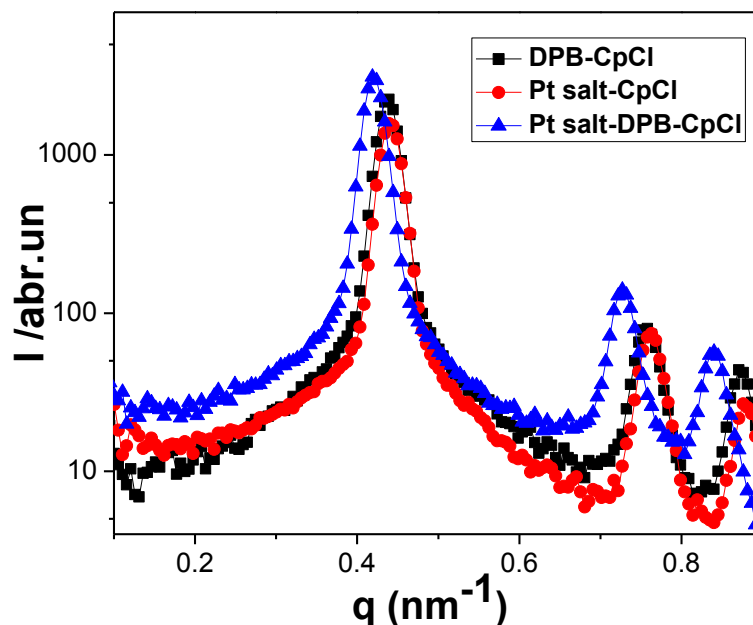


Figure 5.3 SAXS spectra of hexagonal mesophases formed by CpCl as surfactant containing PDPB, Pt or Pt-PDPB

Table 5.2 Numerical values of q_0 , q_1 , q_2 and ratios q_1/q_0 and q_2/q_0 for the samples containing Pt salt, DPB monomer, and both Pt and DPB:

Precursor	q_0 (nm ⁻¹)	q_1 (nm ⁻¹)	q_2 (nm ⁻¹)	q_1/q_0	q_2/q_0	D (nm)
DPB	0.438	0.757	0.876	1.730	2.000	16.5
Pt(NH ₃) ₄ Cl ₂ .H ₂ O	0.439	0.764	0.878	1.740	2.000	16.5
Pt(NH ₃) ₄ Cl ₂ .H ₂ O and DPB	0.42	0.727	0.841	1.730	2.002	17.3

The mesophases containing Pt salt, DPB monomer, and both Pt salt and DPB are then exposed to gamma irradiation with a total dose of 88 kGy (dose rate = 3.6 kGy/h). The radicals (solvated electron and alcohol radical) produced during radiolysis of water and alcohol (n-pentanol used as co-surfactant in our case) can reduce the platinum (II) complex (to platinum (0)) and induce the polymerization of the DPB monomer into PDPB.¹⁹⁴ The transparent mesophases turned into orange after gamma irradiation, indicating the formation of PDPB.^{58,120} After irradiation, the mesophases is still

transparent and birefringent, however, SAXS analysis would be needed to confirm their hexagonal geometry.

V.2.2 Characterization by Transmission Electron Microscopy (TEM)

The synthesized nanostructures of PDPB and Pt as well as Pt-PDPB nanocomposites were characterized by TEM.

a. PDPB nanostructures

After irradiation, the nanomaterials were extracted by adding ethanol and water to the mesophases. The upper part, which is the ethanol phase containing the nanomaterials, was further extracted from the mixture, washed several times with water-ethanol, and dried in an oven set at 40° C for 1 night. The dried nanomaterials were further dispersed in ethanol. Few drops of the suspension were deposited on carbon grids and observed by TEM.

Figure 5.3 shows TEM images of PDPB nanostructures synthesized in hexagonal mesophases (without Pt). The images reveal the formation of connected-nanowires with length of few micrometers and diameter around 22 nm. This value is close to the value of the oil tubes (18 nm), where the polymerization takes place. A direct templating effect of the mesophase has been already shown in previous studies and the diameter of the polymer nanowires can be controlled by fixing the oil tube diameter of the mesophase.¹²⁰

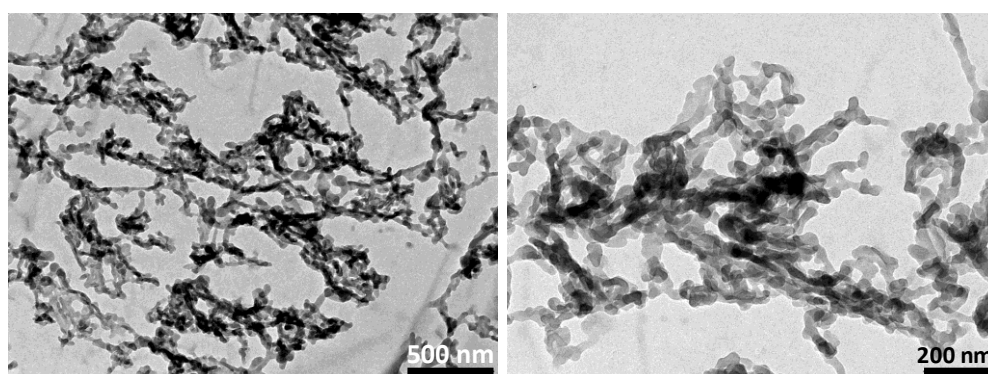


Figure 5.3 TEM images of PDPB nanostructures synthesized in hexagonal mesophases.

b. Pt nanostructures

The Pt-doped mesophases were exposed to irradiation. To extract the synthesized Pt nanomaterials, few milliliters of ethanol were added to the mesophases. Then, the upper part was taken and few drops of it were deposited on carbon grids for TEM observation.

Figure 5.4 presents TEM images of the synthesized Pt nanostructures in mesophases (in the absence of the DPB monomer). Pt nanotubes are observed. These nanotubes are formed by self-assembled small Pt nanoparticles (2.0-2.5 nm). These nanoparticles are formed in the confined water phase (diameter of water channel 3 nm). The diameter of the nanotubes is around 26 to 36 nm (larger than the diameter of the oil tubes which is around 17 nm). These nanotubes are probably formed by nanoparticles of Pt arranged around surfactants, therefore they are soft and fragile. The nanotubes can be easily flattened, reshaped or destroyed by a centrifugation process (even at low speed; less than 1000 rpm) as shown in **Figure 5.5**). The diameter of the Pt nanoparticles is not affected by the centrifugation process.

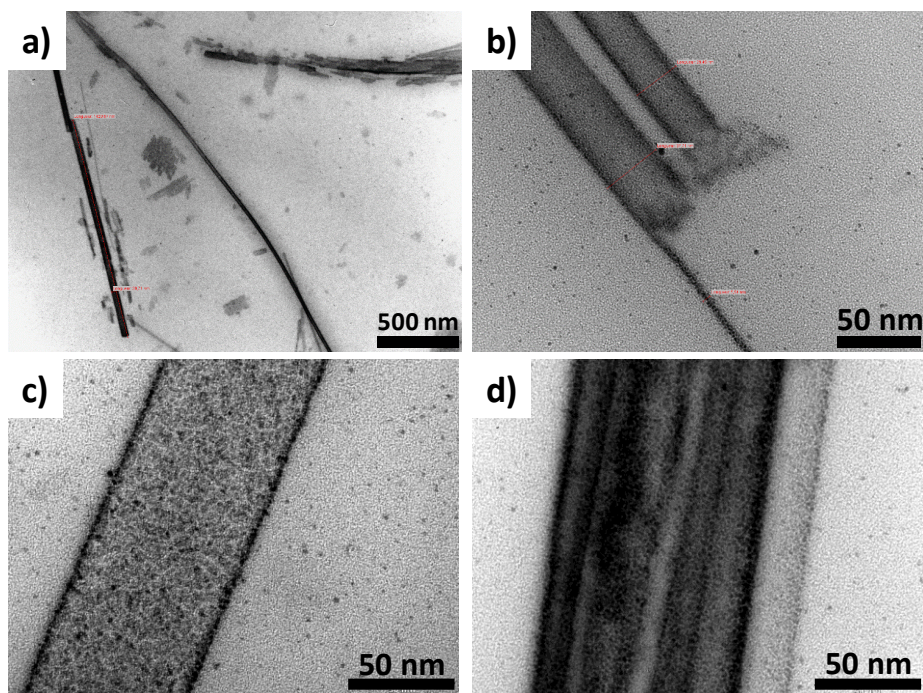


Figure 5.4 TEM images of Pt nanotubes constituted of 2-nm Pt nanoparticles.

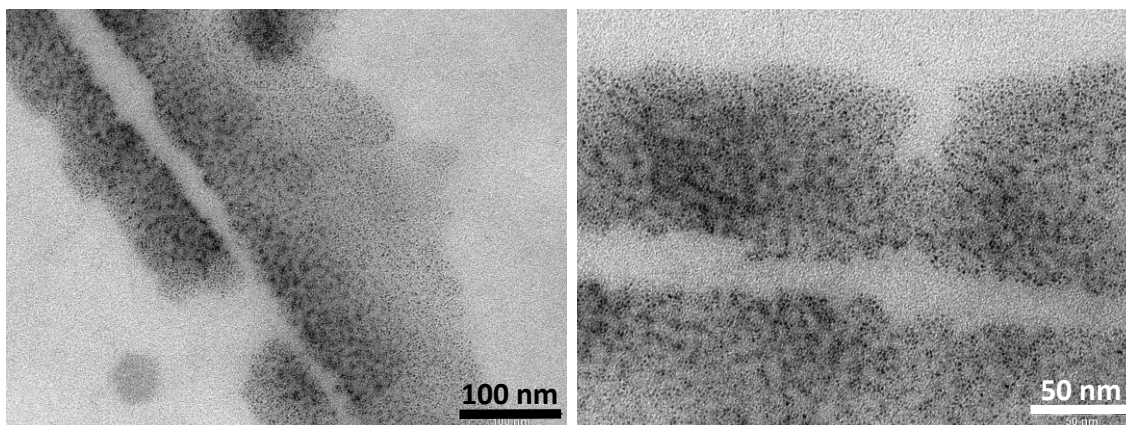


Figure 5.5 TEM images of Pt nanostructures formed by assembly of Pt nanoparticles synthesized in mesophases after centrifugation process.

c. Pt-PDPB nanocomposites

Co-doped Pt-DPB mesophases were exposed to γ -irradiation. **Figure 5.6** shows TEM images of Pt-PDPB nanocomposites synthesized in hexagonal mesophases: Pt nanotubes with diameter around 18 nm, corresponding to the diameter of the oil tubes of the hexagonal mesophases used as soft templates ($D=17.3$ nm) and few micrometers length are observed. The nanotubes are formed by Pt nanoparticles, with a diameter around 1.7 - 2.5 nm, hence comparable to the diameter of the water channel (3 nm). In this case, the nanostructures do not flatten on the TEM grid, which explains why their apparent diameter corresponds exactly to the diameter of the oil tubes. In addition, the composite nanostructures are more stable under centrifugation. Compared to Pt-nanotubes obtained in mesophases doped with only Pt complex (without DPB) (**Figure 5.4**), the nanotubes synthesized in co-doped (with Pt complex and DPB) (**Figure 5.6**) mesophases are less soft.

Irradiation of DPB-doped mesophases leads to nanowires of PDPB synthesized in the oil tubes^{46,120} while irradiation of Pt-doped mesophases leads to Pt-nanotubes. So, we expect that, in case of co-doping of the mesophase with DPB and Pt complex, the polymer PDPB will be located inside the nanotube. However, PDPB cannot be observed by TEM. Further characterization technique such as AFM-IR (atomic force microscopy combined with infrared spectroscopy) was necessary.

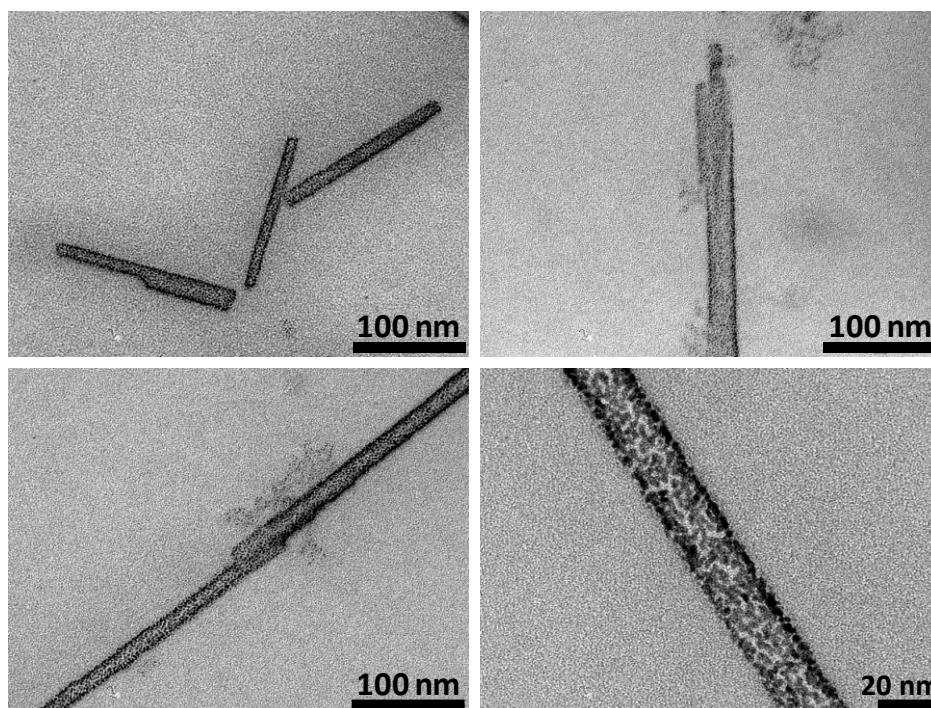


Figure 5.6 TEM images of Pt-PDPB nanocomposites synthesized in hexagonal mesophases.

V.2.3 Characterization by AFMIR

Atomic Force Microscopy combined with infrared spectroscopy (AFMIR) allows concomitant investigation of the surface topography and chemical structure. The surface topography of Pt-PDPB nanocomposites highlights the presence of tube-like structures. However, the diameter observed by AFM is much larger (1.68 μm) compared to those obtained by TEM (18 nm). The observed nanostructures by AFM were probably aggregates of smaller nanotubes formed during deposition on the ZnSe substrate (**Figure 5.7a**). The chemical mapping at 2923 cm^{-1} is attributed to benzene ring C-H in the polymer PDPB. We cannot use lower wavenumbers because the polymer will be destroyed by a high laser energy. The AFMIR spectra in **Figure 5.7c** display peaks at 2854 , 2924 , and 3057 cm^{-1} , which are characteristic peaks of C-H in benzene rings. The chemical mapping and AFMIR spectrum confirms the presence of polymer PDPB in the sample of Pt-PDPB. We conclude that the composite nanostructures are formed by nanowires of PDPB (formed in the oil phase of the mesophase) surrounded by 2 nm-Pt nanoparticles (formed in water phase).

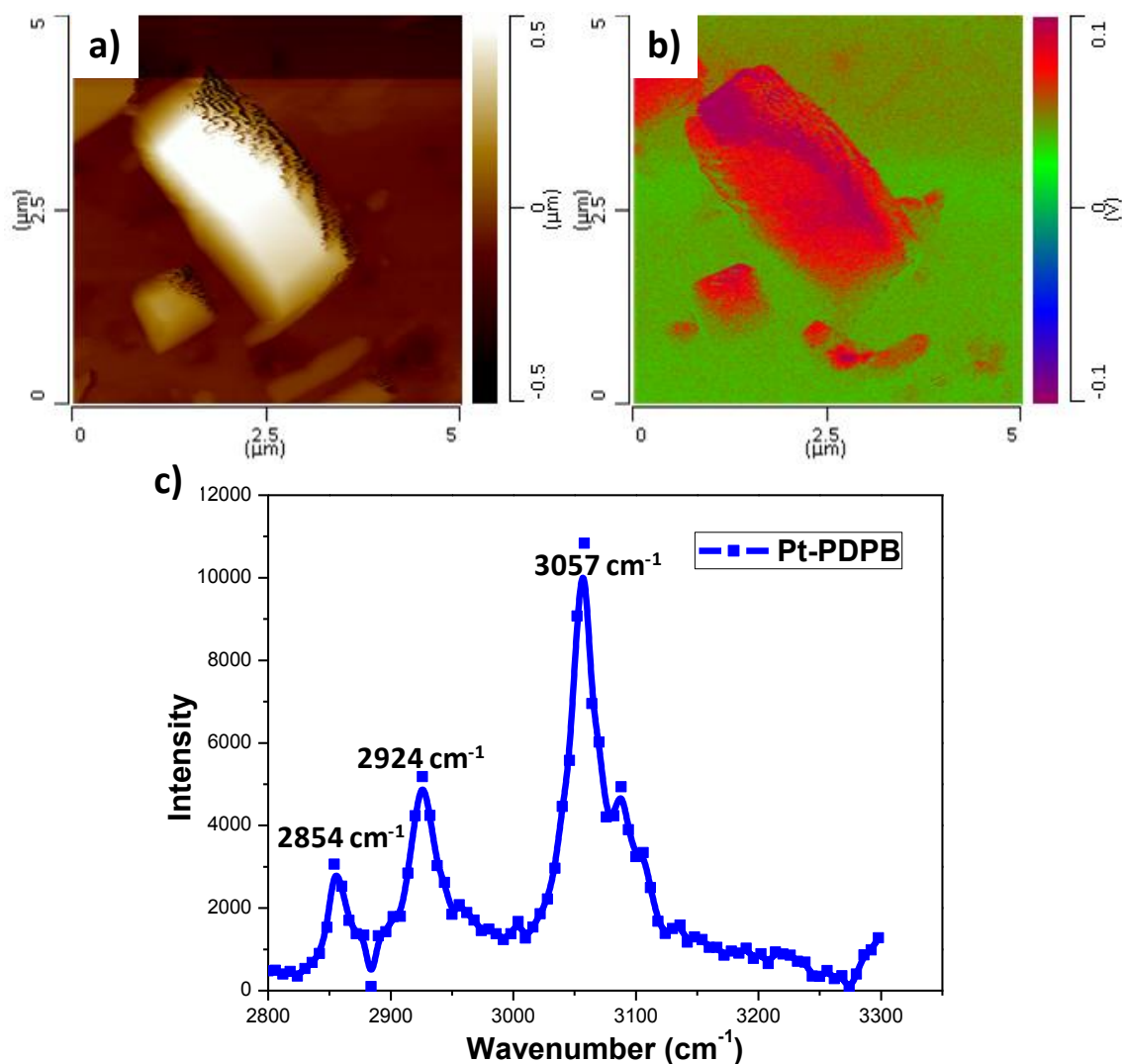


Figure 5.7 AFM topography for Pt-PDPB nanocomposites (a); Chemical mapping at 2923 cm^{-1} for nano Pt-PDPB nanocomposites (b), and (c) AFMIR spectra recorded in the region between $2800 - 3300\text{ cm}^{-1}$.

V.3 Conclusion and Perspectives

Soft Pt nanotubes formed by self-assembly of 2 nm Pt nanoparticles were synthesized by radiolysis in mesophases (initially doped with Pt complexes).

Hexagonal mesophases can be co-doped with monomers and metal salts or complexes. These mesophases were used as soft templates to synthesize metal-polymer composites of Pt-PDPB in one pot by radiolysis. TEM and AFMIR characterization show the formation of Pt-PDPB with wire-like structures with diameter around 18 nm. These nanostructures are formed by conjugated polymer PDPB nanowires surrounded by 2 nm-

Pt nanoparticles. These nanostructures will be further characterized with other techniques such as Nano-Raman and XPS. Application of these nanostructures in catalysis (such as de-NO_x or hydrogenation reactions) will be investigated.

This one-pot synthesis can be generalized to other metal/polymer composite nanostructures for different applications such as H₂ sensing or H₂ storage (with Pd-based nanostructures), catalysis, electrocatalysis, photocatalysis and photovoltaics. Composite nanostructures based on bimetallic NPs (such as Pt-Pd, Pt-Au, Pt-Ni, Au-Ni)/conjugated polymers will also be developed.

CHAPTER VI

General Conclusion and Perspectives

Chapter VI

General Conclusion and Perspectives

Soft template hexagonal mesophases, which consist of a quaternary mixture of surfactants, brine, oil, and co-surfactant, were used as templates for the synthesis of different nanomaterials such as metal nanostructures, polymer nanostructures, and metal-polymer nanocomposites. Unlike hard templates, which need a harsh chemical reagent such as hydrochloric acid to extract nanomaterials after their synthesis inside the hard template, in soft template hexagonal mesophases, the extraction process of nanomaterials is simple, and only requires a washing step with ethanol or 2-propanol. These soft templates can be doped with high concentrations of precursors (metals salts or monomers up to 0.3 M). Hence, relatively large quantities of nanomaterials can be produced. Another interesting property of this class of templates lies in its ability to be swollen by controlling the ratio of oil to water. This allows synthesis of porous metal nanomaterials of controlled porosity (synthesized in the water phase) and polymer nanowires of controlled diameters (synthesized in the oil phase).

The experimental results of the thesis are divided into three parts: 1) Radiolytic synthesis of metal nanostructures in the aqueous phase of hexagonal mesophases and their application in fuel cells, 2) Synthesis of conjugated polymer nanostructures in the oil phase of hexagonal mesophases for photocatalytic degradation of pollutants, 3) One pot synthesis (combined synthesis in the oil and water phases of hexagonal mesophases) of metal-polymer nanocomposites.

1) The synthesis of metal nanostructures for application in fuel cells

Several metal nanostructures such as PdPt nanoballs with controlled porosity and composition, Au@Pd and Au@Pt core shell, trimetallic AuPdPt and bimetallic PtNi porous nanoballs were synthesized in the aqueous phase of hexagonal mesophases using radiolysis. With this technique, very strong reducing radicals are produced homogeneously in the medium leading to homogeneous reduction and nucleation.

- Porous Pd, Pt, and PdPt (with controlled compositions) nanoballs with different pore sizes were obtained by controlling the diameter of the oil tubes of hexagonal mesophases, which can be tuned by varying the ratio of oil to water.

Characterization by TEM, BET, SAXS, and WAXS show that the pore sizes of nanoballs can be tuned from 16 to 45 nm. The pore size is equal to the diameter of the oil tube of the mesophase, proving a templating effect. These porous metal nanoballs were used as electrocatalysts for ethanol oxidation reaction in alkaline solution (in the anodic part of direct ethanol fuel cells). The composition of Pd and Pt was also varied, and Pd₇₅Pt₂₅ appeared to be the best electrocatalyst in term of activity and stability for this reaction. Cyclic voltammetry analysis showed that the electro active surface increased with porosity, which then led to the current increase. In the case of Pd nanoballs, the current density increased when the pore size increased from 16 to 20 nm and reached a plateau for pore sizes higher than 20 nm. However, in the case of PdPt nanoballs, the current density decreased with the pore size. This result was explained thanks to HAADF-TEM and EDS characterizations, which showed that the composition in Pd and Pt on the surface of nanoballs changed with the pore size. At larger pore size, the ratio Pd/Pt on the surface of nanoballs is higher (at a fixed initial concentration), explaining the decrease of the current density with pore size. Higher amount of Pd on the surface at larger pore size is thus assumed to be the cause of less active electrocatalysts.

- Au@Pd (Au₅Pd₉₅ and Au₁₀Pd₉₀), Au@Pt (Au₅Pt₉₅ and Au₁₀Pt₉₀), and Au₅Pd₇₀Pt₂₅ nanostructures were also synthesized in hexagonal mesophases and used for ethanol oxidation reaction. Au@Pd and Au@Pt showed a core-shell structure with gold is in the core surrounded by 3D-connected Pd and Pt nanowires, while Au₅Pd₇₀Pt₂₅ were nanoballs formed by connected nanowires (no core of gold is observed). The trimetallic nanoballs of composition Au₅Pd₇₀Pt₂₅ perform as a better electrocatalyst compared to Pd nanoballs, Pd₇₅Pt₂₅ nanoballs, and Au₅Pd₉₅ core shell nanostructures. Other characterization techniques, such as HAADF, EDS, WAXS and XPS, will be performed to better characterize these nanostructures and their porosity, and determine metal oxidation states.
- Finally, porous Pt₈₅Ni₁₅ nanoballs were synthesized in hexagonal mesophases (using two different sources of irradiation: gamma rays and electron beams) and were used as electrocatalysts for H₂ evolution reaction in acidic media. The sample prepared by electron beam was approximately two times more active than the one prepared by gamma irradiation. However, the activities of these two samples were

lower compared to that of Pt nanoballs. Based on recent literature, we believe that these PtNi nanostructures could be promising electrocatalysts for oxygen reduction reaction. Experiments will be conducted to study their activity for this reaction.

2) The synthesis of conjugated polymer for application in photocatalysis

P3HT (poly(3-hexylthiophene)) nanostructures synthesized in the oil phase of hexagonal mesophases by oxidative polymerization process presented a high photocatalytic activity under UV and visible light for degradation and mineralization of organic pollutants in water. These photocatalysts were found to be very stable with cycling. The mechanistic studies demonstrate that $O_2^{\cdot-}$ was the main radical responsible for the degradation of phenol and Rhodamine B taken as model pollutants. These conjugated polymer nanostructures could be easily deposited on solid supports. When deposited on quartz slides, the photocatalytic activity of the polymer nanostructures was much enhanced. These results open new perspectives for applications in photocatalytic reactors and in self-cleaning surfaces. Further studies are needed to optimize the deposition of these nanostructures on different supports for practical applications. In addition, the modification of these P3HT nanostructures with metal nanoparticles can open new application for H_2 evolution from water under visible light.

Harnessing solar energy and storing it in a chemical form is the most promising green large-scale technological deployment to match our ever-increasing need of energy. In collaboration with Stéphanie Mendes (ICMMO, Université Paris-Saclay), Ally Aukauloo (ICMMO, Université Paris-Saclay) and Wienfried Leibl (CEA, Saclay), we recently demonstrated for the first time that nanostructured conjugated polymers (in particular PDPB (Poly(diphenylbutadiyne)) nanowires when dispersed in water, and in the absence of sacrificial agents or co-catalysts, could perform photocatalytic water oxidation under visible light excitation (submitted). Preliminary results obtained with PDPB nanowires and polypyrrole (PPy) nanostructures show that modifying PDPB and PPy with a small amount of Pt nanoparticles (diameter around 2 nm) (0.1% in weight) led to H_2 production under solar light. These findings open new perspectives for the application of nanostructured conjugated polymers for water splitting. These polymer

nanostructures will be modified with co-catalysts without noble metals (Ni and Co nanoparticles, C dots, etc...) for this application.

3) The synthesis of Pt-PDPB nanocomposites

Hexagonal mesophases could be co-doped with monomers (in the oil phase) and metal salts (in the water phase). The doped mesophases were used as soft templates to synthesize metal-polymer nanocomposites of Pt-PDPB in one pot radiolytic synthesis. Characterizations by TEM and AFMIR showed the formation of Pt-PDPB with wire-like structures formed by conjugated polymer PDPB nanowires surrounded by 2 nm-Pt nanoparticles. These nanostructures will be further characterized with other techniques such as Nano-Raman and XPS. Application of these nanostructures in catalysis (such as de-NO_x or hydrogenation reactions) will be investigated. This one-pot synthesis can be generalized to other metal/polymer composite nanostructures for different applications such as H₂ sensing or H₂ storage (with Pd-based nanostructures), catalysis, electrocatalysis, photocatalysis and photovoltaics. Composite nanostructures based on bimetallic NPs (such as Pt-Pd, Pt-Au, Pt-Ni, Au-Ni)/conjugated polymers will also be developed.

All the results obtained in this thesis show that hexagonal mesophases are very versatile templates to synthesize porous metal nanostructures of controlled porosity (including bimetallic and trimetallic nanostructures), conjugated polymer nanostructures, and composite metal/polymer nanomaterials. These nanomaterials can have applications in electrocatalysis for fuel cells application, catalysis, photocatalysis, solar cells, hydrogen storage, sensing, etc...

Radiolysis appears as a very efficient technique to synthesize a large panel of nanomaterials and industrial protocols can be developed. Ionizing radiations (mainly electron beams and gamma rays) are indeed currently applied in the industry, where large volumes can be treated for medical and surgery material sterilization, and food decontamination (spices, fruits...). There are several companies selling radiations in France, such as *Ionisos*. Therefore, the development of synthetic protocols for catalytic materials by radiolysis could be transposed to industrial production in the middle term. A

few liters of mesophases yield a few grams of materials, but as large volumes can be irradiated, relatively large quantities of nanomaterials can be produced.

PUBLICATIONS RELATED TO THE THESIS:

“Highly Active Poly(3-hexylthiophene) Nanostructures for Photocatalysis under Solar Light”, **D. Floresyona**, F. Goubard, P-H. Aubert, I. Lampre, J. Mathurin, A. Dazzi, S. Ghosh, P. Beaunier, F. Brisset, S. Remita, L. Ramos, H. Remita, *Applied Catalysis B: Environmental*, 209, 23-32 (2017).
<http://dx.doi.org/10.1016/j.apcatb.2017.02.069>

“Conducting polymer-supported palladium nanoplates for applications in direct alcohol oxidation”, S. Ghosh, A-L. Teillout, **D. Floresyona**, P. de Oliveira, A. Hagege, H. Remita, *International Journal of Hydrogen Energy*, 40, 4951-4959,(2015)
<http://dx.doi.org/10.1016/j.ijhydene.2015.01.101>

“Visible-Light-Driven Water Oxidation by Conjugated Polymer Nanostructures without the Assistance of Co-Catalyst”
S. Mendes Marinho, W. Leibl, D. Floresyona, F. Goubard, P-H. Aubert, S. Ghosh, H. Remita, A. Aukauloo, [submitted](#).

References:

1. Trevors, J. T. What is a Global Environmental Pollution Problem? *Water. Air. Soil Pollut.* **210**, 1–2 (2010).
2. Mearns, E. Primary Energy in The European Union and USA Compared. *Energy Matters* (2016).
3. Pollution and exhaustibility of fossil fuels - ScienceDirect. Available at: <http://www.sciencedirect.com/science/article/pii/0928765594900078>. (Accessed: 13th July 2017)
4. Shiklomanov, I. A. Appraisal and Assessment of World Water Resources. *Water Int.* **25**, 11–32 (2000).
5. Rao, C. N. R., Müller, A. & Cheetham, A. K. Nanomaterials – An Introduction. in *The Chemistry of Nanomaterials* (eds. Rao, C. N. R., Müller, A. & Cheetham, A. K. C.) 1–11 (Wiley-VCH Verlag GmbH & Co. KGaA, 2004). doi:10.1002/352760247X.ch1
6. Sun, S., Murray, C. B., Weller, D., Folks, L. & Moser, A. Monodisperse FePt Nanoparticles and Ferromagnetic FePt Nanocrystal Superlattices. *Science* **287**, 1989–1992 (2000).
7. Eychmüller, A. Structure and Photophysics of Semiconductor Nanocrystals. *J. Phys. Chem. B* **104**, 6514–6528 (2000).
8. Huynh, W. U., Dittmer, J. J. & Alivisatos, A. P. Hybrid Nanorod-Polymer Solar Cells. *Science* **295**, 2425–2427 (2002).
9. El-Sayed, M. A. Some Interesting Properties of Metals Confined in Time and Nanometer Space of Different Shapes. *Acc. Chem. Res.* **34**, 257–264 (2001).
10. Sasaki, M. *et al.* Templating fabrication of platinum nanoparticles and nanowires using the confined mesoporous channels of FSM-16—their structural characterization and catalytic performances in water gas shift reaction. *J. Mol. Catal. Chem.* **141**, 223–240 (1999).
11. Fukuoka, A. *et al.* Preparation and catalysis of Pt and Rh nanowires and particles in FSM-16. *Microporous Mesoporous Mater.* **48**, 171–179 (2001).

12. Belloni, J., Mostafavi, M., Remita, H., Marignier, J.-L. & Delcourt, M.-O. Radiation-induced synthesis of mono- and multi-metallic clusters and nanocolloids. *New J. Chem.* **22**, 1239–1255 (1998).
13. Remita, S., Orts, J. M., Feliu, J. M., Mostafavi, M. & Delcourt, M. O. STM identification of silver oligomer clusters prepared by radiolysis in aqueous solution. *Chem. Phys. Lett.* **218**, 115–121 (1994).
14. Krishnaswamy, R. *et al.* Synthesis of Single-Crystalline Platinum Nanorods within a Soft Crystalline Surfactant–PtII Complex. *ChemPhysChem* **7**, 1510–1513 (2006).
15. Surendran, G. *et al.* Synthesis of Porous Platinum Nanoballs in Soft Templates. *Chem. Mater.* **19**, 5045–5048 (2007).
16. Surendran, G. *et al.* Palladium Nanoballs Synthesized in Hexagonal Mesophases. *J. Phys. Chem. C* **112**, 10740–10744 (2008).
17. Ghosh, S. *et al.* Conducting polymer nanofibers with controlled diameters synthesized in hexagonal mesophases. *New J. Chem.* **39**, 8311–8320 (2015).
18. Belloni, J. Nucleation, growth and properties of nanoclusters studied by radiation chemistry. *Catal. Today* **113**, 141–156 (2006).
19. Belloni, J., Douki, T. & Mostafavi, M. *Radiation chemistry*. (EDP Sciences, 2012).
20. Remita, H. & Remita, S. Metal Clusters and Nanomaterials: Contribution of Radiation Chemistry. in *Recent Trends in Radiation Chemistry* 347–383 (WORLD SCIENTIFIC, 2010). doi:10.1142/9789814282093_0013
21. Abidi, W. & Remita, H. Gold based Nanoparticles Generated by Radiolytic and Photolytic Methods. *Recent Pat. Eng.* **4**, 170–188 (2010).
22. Bohren, C. F. & Huffman, D. R. Absorption and Scattering by an Arbitrary Particle. in *Absorption and Scattering of Light by Small Particles* 57–81 (Wiley-VCH Verlag GmbH, 1998). doi:10.1002/9783527618156.ch3
23. Liu, Y., Goebel, J. & Yin, Y. Templated synthesis of nanostructured materials. *Chem. Soc. Rev.* **42**, 2610–2653 (2013).
24. Kim, O.-H. *et al.* Ordered macroporous platinum electrode and enhanced mass transfer in fuel cells using inverse opal structure. *Nat. Commun.* **4**, ncomms3473 (2013).

25. Kitahara, M. *et al.* Preparation of Mesoporous Bimetallic Au–Pt with a Phase-Segregated Heterostructure Using Mesoporous Silica. *Chem. – Eur. J.* **21**, 19142–19148 (2015).
26. Lee, W. & Park, S.-J. Porous Anodic Aluminum Oxide: Anodization and Templated Synthesis of Functional Nanostructures. *Chem. Rev.* **114**, 7487–7556 (2014).
27. Fei, J. *et al.* Controlled Fabrication of Polyaniline Spherical and Cubic Shells with Hierarchical Nanostructures. *ACS Nano* **3**, 3714–3718 (2009).
28. Trueba, M., Montero, A. L. & Rieumont, J. Pyrrole nanoscaled electropolymerization. *Electrochimica Acta* **49**, 4341–4349 (2004).
29. Cho, M. S., Choi, H. J. & Ahn, W.-S. Enhanced Electrorheology of Conducting Polyaniline Confined in MCM-41 Channels. *Langmuir* **20**, 202–207 (2004).
30. Holade, Y., Lehoux, A., Remita, H., Kokoh, K. B. & Napporn, T. W. Efficient Design and Fabrication of Porous Metallic Electrocatalysts. in *Electrocatalysts for Low Temperature Fuel Cells* (eds. Thandavarayanialagan & Saji, V. S.) 511–531 (Wiley-VCH Verlag GmbH & Co. KGaA, 2017). doi:10.1002/9783527803873.ch18
31. Holmberg, K., Jönsson, B., Kronberg, B. & Lindman, B. Introduction to Surfactants. in *Surfactants and Polymers in Aqueous Solution* 1–37 (John Wiley & Sons, Ltd, 2002). doi:10.1002/0470856424.ch1
32. Detergent Properties and Applications. *Sigma-Aldrich* Available at: <http://www.sigmaaldrich.com/technical-documents/articles/biofiles/detergent-properties.html>. (Accessed: 17th June 2017)
33. Polyethylene glycol. *Wikipedia* (2017).
34. Bhardwaj, V., Sharma, K., Chauhan, S. & Sharma, P. Intermolecular interactions of CTAB and potential oxidation inhibitors: physico-chemical controlled approach for food/pharmaceutical function. *RSC Adv.* **4**, 49400–49414 (2014).
35. Zarei, A. R., Bagheri Sadeghi, H. & Abedin, S. Selective Cloud Point Extraction for the Spectrophotometric Determination of Cetylpyridinium Chloride in Pharmaceutical Formulations. *Iran. J. Pharm. Res. IJPR* **12**, 671–677 (2013).
36. Naskar, B., Mondal, S. & Moulik, S. P. Amphiphilic activities of anionic sodium cholate (NaC), zwitterionic 3-[(3-cholamidopropyl)dimethylammonio]-1-

- propanesulfonate (CHAPS) and their mixtures: A comparative study. *Colloids Surf. B Biointerfaces* **112**, 155–164 (2013).
37. Holmberg, K., Jönsson, B., Kronberg, B. & Lindman, B. Surfactant Micellization. in *Surfactants and Polymers in Aqueous Solution* 39–66 (John Wiley & Sons, Ltd, 2002). doi:10.1002/0470856424.ch2
 38. Findenegg, G. H. J. N. Israelachvili: Intermolecular and Surface Forces (With Applications to Colloidal and Biological Systems). Academic Press, London, Orlando, San Diego, New York, Toronto, Montreal, Sydney, Tokyo 1985. 296 Seiten, Preis: \$ 65.00. *Berichte Bunsenges. Für Phys. Chem.* **90**, 1241–1242 (1986).
 39. Israelachvili, J. The science and applications of emulsions — an overview. *Colloids Surf. Physicochem. Eng. Asp.* **91**, 1–8 (1994).
 40. Israelachvili, J. N., Mitchell, D. J. & Ninham, B. W. Theory of self-assembly of hydrocarbon amphiphiles into micelles and bilayers. *J. Chem. Soc., Faraday Trans. 2* **72**, 1525–1568 (1976).
 41. Holmberg, K., Jönsson, B., Kronberg, B. & Lindman, B. Phase Behaviour of Concentrated Surfactant Systems. in *Surfactants and Polymers in Aqueous Solution* 67–96 (John Wiley & Sons, Ltd, 2002). doi:10.1002/0470856424.ch3
 42. Hill, J. P., Shrestha, L. K., Ishihara, S., Ji, Q. & Ariga, K. Self-Assembly: From Amphiphiles to Chromophores and Beyond. *Molecules* **19**, 8589–8609 (2014).
 43. Liu, Q., Sun, Z., Dou, Y., Kim, J. H. & Dou, S. X. Two-step self-assembly of hierarchically-ordered nanostructures. *J. Mater. Chem. A* **3**, 11688–11699 (2015).
 44. Pena dos Santos, E. *et al.* Existence and Stability of New Nanoreactors: Highly Swollen Hexagonal Liquid Crystals. *Langmuir* **21**, 4362–4369 (2005).
 45. Ksar, F. *et al.* Palladium Nanowires Synthesized in Hexagonal Mesophases: Application in Ethanol Electrooxidation. *Chem. Mater.* **21**, 1612–1617 (2009).
 46. Ghosh, S. *et al.* Conducting polymer nanostructures for photocatalysis under visible light. *Nat. Mater.* **14**, 505–511 (2015).
 47. Ghosh, S. *et al.* PEDOT nanostructures synthesized in hexagonal mesophases. *New J. Chem.* **38**, 1106–1115 (2014).
 48. Lehoux, A. *et al.* Tuning the Porosity of Bimetallic Nanostructures by a Soft Templating Approach. *Adv. Funct. Mater.* **22**, 4900–4908 (2012).

49. Siril, P. F. *et al.* Synthesis of Ultrathin Hexagonal Palladium Nanosheets. *Chem. Mater.* **21**, 5170–5175 (2009).
50. Dutt, S., Siril, P. F. & Remita, S. Swollen liquid crystals (SLCs): a versatile template for the synthesis of nano structured materials. *RSC Adv.* **7**, 5733–5750 (2017).
51. Ksar, F. *et al.* Bimetallic Palladium–Gold Nanostructures: Application in Ethanol Oxidation. *Chem. Mater.* **21**, 3677–3683 (2009).
52. Berhault, G., Bisson, L., Thomazeau, C., Verdon, C. & Uzio, D. Preparation of nanostructured Pd particles using a seeding synthesis approach—Application to the selective hydrogenation of buta-1,3-diene. *Appl. Catal. Gen.* **327**, 32–43 (2007).
53. Johnson, C. J., Dujardin, E., Davis, S. A., Murphy, C. J. & Mann, S. Growth and form of gold nanorods prepared by seed-mediated, surfactant-directed synthesis. *J. Mater. Chem.* **12**, 1765–1770 (2002).
54. Ghosh, S. *et al.* Visible-light active conducting polymer nanostructures with superior photocatalytic activity. *Sci. Rep.* **5**, srep18002 (2015).
55. Pena dos Santos, E. *et al.* Existence and Stability of New Nanoreactors: Highly Swollen Hexagonal Liquid Crystals. *Langmuir* **21**, 4362–4369 (2005).
56. Block, B. P. & Bailar, J. C. The Reaction of Gold(III) with Some Bidentate Coördinating Groups¹. *J. Am. Chem. Soc.* **73**, 4722–4725 (1951).
57. Grabowska, E. *et al.* Modification of Titanium(IV) Dioxide with Small Silver Nanoparticles: Application in Photocatalysis. *J. Phys. Chem. C* **117**, 1955–1962 (2013).
58. Ghosh, S. *et al.* Conducting polymer nanostructures for photocatalysis under visible light. *Nat. Mater.* **14**, 505–511 (2015).
59. Dazzi, A. & Prater, C. B. AFM-IR: Technology and Applications in Nanoscale Infrared Spectroscopy and Chemical Imaging. *Chem. Rev.* **117**, 5146–5173 (2017).
60. Gritzner, G. & Kůta, J. Recommendations on reporting electrode potentials in nonaqueous solvents. *Electrochimica Acta* **29**, 869–873 (1984).
61. Boudghene Stambouli, A. & Traversa, E. Fuel cells, an alternative to standard sources of energy. *Renew. Sustain. Energy Rev.* **6**, 295–304 (2002).
62. Wiley: Modeling and Control of Fuel Cells: Distributed Generation Applications - M. H. Nehrir, C. Wang. Available at:

<http://www.wiley.com/WileyCDA/WileyTitle/productCd-0470233281.html>.

(Accessed: 11th June 2017)

63. Xu, H., Kong, L. & Wen, X. Fuel cell power system and high power DC-DC converter. *IEEE Trans. Power Electron.* **19**, 1250–1255 (2004).
64. Xin, K. & Khambadkone, A. M. Dynamic modelling of fuel cell with power electronic current and performance analysis. in *The Fifth International Conference on Power Electronics and Drive Systems, 2003. PEDS 2003.* **1**, 607–612 (2003).
65. Ozpineci, B., Tolbert, L. M., Su, G. J. & Du, Z. Optimum fuel cell utilization with multilevel DC-DC converters. in *Nineteenth Annual IEEE Applied Power Electronics Conference and Exposition, 2004. APEC '04* **3**, 1572–1576 Vol.3 (2004).
66. Ozpineci, B., Tolbert, L. M. & Du, Z. Optimum fuel cell utilization with multilevel inverters. in *2004 IEEE 35th Annual Power Electronics Specialists Conference (IEEE Cat. No.04CH37551)* **6**, 4798–4802 Vol.6 (2004).
67. Wai, R.-J., Duan, R.-Y., Lee, J.-D. & Liu, L.-W. High-efficiency fuel-cell power inverter with soft-switching resonant technique. *IEEE Trans. Energy Convers.* **20**, 485–492 (2005).
68. Jang, S. J., Won, C. Y., Lee, B. K. & Hur, J. Fuel Cell Generation System With a New Active Clamping Current-Fed Half-Bridge Converter. *IEEE Trans. Energy Convers.* **22**, 332–340 (2007).
69. Lai, J. S. A high-performance V6 converter for fuel cell power conditioning system. in *2005 IEEE Vehicle Power and Propulsion Conference* 7 pp.- (2005). doi:10.1109/VPPC.2005.1554624
70. Sickel, R. *et al.* Modular converter for fuel cell systems with buffer storage. in *2005 European Conference on Power Electronics and Applications* 9 pp.-P.9 (2005). doi:10.1109/EPE.2005.219721
71. Todorovic, M. H., Palma, L. & Enjeti, P. Design of a wide input range DC-DC converter with a robust power control scheme suitable for fuel cell power conversion. in *Nineteenth Annual IEEE Applied Power Electronics Conference and Exposition, 2004. APEC '04* **1**, 374–379 Vol.1 (2004).
72. Song, Y. J., Chung, S.-K. & Enjeti, P. N. A current-fed HF link direct DC/AC converter with active harmonic filter for fuel cell power systems. in *Conference*

- Record of the 2004 IEEE Industry Applications Conference, 2004. 39th IAS Annual Meeting.* **1**, 128 Vol.1 (2004).
73. Tuckey, A. M. & Krase, J. N. A low-cost inverter for domestic fuel cell applications. in *2002 IEEE 33rd Annual IEEE Power Electronics Specialists Conference. Proceedings (Cat. No.02CH37289)* **1**, 339–346 vol.1 (2002).
 74. Kim, Y.-H., Moon, H.-W., Kim, S.-H., Cheong, E.-J. & Won, C.-Y. A fuel cell system with Z-source inverters and ultracapacitors. in *The 4th International Power Electronics and Motion Control Conference, 2004. IPEMC 2004.* **3**, 1587–1591 Vol.3 (2004).
 75. Wang, J., Peng, F. Z., Anderson, J., Joseph, A. & Buffenbarger, R. Low cost fuel cell inverter system for residential power generation. in *Nineteenth Annual IEEE Applied Power Electronics Conference and Exposition, 2004. APEC '04* **1**, 367–373 Vol.1 (2004).
 76. Jain, S., Jiang, J., Huang, X. & Stevandic, S. Single Stage Power Electronic Interface for a Fuel Cell Based Power Supply System. in *2007 IEEE Canada Electrical Power Conference* 201–206 (2007). doi:10.1109/EPC.2007.4520330
 77. Kirubakaran, A., Jain, S. & Nema, R. K. A review on fuel cell technologies and power electronic interface. *Renew. Sustain. Energy Rev.* **13**, 2430–2440 (2009).
 78. Rydén, M. Hydrogen production from fossil fuels with carbon dioxide capture, using chemical-looping technologies. (Chalmers University of Technology, 2008).
 79. Recent Advances in Fuel Cells for Transportation Applications. Available at: <http://papers.sae.org/1999-01-0534/>. (Accessed: 11th June 2017)
 80. Lamy, C. *et al.* Recent advances in the development of direct alcohol fuel cells (DAFC). *J. Power Sources* **105**, 283–296 (2002).
 81. An, L., Zhao, T. S., Shen, S. Y., Wu, Q. X. & Chen, R. Alkaline direct oxidation fuel cell with non-platinum catalysts capable of converting glucose to electricity at high power output. *J. Power Sources* **196**, 186–190 (2011).
 82. An, L., Zhao, T. S., Shen, S. Y., Wu, Q. X. & Chen, R. Performance of a direct ethylene glycol fuel cell with an anion-exchange membrane. *Int. J. Hydrog. Energy* **35**, 4329–4335 (2010).
 83. An, L., Zhao, T. S., Chen, R. & Wu, Q. X. A novel direct ethanol fuel cell with high power density. *J. Power Sources* **196**, 6219–6222 (2011).

84. Park, K.-W. & Sung, Y.-E. Catalytic Activity of Platinum on Ruthenium Electrodes with Modified (Electro)chemical States. *J. Phys. Chem. B* **109**, 13585–13589 (2005).
85. Kua, J. & Goddard, W. A. Oxidation of Methanol on 2nd and 3rd Row Group VIII Transition Metals (Pt, Ir, Os, Pd, Rh, and Ru): Application to Direct Methanol Fuel Cells. *J. Am. Chem. Soc.* **121**, 10928–10941 (1999).
86. Deshpande, K., Mukasyan, A. & Varma, A. High throughput evaluation of perovskite-based anode catalysts for direct methanol fuel cells. *J. Power Sources* **158**, 60–68 (2006).
87. Kamarudin, M. Z. F., Kamarudin, S. K., Masdar, M. S. & Daud, W. R. W. Review: Direct ethanol fuel cells. *Int. J. Hydrog. Energy* **38**, 9438–9453 (2013).
88. Holade, Y., Lehoux, A., Remita, H., Kokoh, K. B. & Napporn, T. W. Au@Pt Core–Shell Mesoporous Nanoballs and Nanoparticles as Efficient Electrocatalysts toward Formic Acid and Glucose Oxidation. *J. Phys. Chem. C* **119**, 27529–27539 (2015).
89. Zhang, R. & Chen, W. Synthesis and Electrocatalysis of Pt-Pd Bimetallic Nanocrystals for Fuel Cells. in *Nanomaterials for Fuel Cell Catalysis* (eds. Ozoemena, K. I. & Chen, S.) 169–223 (Springer International Publishing, 2016). doi:10.1007/978-3-319-29930-3_4
90. Dimos, M. M. & Blanchard, G. J. Evaluating the Role of Pt and Pd Catalyst Morphology on Electrocatalytic Methanol and Ethanol Oxidation. *J. Phys. Chem. C* **114**, 6019–6026 (2010).
91. Srinivasan, S., Davé, B. B., Murugesamoorthi, K. A., Parthasarathy, A. & Appleby, A. J. Overview of Fuel Cell Technology. in *Fuel Cell Systems* (eds. Blomen, L. J. M. J. & Mugerwa, M. N.) 37–72 (Springer US, 1993). doi:10.1007/978-1-4899-2424-7_3
92. Wang, H.-F. & Liu, Z.-P. Selectivity of Direct Ethanol Fuel Cell Dictated by a Unique Partial Oxidation Channel. *J. Phys. Chem. C* **111**, 12157–12160 (2007).
93. Liang, Z. X., Zhao, T. S., Xu, J. B. & Zhu, L. D. Mechanism study of the ethanol oxidation reaction on palladium in alkaline media. *Electrochimica Acta* **54**, 2203–2208 (2009).

94. Lamy, C., Belgsir, E. M. & Léger, J.-M. Electrocatalytic oxidation of aliphatic alcohols: Application to the direct alcohol fuel cell (DAFC). *J. Appl. Electrochem.* **31**, 799–809 (2001).
95. Zhou, W. *et al.* Pt based anode catalysts for direct ethanol fuel cells. *Appl. Catal. B Environ.* **46**, 273–285 (2003).
96. S. Lai, S. C. & M. Koper, M. T. Ethanol electro- oxidation on platinum in alkaline media. *Phys. Chem. Chem. Phys.* **11**, 10446–10456 (2009).
97. Camara, G. A. & Iwasita, T. Parallel pathways of ethanol oxidation: The effect of ethanol concentration. *J. Electroanal. Chem.* **578**, 315–321 (2005).
98. Wang, Y., Zou, S. & Cai, W.-B. Recent Advances on Electro-Oxidation of Ethanol on Pt- and Pd-Based Catalysts: From Reaction Mechanisms to Catalytic Materials. *Catalysts* **5**, 1507–1534 (2015).
99. Shao, M., Chang, Q., Dodelet, J.-P. & Chenitz, R. Recent Advances in Electrocatalysts for Oxygen Reduction Reaction. *Chem. Rev.* **116**, 3594–3657 (2016).
100. Holade, Y., Lehoux, A., Remita, H., Kokoh, K. B. & Napporn, T. W. Efficient Design and Fabrication of Porous Metallic Electrocatalysts. in *Electrocatalysts for Low Temperature Fuel Cells* (eds. Thandavarayanialagan & Saji, V. S.) 511–531 (Wiley-VCH Verlag GmbH & Co. KGaA, 2017). doi:10.1002/9783527803873.ch18
101. Menzel, N., Ortel, E., Kraehnert, R. & Strasser, P. Electrocatalysis Using Porous Nanostructured Materials. *ChemPhysChem* **13**, 1385–1394 (2012).
102. Jiang, B. *et al.* Morphosynthesis of nanoporous pseudo Pd@Pt bimetallic particles with controlled electrocatalytic activity. *J. Mater. Chem. A* **4**, 6465–6471 (2016).
103. Lehoux, A. *et al.* Tuning the Porosity of Bimetallic Nanostructures by a Soft Templating Approach. *Adv. Funct. Mater.* **22**, 4900–4908 (2012).
104. Ksar, F. *et al.* Bimetallic Palladium–Gold Nanostructures: Application in Ethanol Oxidation. *Chem. Mater.* **21**, 3677–3683 (2009).
105. Stamenkovic, V. R. *et al.* Improved Oxygen Reduction Activity on Pt₃Ni(111) via Increased Surface Site Availability. *Science* **315**, 493–497 (2007).
106. Snyder, J., Fujita, T., Chen, M. W. & Erlebacher, J. Oxygen reduction in nanoporous metal–ionic liquid composite electrocatalysts. *Nat. Mater.* **9**, 904–907 (2010).

107. Jung, N., Chung, D. Y., Ryu, J., Yoo, S. J. & Sung, Y.-E. Pt-based nanoarchitecture and catalyst design for fuel cell applications. *Nano Today* **9**, 433–456 (2014).
108. Xia, T. *et al.* Facile and Rapid Synthesis of Ultrafine PtPd Bimetallic Nanoparticles and Their High Performance toward Methanol Electrooxidation. *J. Nanomater.* **2014**, e496249 (2014).
109. Jiang, Q. *et al.* Promoting Effect of Ni in PtNi Bimetallic Electrocatalysts for the Methanol Oxidation Reaction in Alkaline Media: Experimental and Density Functional Theory Studies. *J. Phys. Chem. C* **114**, 19714–19722 (2010).
110. Zhou, Y.-Y. *et al.* Self-Decoration of PtNi Alloy Nanoparticles on Multiwalled Carbon Nanotubes for Highly Efficient Methanol Electro-Oxidation. *Nano-Micro Lett.* **8**, 371–380 (2016).
111. Zhang, B. *et al.* Tuning the surface structure of supported PtNi x bimetallic electrocatalysts for the methanol electro-oxidation reaction. *Chem. Commun.* **52**, 3927–3930 (2016).
112. Zhu, C., Guo, S. & Dong, S. Rapid, General Synthesis of PdPt Bimetallic Alloy Nanosponges and Their Enhanced Catalytic Performance for Ethanol/Methanol Electrooxidation in an Alkaline Medium. *Chem. – Eur. J.* **19**, 1104–1111 (2013).
113. Kadirgan, F. *et al.* Carbon supported nano-sized Pt-Pd and Pt-Co electrocatalysts for proton exchange membrane fuel cells. *Int. J. Hydrog. Energy* **34**, 9450–9460 (2009).
114. Kadirgan, F., Beyhan, S. & Atilan, T. Preparation and characterization of nano-sized Pt–Pd/C catalysts and comparison of their electro-activity toward methanol and ethanol oxidation. *Int. J. Hydrog. Energy* **34**, 4312–4320 (2009).
115. Sing, K. S. W. Reporting physisorption data for gas/solid systems with special reference to the determination of surface area and porosity (Recommendations 1984). *Pure Appl. Chem.* **57**, 603–619 (1985).
116. Yin, Z., Zheng, H., Ma, D. & Bao, X. Porous Palladium Nanoflowers that Have Enhanced Methanol Electro-Oxidation Activity. *J. Phys. Chem. C* **113**, 1001–1005 (2009).
117. Dimos, M. M. & Blanchard, G. J. Evaluating the Role of Pt and Pd Catalyst Morphology on Electrocatalytic Methanol and Ethanol Oxidation. *J. Phys. Chem. C* **114**, 6019–6026 (2010).

118. Ghosh, S. *et al.* PEDOT nanostructures synthesized in hexagonal mesophases. *New J. Chem.* **38**, 1106–1115 (2014).
119. Floresyona, D. *et al.* Highly active poly(3-hexylthiophene) nanostructures for photocatalysis under solar light. *Appl. Catal. B Environ.* **209**, 23–32 (2017).
120. Ghosh, S. *et al.* Conducting polymer nanofibers with controlled diameters synthesized in hexagonal mesophases. *New J. Chem.* **39**, 8311–8320 (2015).
121. Surendran, G. *et al.* Highly Swollen Liquid Crystals as New Reactors for the Synthesis of Nanomaterials. *Chem. Mater.* **17**, 1505–1514 (2005).
122. Takamura, T. & Minamiyama, K. Anodic Oxidation of Methanol at Palladium Electrode in Alkaline Solution. *J. Electrochem. Soc.* **112**, 333–335 (1965).
123. Hu, C.-C. & Wen, T.-C. Voltammetric investigation of palladium oxides—I: Their formation/reduction in NaOH. *Electrochimica Acta* **40**, 495–503 (1995).
124. Ghosh, S. *et al.* Conducting polymer-supported palladium nanoplates for applications in direct alcohol oxidation. *Int. J. Hydrog. Energy* **40**, 4951–4959 (2015).
125. Liang, Z. X., Zhao, T. S., Xu, J. B. & Zhu, L. D. Mechanism study of the ethanol oxidation reaction on palladium in alkaline media. *Electrochimica Acta* **54**, 2203–2208 (2009).
126. Anjos, D. M. dos, Hahn, F., Léger, J.-M., Kokoh, K. B. & Tremiliosi-Filho, G. In situ FTIRS studies of the electrocatalytic oxidation of ethanol on Pt alloy electrodes. *J. Solid State Electrochem.* **11**, 1567–1573 (2007).
127. Zhou, Z.-Y., Wang, Q., Lin, J.-L., Tian, N. & Sun, S.-G. In situ FTIR spectroscopic studies of electrooxidation of ethanol on Pd electrode in alkaline media. *Electrochimica Acta* **55**, 7995–7999 (2010).
128. Ma, L., Chu, D. & Chen, R. Comparison of ethanol electro-oxidation on Pt/C and Pd/C catalysts in alkaline media. *Int. J. Hydrog. Energy* **37**, 11185–11194 (2012).
129. An, H. *et al.* Electrocatalytic performance of Pd nanoparticles supported on TiO₂-MWCNTs for methanol, ethanol, and isopropanol in alkaline media. *J. Electroanal. Chem.* **741**, 56–63 (2015).
130. Rand, D. A. J. & Woods, R. The nature of adsorbed oxygen on rhodium, palladium and gold electrodes. *J. Electroanal. Chem. Interfacial Electrochem.* **31**, 29–38 (1971).

131. Grdeń, M., Piaścik, A., Koczorowski, Z. & Czerwiński, A. Hydrogen electrosorption in Pd–Pt alloys. *J. Electroanal. Chem.* **532**, 35–42 (2002).
132. Rolison, D. R. Catalytic Nanoarchitectures--the Importance of Nothing and the Unimportance of Periodicity. *Science* **299**, 1698–1701 (2003).
133. Botz, A. J. R., Nebel, M., Rincón, R. A., Ventosa, E. & Schuhmann, W. Onset potential determination at gas-evolving catalysts by means of constant-distance mode positioning of nanoelectrodes. *Electrochimica Acta* **179**, 38–44 (2015).
134. Zuliani, C., Walsh, D. A., Keyes, T. E. & Forster, R. J. Formation and Growth of Oxide Layers at Platinum and Gold Nano- and Microelectrodes. *Anal. Chem.* **82**, 7135–7140 (2010).
135. Kim, D., Lee, Y. W., Lee, S. B. & Han, S. W. Convex Polyhedral Au@Pd Core–Shell Nanocrystals with High-Index Facets. *Angew. Chem. Int. Ed.* **51**, 159–163 (2012).
136. Zhang, L.-F., Zhong, S.-L. & Xu, A.-W. Highly Branched Concave Au/Pd Bimetallic Nanocrystals with Superior Electrocatalytic Activity and Highly Efficient SERS Enhancement. *Angew. Chem. Int. Ed.* **52**, 645–649 (2013).
137. Song, H. M., Moosa, B. A. & Khashab, N. M. Water-dispersable hybrid Au–Pd nanoparticles as catalysts in ethanol oxidation, aqueous phase Suzuki–Miyaura and Heck reactions. *J. Mater. Chem.* **22**, 15953–15959 (2012).
138. Remita, H., Lampre, I., Mostafavi, M., Balanzat, E. & Bouffard, S. Comparative study of metal clusters induced in aqueous solutions by γ -rays, electron or C₆⁺ ion beam irradiation. *Radiat. Phys. Chem.* **72**, 575–586 (2005).
139. Urchaga, P., Baranton, S., Coutanceau, C. & Jerkiewicz, G. Electro-oxidation of COchem on Pt Nanosurfaces: Solution of the Peak Multiplicity Puzzle. *Langmuir* **28**, 3658–3663 (2012).
140. Urchaga, P., Baranton, S., Coutanceau, C. & Jerkiewicz, G. Evidence of an Eley–Rideal Mechanism in the Stripping of a Saturation Layer of Chemisorbed CO on Platinum Nanoparticles. *Langmuir* **28**, 13094–13104 (2012).
141. Wang, S., Yang, G. & Yang, S. Pt-Frame@Ni quasi Core–Shell Concave Octahedral PtNi₃ Bimetallic Nanocrystals for Electrocatalytic Methanol Oxidation and Hydrogen Evolution. *J. Phys. Chem. C* **119**, 27938–27945 (2015).

142. Ge, Y. *et al.* PtNi/NiO Clusters Coated by Hollow Silica: Novel Design for Highly Efficient Hydrogen Production from Ammonia–Borane. *ACS Appl. Mater. Interfaces* **9**, 3749–3756 (2017).
143. Kamat, P. V. TiO₂ Nanostructures: Recent Physical Chemistry Advances. *J. Phys. Chem. C* **116**, 11849–11851 (2012).
144. Méndez-Medrano, M. G. *et al.* Surface Modification of TiO₂ with Au Nanoclusters for Efficient Water Treatment and Hydrogen Generation under Visible Light. *J. Phys. Chem. C* **120**, 25010–25022 (2016).
145. Bian, Z., Tachikawa, T., Zhang, P., Fujitsuka, M. & Majima, T. Au/TiO₂ Superstructure-Based Plasmonic Photocatalysts Exhibiting Efficient Charge Separation and Unprecedented Activity. *J. Am. Chem. Soc.* **136**, 458–465 (2014).
146. Kowalska, E., Mahaney, O. O. P., Abe, R. & Ohtani, B. Visible-light-induced photocatalysis through surface plasmon excitation of gold on titania surfaces. *Phys. Chem. Chem. Phys.* **12**, 2344–2355 (2010).
147. Kamat, P. V. Manipulation of Charge Transfer Across Semiconductor Interface. A Criterion That Cannot Be Ignored in Photocatalyst Design. *J. Phys. Chem. Lett.* **3**, 663–672 (2012).
148. Luo, Q., Bao, L., Wang, D., Li, X. & An, J. Preparation and Strongly Enhanced Visible Light Photocatalytic Activity of TiO₂ Nanoparticles Modified by Conjugated Derivatives of Polyisoprene. *J. Phys. Chem. C* **116**, 25806–25815 (2012).
149. Linic, S., Christopher, P. & Ingram, D. B. Plasmonic-metal nanostructures for efficient conversion of solar to chemical energy. *Nat. Mater.* **10**, 911–921 (2011).
150. Wang, X. *et al.* A metal-free polymeric photocatalyst for hydrogen production from water under visible light. *Nat. Mater.* **8**, 76–80 (2009).
151. Serpone, N. & Emeline, A. V. Semiconductor Photocatalysis — Past, Present, and Future Outlook. *J. Phys. Chem. Lett.* **3**, 673–677 (2012).
152. Su, C. *et al.* Visible-Light Photocatalysis of Aerobic Oxidation Reactions Using Carbazolic Conjugated Microporous Polymers. *ACS Catal.* **6**, 3594–3599 (2016).
153. Liu, J. *et al.* Metal-free efficient photocatalyst for stable visible water splitting via a two-electron pathway. *Science* **347**, 970–974 (2015).

154. Radiation. Available at: <http://qdl.scs-inc.us/2ndParty/Pages/10522.html>. (Accessed: 3rd June 2017)
155. Polyacetylene, (CH)_x: n-type and p-type doping and compensation. *Appl. Phys. Lett.* **33**, 18–20 (1978).
156. Yuen, J. D. *et al.* Nonlinear transport in semiconducting polymers at high carrier densities. *Nat. Mater.* **8**, 572–575 (2009).
157. Martini, I. B. *et al.* Controlling optical gain in semiconducting polymers with nanoscale chain positioning and alignment. *Nat. Nanotechnol.* **2**, 647–652 (2007).
158. Ma, D., Aguiar, M., Freire, J. A. & Hümmelgen, I. A. Organic Reversible Switching Devices for Memory Applications. *Adv. Mater.* **12**, 1063–1066 (2000).
159. Sirringhaus, H., Tessler, N. & Friend, R. H. Integrated Optoelectronic Devices Based on Conjugated Polymers. *Science* **280**, 1741–1744 (1998).
160. Yin, Z. & Zheng, Q. Controlled Synthesis and Energy Applications of One-Dimensional Conducting Polymer Nanostructures: An Overview. *Adv. Energy Mater.* **2**, 179–218 (2012).
161. Ghosh, S., Maiyalagan, T. & Basu, R. N. Nanostructured conducting polymers for energy applications: towards a sustainable platform. *Nanoscale* **8**, 6921–6947 (2016).
162. Ghosh, S. *et al.* Visible-light active conducting polymer nanostructures with superior photocatalytic activity. *Sci. Rep.* **5**, 18002 (2015).
163. Herrmann, J.-M. Heterogeneous photocatalysis: fundamentals and applications to the removal of various types of aqueous pollutants. *Catal. Today* **53**, 115–129 (1999).
164. Braslavsky, S. E. Glossary of terms used in photochemistry, 3rd edition (IUPAC Recommendations 2006). *Pure Appl. Chem.* **79**, 293–465 (2007).
165. Electronic and Optical Properties of Conjugated Polymers - Oxford Scholarship. (2013). Available at: <http://www.oxfordscholarship.com/view/10.1093/acprof:oso/9780199677467.001.0001/acprof-9780199677467>. (Accessed: 26th April 2017)
166. Epstein, A. J. *et al.* Insulator to metal transition in polyaniline. (1987). Available at: <http://www.physics.ufl.edu/~tanner/PDFS/Epstein87sm-polyaniline2.pdf>. (Accessed: 2nd May 2017)

167. Bolto, B. A., McNeill, R. & Weiss, D. E. Electronic Conduction in Polymers. III. Electronic Properties of Polypyrrole. *Aust. J. Chem.* **16**, 1090–1103 (1963).
168. Shirakawa, H., Louis, E. J., MacDiarmid, A. G., Chiang, C. K. & Heeger, A. J. Synthesis of electrically conducting organic polymers: halogen derivatives of polyacetylene, (CH)_x. *J. Chem. Soc. Chem. Commun.* 578–580 (1977). doi:10.1039/C39770000578
169. Zhang, G., Lan, Z.-A. & Wang, X. Conjugated Polymers: Catalysts for Photocatalytic Hydrogen Evolution. *Angew. Chem. Int. Ed.* **55**, 15712–15727 (2016).
170. Rahman, M. A., Kumar, P., Park, D.-S. & Shim, Y.-B. Electrochemical Sensors Based on Organic Conjugated Polymers. *Sensors* **8**, 118–141 (2008).
171. Electronics of Conjugated Polymers (I): Polyaniline. Available at: <http://connection.ebscohost.com/c/articles/84358543/electronics-conjugated-polymers-i-polyaniline>. (Accessed: 26th April 2017)
172. Atkins, P. & Paula, J. de. *Physical Chemistry*. (W. H. Freeman, 2007).
173. Cheng, Y.-J., Yang, S.-H. & Hsu, C.-S. Synthesis of Conjugated Polymers for Organic Solar Cell Applications. *Chem. Rev.* **109**, 5868–5923 (2009).
174. Shi, Y., Peng, L., Ding, Y., Zhao, Y. & Yu, G. Nanostructured conductive polymers for advanced energy storage. *Chem. Soc. Rev.* **44**, 6684–6696 (2015).
175. Pecher, J. & Mecking, S. Nanoparticles of Conjugated Polymers. *Chem. Rev.* **110**, 6260–6279 (2010).
176. Prieto-Mahaney, O.-O., Murakami, N., Abe, R. & Ohtani, B. Correlation between Photocatalytic Activities and Structural and Physical Properties of Titanium(IV) Oxide Powders. *Chem. Lett.* **38**, 238–239 (2009).
177. Ohtani, B., Mahaney, O. O. P., Amano, F., Murakami, N. & Abe, R. What Are Titania Photocatalysts?—An Exploratory Correlation of Photocatalytic Activity with Structural and Physical Properties. *J. Adv. Oxid. Technol.* **13**, 247–261 (2016).
178. Nanomaterials: A Danger or a Promise? - A Chemical and | Roberta Brayner | Springer. Available at: <http://www.springer.com/us/book/9781447142126>. (Accessed: 18th April 2017)
179. Günes, S., Neugebauer, H. & Sariciftci, N. S. Conjugated Polymer-Based Organic Solar Cells. *Chem. Rev.* **107**, 1324–1338 (2007).

180. Wang, D. *et al.* Characterization and photocatalytic activity of poly(3-hexylthiophene)-modified TiO₂ for degradation of methyl orange under visible light. *J. Hazard. Mater.* **169**, 546–550 (2009).
181. Zheng, T., Xu, J., Zhang, Z. & Zeng, H. P3HT/Bi₂MoO₆ heterojunction with enhanced photocatalytic activity. *Mater. Lett.* **164**, 640–643 (2016).
182. Qiao, X., Wang, X. & Mo, Z. The effects of different alkyl substitution on the structures and properties of poly(3-alkylthiophenes). *Synth. Met.* **118**, 89–95 (2001).
183. Serpone, N. *et al.* Standardization protocol of process efficiencies and activation parameters in heterogeneous photocatalysis: relative photonic efficiencies ζ_r . *J. Photochem. Photobiol. Chem.* **94**, 191–203 (1996).
184. Brown, P. J. *et al.* Effect of interchain interactions on the absorption and emission of poly(3-hexylthiophene). *Phys. Rev. B* **67**, 064203 (2003).
185. Cook, S., Furube, A. & Katoh, R. Analysis of the excited states of regioregular polythiophene P3HT. *Energy Environ. Sci.* **1**, 294–299 (2008).
186. Piris, J. *et al.* Photogeneration and Ultrafast Dynamics of Excitons and Charges in P3HT/PCBM Blends. *J. Phys. Chem. C* **113**, 14500–14506 (2009).
187. Trotzky, S., Hoyer, T., Tuszynski, W., Lienau, C. & Parisi, J. Femtosecond up-conversion technique for probing the charge transfer in a P3HT : PCBM blend via photoluminescence quenching. *J. Phys. Appl. Phys.* **42**, 055105 (2009).
188. Cruz, R. A., Catunda, T., Facchinatto, W. M., Balogh, D. T. & Faria, R. M. Absolute photoluminescence quantum efficiency of P3HT/CHCl₃ solution by Thermal Lens Spectrometry. *Synth. Met.* **163**, 38–41 (2013).
189. Ghosh, S. *et al.* Conducting polymer-supported palladium nanoplates for applications in direct alcohol oxidation. *Int. J. Hydrog. Energy* **40**, 4951–4959 (2015).
190. Antolini, E. Composite materials: An emerging class of fuel cell catalyst supports. *Appl. Catal. B Environ.* **100**, 413–426 (2010).
191. A polymer–metal–polymer–metal heterostructure for enhanced photocatalytic hydrogen production - *Journal of Materials Chemistry A* (RSC Publishing) DOI:10.1039/C4TA04636F. Available at: <http://pubs.rsc.org/-/content/articlehtml/2015/ta/c4ta04636f>. (Accessed: 13th July 2017)

192. Polymer-supported CuPd nanoalloy as a synergistic catalyst for electrocatalytic reduction of carbon dioxide to methane. Available at: <http://www.pnas.org/content/112/52/15809.full>. (Accessed: 13th July 2017)
193. Jana, B., Bhattacharyya, S. & Patra, A. Conjugated polymer P3HT–Au hybrid nanostructures for enhancing photocatalytic activity. *Phys. Chem. Chem. Phys.* **17**, 15392–15399 (2015).
194. Cui, Z. *et al.* Radiation-induced reduction–polymerization route for the synthesis of PEDOT conducting polymers. *Radiat. Phys. Chem.* **119**, 157–166 (2016).

Titre : Synthèse des nanostructures métalliques et de polymères conjugués dans des mésophases hexagonales pour des applications en piles à combustible et en photocatalyse

Mots clés : Mésophases hexagonales, nanostructures métalliques poreuses, nanostructures de polymères conjugués, électrocatalyse, photocatalyse, radiolyse, piles à combustible, oxydation de l'éthanol, dépollution de l'eau.

Résumé : Les mésophases hexagonales sont des systèmes quaternaires formés de tensioactifs et co-tensioactifs, eau salée et huile. Ces mésophases sont utilisées comme moules « mous » pour la synthèse de différents nanomatériaux tels que des nanostructures métalliques poreuses, des nanostructures de polymères conjugués et des nanocomposites métalliques-polymères. Contrairement aux matrices (ou moules) durs, qui nécessitent des réactifs chimiques corrosifs pour extraire les nanomatériaux synthétisés *in situ*, le processus d'extraction des nanomatériaux synthétisés dans les mésophases hexagonales est simple : les nanomatériaux peuvent être extraits simplement par lavage avec de l'éthanol ou du 2-propanol. Un autre intérêt à utiliser ces mésophases comme matrice de synthèse est qu'elles peuvent être gonflées en contrôlant le rapport huile / eau.

Cette thèse est divisée en trois parties: 1) La synthèse de nanostructures métalliques poreuses dans la phase aqueuse des mésophases hexagonales et leur application dans les piles à combustible (oxydation de l'éthanol), 2) La synthèse de nanostructures de polymères conjugués dans la phase huile des mésophases hexagonales pour des applications en photocatalyse et en particulier pour la dégradation de polluants, 3) La synthèse combinée dans les phases huile et eau des mésophases hexagonales de nanocomposites métal-polymère.

Plusieurs nanostructures métalliques telles que des nanoballes PdPt de porosité et composition contrôlées, des nanostructures poreuses cœur-coquille AuPd et AuPt, bimétalliques PtNi et trimétalliques AuPdPt ont été synthétisées par radiolyse dans la phase aqueuse des mésophases hexagonales. Les nanoballes PdPt de porosité -

et composition contrôlées ont été utilisées comme électro-catalyseurs pour l'oxydation de l'éthanol. L'effet de la taille des pores sur la surface électro-active des nanostructures métalliques et leur activité électrocatalytique pour l'oxydation de l'éthanol a été étudié. Les nanostructures poreuses cœur-coquille bimétalliques AuPd et AuPt, et trimétalliques AuPdPt ont été utilisées pour l'oxydation de l'éthanol et du glucose. Les nanoballes poreuses PtNi ont été utilisées pour l'évolution de H₂ et la réaction de réduction de l'oxygène.

Des nanostructures de polymères conjugués (poly(3-hexylthiophène), P3HT) ont été synthétisées dans la phase huile des mésophases hexagonales. Ces nanostructures de polymères ont une activité photocatalytique élevée sous UV et lumière visible. Le phénol et la rhodamine B ont été utilisés comme polluants modèles. Ces photocatalyseurs sont très stables même après plusieurs cycles photocatalytiques. L'ajout de molécules capteurs et l'étude du mécanisme montrent que les radicaux O₂⁻ sont les principaux radicaux responsables de la dégradation du phénol. De manière très intéressante, l'activité photocatalytique de ces nanostructures de P3HT est fortement augmentée lorsqu'elles sont supportées sur une surface solide. Ce résultat ouvre de nouvelles perspectives pour des applications dans des réacteurs photocatalytiques et des surfaces autonettoyantes.

Des résultats préliminaires sur la synthèse des nanocomposites Pt-PDPB (polydiphenylbutadiyne) sont également présentés dans cette thèse.



Title : Synthesis of metal and conjugated polymer nanostructures in hexagonal mesophases for application in fuel cells and photocatalysis

Keywords : hexagonal mesophases, porous metal nanostructures, conjugated polymer nanostructures, electrocatalysis, photocatalysis, radiolysis, fuel cells, ethanol oxidation, water depollution.

Abstract : Soft hexagonal mesophases, which consist of quaternary systems (surfactants, brine, oil, and co-surfactant) are used as templates for the synthesis of different nanomaterials such as metal nanostructures, conjugated polymer nanostructures, and metal-polymer nanocomposites. Unlike hard templates, which need a harsh chemical reagents to extract nanomaterials after the synthesis, in soft template hexagonal mesophases, the extraction process of nanomaterials is simple, only by washing with ethanol or 2-propanol. Another interesting property of this class of template lies on its ability to be swollen by controlling the ratio of oil to water.

This thesis is divided into three parts: 1) Radiolytic synthesis of metal nanostructures in the aqueous phase of hexagonal mesophases and their application in fuel cells (ethanol oxidation), 2) Synthesis of conjugated polymer nanostructures in the oil phase of hexagonal mesophases for photocatalytic degradation of pollutants, 3) Combined synthesis in the oil and water phases of hexagonal mesophases of metal-polymer nanocomposites.

Several metal nanostructures such as PdPt nanoballs with controlled composition and porosity, AuPd and AuPt core shell, bimetallic PtNi and trimetallic AuPdPt porous nanoballs were synthesized by radiolysis in the aqueous phase of hexagonal mesophases.

PdPt nanoballs with controlled porosity and composition were used as electrocatalysts for ethanol oxidation. The effect of the pore size on their electro active surface and their electrocatalytic activity towards ethanol oxidation were studied. AuPd and AuPt core-shell, and trimetallic AuPdPt porous nanoballs were used for ethanol and glucose oxidation. PtNi porous nanoballs were used for H₂ evolution and oxygen reduction reaction.

Conjugated polymer nanostructures namely P3HT (poly(3-hexylthiophene)) were synthesized in the oil phase of hexagonal mesophases. These polymer nanostructures are highly active for photocatalysis under UV and visible light. Phenol and rhodamine B were used as model pollutants. These photocatalysts are very stable even after repeated cycling. Addition of scavengers and mechanistic studies show that O₂⁻ is the main radical responsible for degradation of phenol. Most interestingly, the photocatalytic activity of these P3HT nanostructures is highly enhanced when they are supported on a solid surface opening new perspectives in photocatalytic reactors and self-cleaning surfaces.

Preliminary results on the synthesis of Pt-PDPB (polydiphenylbutadiyne) nanocomposites are also presented in this thesis.